LUNDS UNIVERSITET

# Spatio-temporal characterization of intense ultrashort laser pulses

Master Thesis

by Mekan Merdanov

Supervisor: Cord Arnold

Co-supervisor: Per Eng-Johnsson

Examiner: Jörgen Larsson

LRAP: 599






18th July 2024

# Abstract

When ultrashort pulses pass through common optical elements such as gratings and thick lenses, they can pick up spatio-temporal couplings (STCs) - nonseparable chromatic aberrations. The main cause of this phenomenon is the inherent feature of ultrashort pulses—their broadband spectrum. STCs increase pulse duration and reduce the intensity at the focus, which will be detrimental for many applications, for example, in high-harmonic generation (HHG). This project identifies and visualizes the STCs of ultrashort laser pulses used for HHG and laser-driven acceleration by removing aberrations shared by all wavelengths. Spatially resolved Fourier Transform spectrometry is the main method for our STC characterization. Improvement of the existing data analysis code, including the shared aberration removal and comprehensive STC analysis documentation are included in this work.

# Popular science summary

Lasers have unique properties that distinguish them from ordinary sunlight or light from our homes' lamps. That property is known as spatial and temporal coherence. Thanks to those properties, pulses with very short duration, i.e., in the femtosecond range, can be generated. A femtosecond is the millions of billions of a second. But why do we need such a short pulse? There are two answers: first, using the short pulse, we can take a "movie" of fast events, and second, achieving high intensity is feasible with short pulses. By saying "fast event," we mean ultrafast events like electron motion around nuclei in the atom and chemical reactions that unfold on the femtosecond (fs) time scale.

Relatively recently, the process called high-order harmonic generation allowed to achieve pulses on the attosecond time scale. It is an extremely short duration (1 as=1 $\cdot 10^{-18}$ s). Accessing such an ultrashort duration provides us with advanced insights into the dynamics of electrons in atoms, molecules, and solids. This knowledge can be applied to achieve real-time control of electron motion in matter, with practical applications such as the transition from THz-to-PHz electronics, probing the molecular composition of biological systems for health monitoring, and disease detection. Reaching high intensity with ultrashort pulses has important applications in particle acceleration. Since at such high intensity, particles can accelerate close to the speed of light in less than a meter. This allows us to drastically reduce the size of conventional particle accelerators. High-speed protons can kill cancer cells, which has an important application in medicine.

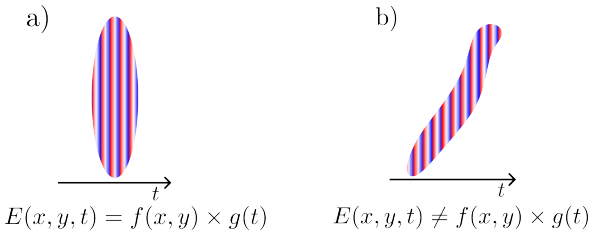


**Figure 1:** Illutration of a) clean pulse (no STC) b) distorted pulse (with STC). Image adapted from [1].

When generating and manipulating ultrashort pulses, their field can be distorted by common optical elements, like lenses, gratings, etc. These distortions are usually called spatio-temporal couplings (STC). To put it in the simplest terms, STC means that the pulse properties cannot be written separately as a space and a temporal component. These distortions can be beneficial or harmful to the system. In both cases, it becomes important to characterize them. During this project, STC characterization is done for the two laser systems used for high-order harmonic generation (AttoLab) and particle acceleration (Multi-pass cell MPC system at DESY). In the AttoLab, significant STCs are observed. STCs are also present in the source of the MPC system but these do not transfer to the compressed output pulses.

# Acknowledgements

I would like to express my sincere gratitude to my supervisor, Cord. Without his guidance, I would not have been able to complete this project. As a local director of the LASCALA master program and teacher, he has been a source of guidance and inspiration to me. His comments on my written thesis were great inspirations to make this thesis more comprehensive to the reader. Special thanks to Ann-Kathrin for mentoring me during this project. Her positivity and willingness to help at any time made this work much valuable and fun. Thanks also to my co-supervisor, Per Eng-Johnsson, for his interesting discussions in the group meetings.

I am equally grateful to Chen for his assistance when I encountered difficulties with the MATLAB code. His willingness to devote time, even late in the lab, to help me with this project has been invaluable. His expertise in optics has enlightened me on various aspects of aberrations and spatiotemporal couplings. I also want to thank Anne-Lise and Saga for their support and time during the DESY experimental campaign.

Thanks to Elisa and Venus for their very clear explanations, guidance in the lab, and career advice for a PhD. Also, thanks to all the Atomic Physics division staff members for their friendliness and warm welcome.

I want to say thanks to the European Union, which supported me financially with a generous scholarship during my LASCALA master's program.

Lastly, I want to thank my family for their constant support and my LASCALA friends Emmanuel, Camila, and Javier for sharing time with me on this incredible journey.

# Notations

## Abbreviations

STC -Spatio-temporal coupling
PFT - Pulse front tilt
PFC - Pulse front curvature
CPA - Chirped Pulse Amplification
OPCPA - Optical Parametric Chirped Pulse Amplification
AD - Angular dispersion
GD - Group delay
GDD - Group delay dispersion
NF - Near-field
FF- Far-field
CC - Chromatic curvature
CCD - Charge-coupled device MPC - Multi-pass cell compression
FT - Fourier Transform
d-scan - dispersive scan
FROG - Frequency-resolved optical gating
FTS - Fourier Transform Spectroscopy
FFT - Fast Fourier Transform
MMT - Mode matching telescope
TEL - Telescope
CMP - Compressor
STARFISH-spatio-temporal amplitude-and-phase reconstruction by Fourier-transform of interference spectra of high-complex-beams
SPIDER - spectral phase interferometry for direct electric-field reconstruction
SPM - Self phase modulation
TERMITES - Total E-field reconstruction using a Michelson interferometer temporal scan

# Contents

# 1 Introduction

The invention of the laser has profoundly impacted the field of science and technology. Lasers' unique characteristics, such as temporal coherency, enable the generation of ultrashort pulses. Spatial coherency allows the laser to be focused on a precise spot. These features have various practical applications, including imaging ultrafast processes, laser cutting, and lithography.

The generation of ultrashort pulses is crucial for high optical power delivery and imaging of ultrafast processes. Continuous progress has been made in reducing the pulse durations from nanosecond and picosecond to extremely short femto- and attosecond (as) pulses. We can achieve high peak power by concentrating the modest energy in a very short duration. The first lasers, built between 1960 and 1970, generated peak power from megawatts (MW) to gigawatts (GW). However, in the subsequent decade, laser peak power remained unchanged due to the damage to the amplifier material at high power. The advance of the chirped-pulse amplification technology (CPA) [2] allowed it to reach terawatt (TW) and then petawatt (PW) peak power levels. The discovery of high-harmonic generation (HHG) in gases when exposed to the highly intense laser field led to the generation of extremely ultrashort attosecond pulses. To put this into perspective, consider how many times one second is smaller than the age of the universe, one attosecond is equivalently smaller than one second [3]. Ultrashort pulses are used to image the ultrafast biological, chemical, and physical processes. Moreover, the intense ultrashort pulses are used for electron wake-field acceleration and laser fusion.

With the advancement of the generation of ultrashort pulses, their characterization became important. How do we know our ultrashort pulse is short? What are its spatial characteristics? Currently, commercially available photodetectors can accurately measure the duration of nanosecond pulses. However, if we want to measure pico- and femtosecond pulse duration, we need a shorter event to make the measurement. Since no such event was available, researchers found a clever solution: the shortest event available was the event itself. As a result, the autocorrelation method was developed [4]. The other popular methods include frequency-resolved optical gating (FROG) [5], spectral phase interferometry for direct electric-field reconstruction (SPIDER) [6], and dispersion scan (d-scan) [7].

The above-mentioned methods assume that the temporal (or spectral) field has the same properties at all points in the beam and can give correct characterization, if the field is spatially homogenous. However, in generating and manipulating ultrashort pulses, the beam is exposed to spatio-temporal distortions commonly known as spatio-temporal couplings (STC). Examples of STCs are group delay variations across the beam, i.e., the spatially varying time of arrival in the transverse direction. More generally, spatio-temporal coupling corresponds to the case when spectral/temporal properties of a broadband field are not spatially homogenous. This results in a pulse duration increase and intensity reduction at the focus. STC can be detri-

mental or beneficial depending on the application. In both cases, it is important to give them characterization. Because of that, many STC characterization techniques were developed. Spatially-encoded arrangement SPIDER (SEA-SPIDER) [8] and spatio-temporal amplitude-and-phase reconstruction by Fourier-transform of interference spectra of high-complex-beams (STARFISH) [9], are few examples of them. The main focus of this thesis is STC characterization of ultrashort pulses using spatially resolved Fourier Transform Spectrometry (FTS) technique [7]. In this technique, the unknown pulse is separated into two. One is used to make a homogenous beam, which is brought to interfere with the other one on the camera chip. By changing the delay between the reference and the unknown beam, we obtain a spectrogram for each pixel of the camera. Assuming the reference beam is known, we can subtract the unknown phase for each pixel, i.e., spatially resolve it. Thus, in the end, the 3 dimensional (two space and one time/frequency) data of the unknown complex field are obtained. From that data, one can inspect the pulse's STCs.

## 1.1 Objective

This project concerns the STC characterization of intense ultrashort laser pulses located at the Lund High-Power Laser Facility and the German Electron Synchrotron (DESY). To achieve this, the spatially resolved Fourier Transform Spectroscopy technique [10] is used. The Titanium-doped Sapphire (Ti: Sapphire) CPA laser based in Lund has a central wavelength of around 800 nm, pulse duration of around 20 fs, and repetition rate of 3 kHz. The laser comprises a grating compressor to achieve the final pulse duration after the amplification. Like any dispersive element, it is a potential source for STCs. The STC measurements were performed to determine the existence of any STC in the output of the Ti: Sapphire laser. Similar STC measurements were performed for each stage of the Multi-pass-cell compressed (MPC) setup at DESY. MPCs are a new technique [11] which allows temporal compression of the pulses from picosecond down to femtosecond duration. The goal is to determine whether STCs exist in this setup, which hasn't been done before.

The obtained data involves cumbersome manipulations of 3D matrices representing ultrashort laser pulses in space and time/frequency, which will be discussed in great detail in section 3.2. The common aberration shared by all wavelength components must be removed to see the true STC. This feature was added to the existing MATLAB code, which has been optimized and well-documented.

## 1.2 Motivation

Like any electromagnetic wave, light pulses can be described in the form of an electric field. Usually, the spatial and the temporal/spectral parts are assumed to be independent of each other, i.e., the field can be written as the product of the spatial and temporal/spectral profiles. Although this assumption is valid in many cases, it is often wrong in the case of ultrashort pulses. The impossibility of separating the

spatial from the temporal behavior of ultrashort pulses is due to their broad spectral bandwidth. This mutual dependence of spatial and temporal coordinates is called spatio-temporal couplings (STC). Common sources of STCs are prisms, gratings, singlet lenses, nonlinear optical interactions, and even simple apertures, which nicely illustrate the wavelength dependence of diffraction. Prisms and gratings introduce STCs, like angular chirp, pulse-front tilt, and spatial chirp, which will be discussed in section 2.4. Singlet lenses introduce pulse front curvature as a result of their chromaticity [12]. Depending on their applications, STCs can be detrimental or beneficial for ultrafast optical systems. A chirped pulse amplification system and 4-F pulse shapers are built to introduce and subsequently compensate for any STCs. STCs increase the pulse duration and decrease the intensity of the focus. On the other hand, STCs are beneficial for controlling the beam properties and, thus, light-matter interaction processes. For example, one can optimize the non-linear sum or frequency difference generation, broadband THz generation with controlled STC [13] and generate isolated attosecond pulses by using the attosecond lighthouse effect [14].

## 1.3 Thesis outline

Chapter 2 provides the necessary theoretical information for this project. It involves the time-frequency description of ultrashort pulses (section 2.1.1), basic principles of Fourier Optics, pulse compression techniques, and a description of the common types of aberrations. Since the main focus of this project is about STCs, I included a detailed description of STCs with simulations in section 2.4. Then, chapter 3 gives a detailed description of the method and steps of data processing in the example of the data obtained from the Ti: Sapphire CPA laser. The last chapter 5 gives the conclusion of the results and a future outlook of possible improvements of the STC setup.

# 2 Theory

This chapter provides essential theoretical background for this work. Most of the theoretical part is influenced by literature [15], [16]. Since the main focus of this project is the characterization of ultrashort pulses, the first big section 2.1 is dedicated to ultrafast optics and is divided into several subsections. It starts with a time and frequency description of ultrashort pulses (subsection 2.1.1), followed by the propagation of ultrashort pulses in the media (subsection 2.1.2) and ends with basic principles of pulse compression (subsection 2.1.3).

Since the data analysis part of this project involves focusing, spatial filtering, and shared aberration removal of the ultrashort pulse, it is relevant to briefly introduce Fourier Optics and Aberration theory in section 2.2. This section briefly starts with the principles of Fourier Optics in subsection 2.2.1. The following subsection gives comprehensive information about common types of aberration (subsection 2.2.2) and descriptions of the aberrated wavefront (subsection 2.2.3).

The following section 2.3 gives a short introduction to the amplification of ultrashort pulses.

This chapter concludes with section 2.4 about the detailed theory of Spatio-Temporal Couplings (STCs) - the main focus of this project.

## 2.1 Ultrafast Optics

### 2.1.1 Time and frequency description of ultrashort pulses

Using the fundamental laws of Maxwell's electromagnetic theory, we can derive the wave equation:

$$\nabla^2 u - \frac{1}{c^2}\frac{\partial^2 u}{\partial t^2} = 0 \tag{2.1}$$

Where $c = c_0/n$ - speed of the optical wave in the material. $\nabla^2 = \partial^2/\partial^2 x^2 + \partial^2/\partial y^2 + \partial^2/\partial z^2$ - Laplacian operator in cartesian coordinates.

We can describe the monochromatic wave at position $\mathbf{r} = (x, y, z)$ at given time $t$ using the *wavefunction*: $u(\mathbf{r}, t) = a(\mathbf{r}) \cos[2\pi\nu t + \phi(\mathbf{r})]$. But for mathematical manipulations, using the complex amplitude $U(\mathbf{r}, t)$ is convenient. Its real part gives us wavefunction $\mathrm{Re}\{U(\mathbf{r}, t)\}$:

$$U(\mathbf{r}, t) = U(\mathbf{r}) \exp(j2\pi\nu t) \tag{2.2}$$

where $U(\mathbf{r}) = a(\mathbf{r}) \exp[j\phi(\mathbf{r})]$- is called *complex amplitude* of the wave.

For considering optical pulse in the time domain, we can omit the spatial part and only focus on the temporal part of the complex amplitude equation 2.2. Then for an optical pulse with central frequency $\nu_0$ we can write $U(t) = A(t) \exp j2\pi\nu_0 t$, where $A(t) = |A(t)| \exp[j\phi(t)]$ - *complex envelope* with amplitude $|A(t)|$ and phase $\phi(t)$. Intensity in the time domain is $I(t) = |A(t)|^2$. Using the equation for the complex envelope, we can write:

$$U(t) = |A(t)| \exp(j[\omega_0 t + \phi(t)]) \tag{2.3}$$

Where $\omega_0 = 2\pi\nu_0$ - is the central angular frequency of the optical pulse. To characterize the optical pulse in the spectral domain, we need to take the Fourier transform of the equation 2.3. This will give us a function centered around the angular frequency $\omega_0$:

$$U(\omega) = |U(\omega)| \exp[j\psi(\omega)] \tag{2.4}$$

where $|U(\omega)| = \sqrt{S(\omega)}$- is the spectral amplitude, $S(\omega)$ - spectral intensity, $\psi(\omega)$- spectral phase.

Taking the derivative from the phase of equation 2.3, we can find the instantaneous angular frequency given by:

$$\omega_{ins} = \omega_0 + \frac{d\phi}{dt} \tag{2.5}$$

Let's analyze the time evolution of the phase $\phi(t)$ of the complex envelope (eq. 2.3). For that, we will Taylor expand this phase around the pulse center (in our case $t_0 = 0$):

$$\phi(t) = \phi_0 + \left.\frac{\partial\phi(t)}{\partial t}\right|_{t_0} t + \frac{1}{2}\left.\frac{\partial^2\phi(t)}{\partial t^2}\right|_{t_0} t^2 + ... \tag{2.6}$$

Here, the first term in this equation, $\phi_0$, is called the carrier-envelope offset phase (CEP), which describes the difference between the optical phase of the carrier wave and the envelope position (see fig. 2.1). The second term makes a shift in the frequency domain, as one can observe from equation 2.5. The third term corresponds to chirp: if $\phi'' = \partial^2\phi/\partial t^2 > 0$ pulse is **up-chirped**, if $\phi'' < 0$ pulse is **down-chirped**. In the former case, the instantaneous frequency will linearly increase; in the latter case, the instantaneous frequency will linearly decrease. The higher terms in eq. 2.6 results in nonlinear changes of instantaneous frequency.

Similarly, we can expand the spectral phase into the Taylor series around the central frequency $\omega_0$:

$$\psi(\omega) = \psi_0 + \left.\frac{\partial\psi(\omega)}{\partial\omega}\right|_{\omega_0} (\omega - \omega_0) + \frac{1}{2}\left.\frac{\partial^2\psi}{\partial\omega^2}\right|_{\omega_0} (\omega - \omega_0)^2 + \frac{1}{6}\left.\frac{\partial^3\psi}{\partial\omega^3}\right|_{\omega_0} (\omega - \omega_0)^3 + ... \tag{2.7}$$

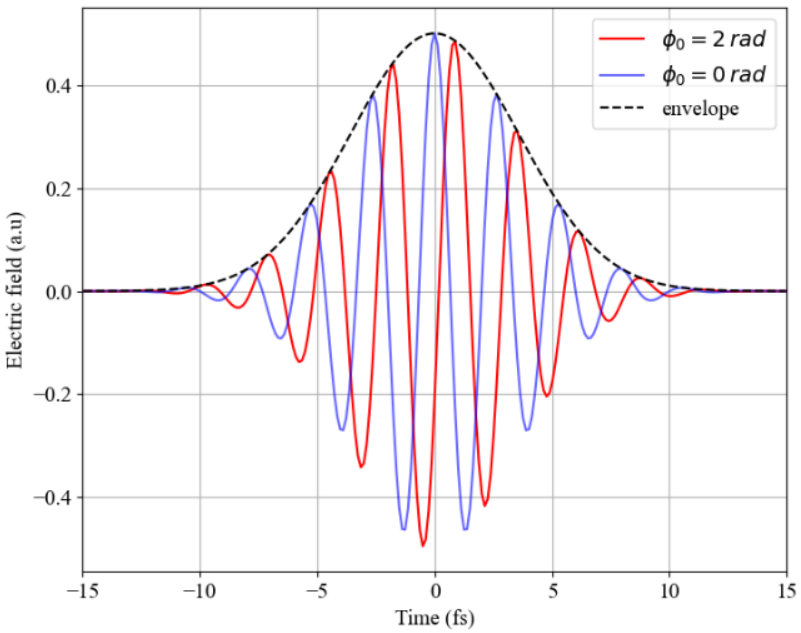


**Figure 2.1:** Effect of CEP (carrier-envelope offset) phase $\phi_0$ to ultrashort pulse

Here, the first term $\psi_0$ corresponds to the CEP in the spectral domain, and it is the same as $\phi_0$ due to the linearity of the Fourier transform. The second term corresponds to a shift in the time domain and is defined as *Group Delay* GD $= \partial\psi(\omega)/\partial\omega$ of the pulse. The third term corresponds to chirp. Since it involves the second order frequency derivative of phase or first order derivative of GD, thus, it is defined as the *Group Delay Dispersion* GDD$= \partial(\text{GD})/\partial\omega = \partial^2\psi(\omega)/\partial\omega^2$.

Figure 2.2 shows the pulses with Gaussian shape and at different phase values in both temporal and spectral domains.

The pulse duration of the Gaussian pulse $\Delta\tau$ is taken as the full-width half maximum (FWHM) of its intensity $I(t)$. Similarly, we define the pulse's spectral width $\Delta\nu$ as FWHM of spectral intensity $S(\omega)$. The relation between these two variables is:

$$\Delta\tau\Delta\nu \geq 0.44 \tag{2.8}$$

We can deduce from this equation that the broader the pulse spectrum, the shorter the pulse potentially becomes. For the $\Delta\tau\Delta\nu = 0.44$ case, we call it the pulse is Fourier limited pulse.

### 2.1.2 Pulse propagation

#### Group vs. Phase velocity

The most commonly known effect when light propagates through material is dispersion. It is caused by the fact that different frequency components of the pulse propagate at different velocities. Because we know that the velocity of light in the material is

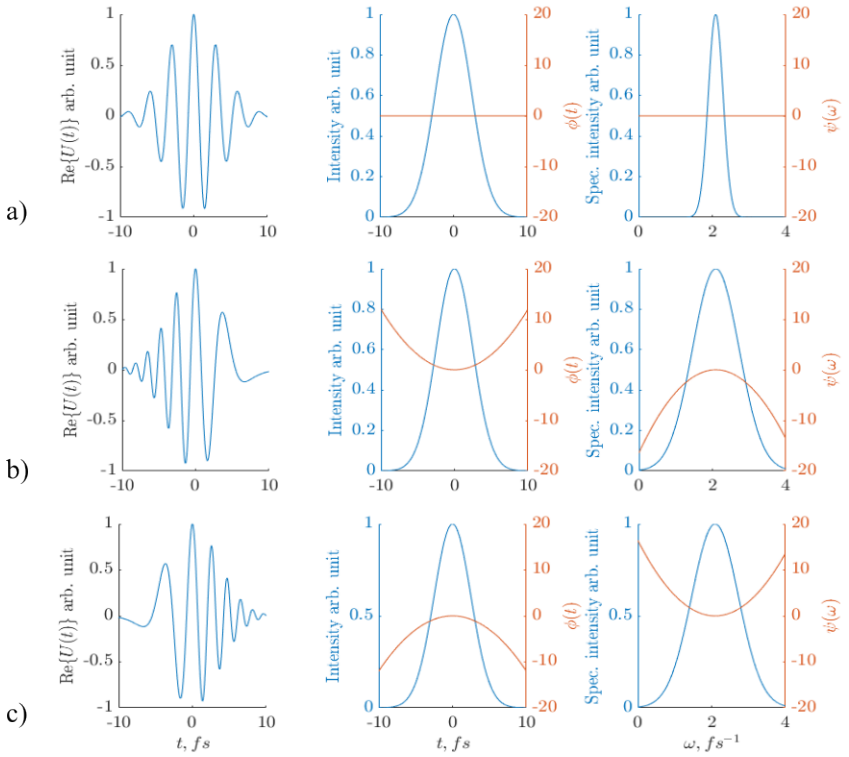


**Figure 2.2:** Temproal and spectral profiles of the Gaussian pulse with pulse duration $5\,fs$ central angular frequency $\omega_0 = 2.093\,fs^{-1}$. a) Tranfrom limited pulse, b) Down-chirped pulse with chirp parameter $\phi'' = -3$, c) Up-chirped pulse with $\phi'' = 3$

defined by $c_n = c/n(\lambda)$, where $c$ - speed of light in the vacuum, $n(\lambda)$ - refractive index of material that depends on the wavelength and can be described with good accuracy by the Sellmeier's equation:

$$n^2(\lambda) = 1 + \sum_k \frac{B_k \lambda^2}{\lambda^2 - C_k} \tag{2.9}$$

where, $B_k, C_k$ - are experimentally determined constants of material, $\lambda$-wavelength of the light in the vacuum. The shorter the pulse, the broader its spectrum and the stronger the effects of dispersion on the pulse. When considering ultrashort pulse propagation, separating the two concepts, group velocity and phase velocity, is useful. The phase velocity of ultrashort pulse with central frequency $\omega_0$ is defined as [16]: $v_p \equiv c_n = \frac{\omega}{k_n}\Big|_{\omega_0}$ while the group velocity of the same ultrashort pulse is defined as $v_g \equiv \frac{d\omega}{dk_n}\Big|_{\omega_0}$, where $k_n = kn(\omega)$-wavenumber of the pulse in the material, $k = 2\pi/\omega$-the wavenumber in the vacuum. Phase velocity corresponds to the velocity of the carrier wave, and group velocity corresponds to the propagation speed of the envelope of the pulse (see figure 2.3).

By inserting the value of the $k_n$ into the group velocity equation, we can find:

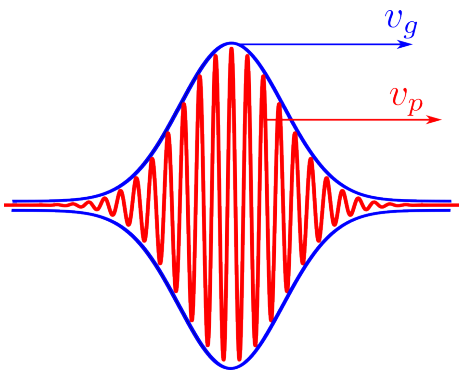


**Figure 2.3:** Illustration of group and phase velocity. Phase front propagates with phase velocity and peak of the envelope propagates with group velocity

$$\frac{1}{v_g} = \frac{dk_n(\omega)}{d\omega} = \frac{d}{d\omega}\left[\frac{n(\omega)\omega}{c}\right] = \frac{n(\omega)}{d\omega}\frac{\omega}{c} + \frac{n}{c} \tag{2.10}$$

And using the relation:

$$\nu = \frac{c}{\lambda} => \frac{d\nu}{d\lambda} = -\frac{c}{\lambda^2} = -\frac{\nu}{\lambda} => \frac{d\nu}{\nu} = -\frac{-d\lambda}{\lambda} \tag{2.11}$$

since $\omega = 2\pi\nu$, we can find that $\frac{d\omega}{\omega} = -\frac{d\lambda}{\lambda}$. And hence

$$\frac{dn(\omega)}{d\omega}\omega = -\frac{dn(\lambda)}{d\lambda}\lambda \tag{2.12}$$

Putting this equation into equation 2.10, we can find the equation for the group velocity:

$$v_g = \frac{c}{n - \frac{dn}{d\lambda}\lambda} = \frac{c}{n_g} \tag{2.13}$$

where $n_g = n - (dn/d\lambda)\lambda$ - is defined as the *group index*.

Consider the transform-limited pulse with duration $\tau_0$ linearly propagates through the material with positive dispersion. This medium will create the phase shift $\phi = k_n L = kn(\omega)L$ and the pulse will have duration given by:

$$\tau(L) = \tau_0\sqrt{1 + \left(\frac{4\ln 2\frac{d^2\phi}{d\omega^2}}{\tau_0^2}\right)^2} \tag{2.14}$$

Where $d^2\phi/d\omega^2 = GDD$-group delay dispersion introduced by the medium. This equation shows that the pulse duration is increased and positively chirped after passing the medium. In other words, longer wavelength spectral components go faster than shorter wavelengths, $\lambda_1 > \lambda_2 => v_g(\lambda_1) > v_g(\lambda_2)$ or "red goes faster than blue." This

is true for the case of normal dispersion, i.e., in the wavelength from the ultraviolet (UV) to the near-infrared range of the spectrum (NIR). However, dispersion will be anomalous for the longer wavelength, and the effect will be reversed. Notably, the pulse spectrum does not change during propagation.

### 2.1.3 Pulse compression

We saw that when the pulse propagates through a material with positive dispersion, it obtains positive $GDD$, and its duration increases. To compensate for positive $GDD$ and compress the pulse duration, we need to use another optical system that can introduce negative dispersion. The most practical way is to use a system containing angular dispersion elements such as prisms, gratings, or Bragg mirrors.

The wavelength dependence of the refractive index in Snell's law results in different wavelength components being refracted at different angles and traveling on different geometrical paths. It has been shown that regardless of the sign of the material dispersion (positive or negative), the angular dispersion (AD) introduces negative $GDD$ [17].

For compressing the pulse with a prism, only using a single prism is not enough. We need to use a prism pair (fig. 2.4 a.). The first prism will introduce angular dispersion, i.e., short wavelengths ("blue part") will be refracted more strongly than longer ones ("red part"), and the different colors will propagate in different directions. The second prism will collimate the angular dispersion, but the colors are spatially separated from each other. This can be compensated by reversing the beam propagation using mirrors or using another couple of prisms (fig. 2.4 b.). In the end, we can obtain the pulse with negative $GDD$, i.e., "blue goes faster than red" in the space between the prisms.

The same reasoning applies to grating compressors (fig. 2.4 c.). In the grating compressor configuration, the longer wavelength part of the pulse travels a longer distance than the shorter wavelength part. As a result, it introduces the negative $GDD$. Moreover, we can control the amount of $GDD$ by changing the distance $L_g$ between two parallel gratings. This $GDD$ can be found using the following equation [16]:

$$\frac{d^2\phi}{d\omega^2} = -\frac{\lambda_0^3 L_g}{\pi c_0^2 \Lambda^2}\left[1 - \left(\frac{\lambda_0}{\Lambda} - \sin\theta_i\right)^2\right]^{-3/2} \tag{2.15}$$

where $\lambda_0$ - central wavelength of the pulse, $\theta_i$- incident angle of the pulse to a grating compressor, $\Lambda$-grating period.

Another pulse compression option is Bragg-Grating mirrors or Bragg-Grating chirp mirrors, which have revolutionized ultrashort pulse generation. These mirrors are designed to gradually increase the Bragg wavelength from the surface to the substrate. This allows shorter wavelength parts to be reflected closer to the surface while the longer parts can penetrate deeper, resulting in negative $GDD$ of the output pulse ("blue goes faster than red").

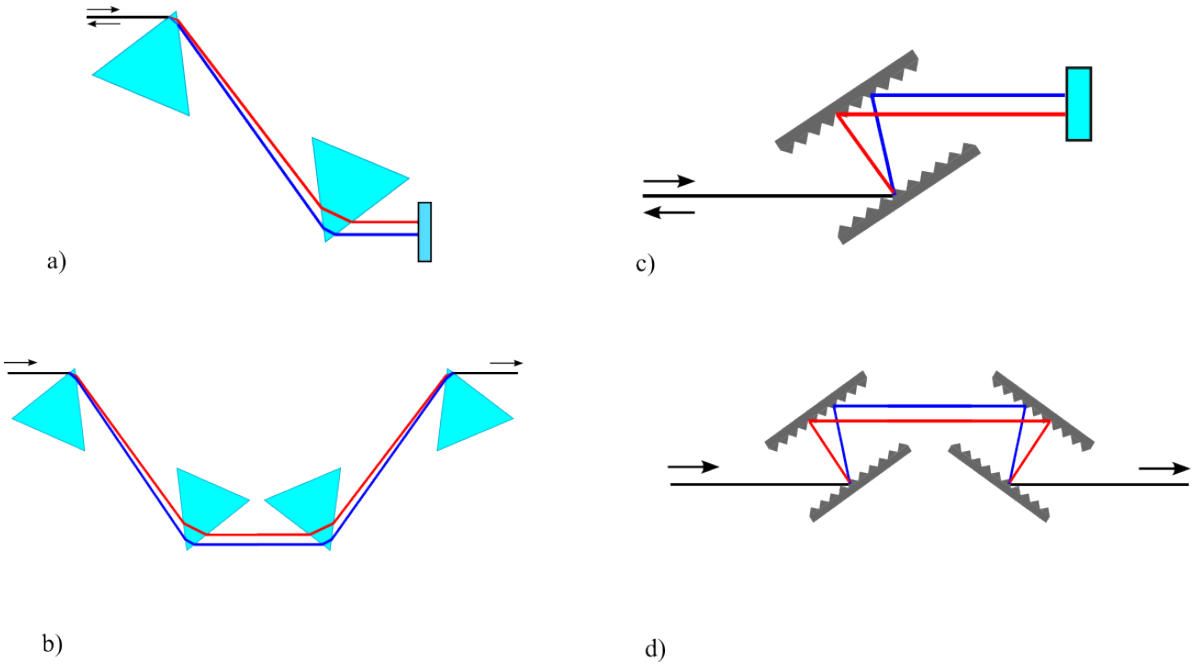


**Figure 2.4:** Pulse compression using a pair of prisms (a), four prisms (b), pair of gratings (c), four gratings (d). The long wavelength $\lambda_2$ part is illustrated as a red line, while the short wavelength $\lambda_1$ part is illustrated as a blue line.

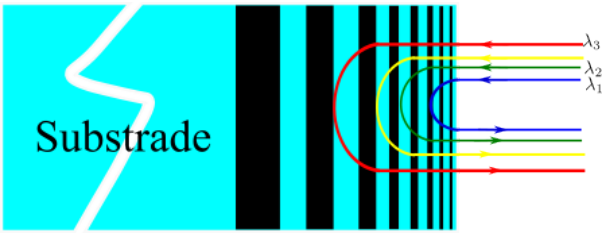


**Figure 2.5:** Bragg-Grating mirrors

## 2.2 Aberration of Ultrashort pulses

### 2.2.1 Basic principles of Fourier Optics

Signals in nature, like sound or light signals, appear in complicated forms. They may contain different frequencies and vary with time $f(t)$ in a way that it would be difficult to define them with concrete analytical expression. However, using harmonic analysis, it is possible to expand such a complex function in terms of the superposition of harmonic functions with different frequencies. These harmonic functions have a simpler form, making it easier to work with them. For example, $f(t)$ function can be expanded in terms of harmonics functions $G(\nu)\exp j2\pi\nu t$:

$$f(t) = \int_{-\infty}^{+\infty} G(\nu)\exp(j2\pi\nu t)\ d\nu \tag{2.16}$$

From this equation, the function $f(t)$ is decomposed by the linear combination (in this case, an integral) of elementary functions $\exp j2\pi\nu t$ and $G(\nu)$ is just a weighting factor that is applied to these elementary functions for obtaining the desired function $f(t)$. In equation 2.16, $G(\nu)$ is called **Fourier Transform of *f(t)*** and found using the following equation:

$$G(\nu) = \mathcal{F}\{f(t)\} = \int_{-\infty}^{+\infty} f(t)\exp(-j2\pi\nu t)\ dt \tag{2.17}$$

And equation 2.16 is called inverse Fourier Transform equation: $f(t) = \mathcal{F}^{-1}\{G(\nu)\}$.

Similarly, an arbitrary complex function $f(x, y)$ that depends on two independent variables $x$ and $y$ can be written as a superposition of the harmonic functions:

$$f(x,y) = \iint_{-\infty}^{+\infty} G(\nu_x,\nu_y)\exp[-j2\pi(\nu_x x + \nu_y y)]\,d\nu_x\,d\nu_y \tag{2.18}$$

where $\nu_x$ and $\nu_y$ are the spatial frequencies along $x$ and $y$ directions, respectively. The coefficients $G(\nu_x, \nu_y)$ are determined by the **two dimensional Fourier Transform**:

$$G(\nu_x,\nu_y) = \iint_{-\infty}^{+\infty} f(x,y)\exp[2\pi(\nu_x x + \nu_y y)]\,dx\,dy \tag{2.19}$$

And equation 2.18 is called the two-dimensional inverse Fourier Transform.

Similarly to the one-dimensional case, by looking at the equation 2.18, we can think the two-dimensional function $f(x, y)$ is a linear combination (integral in our case) of elementary functions of the form $\exp[j2\pi(\nu_x x + \nu_y y)]$. This function has exciting

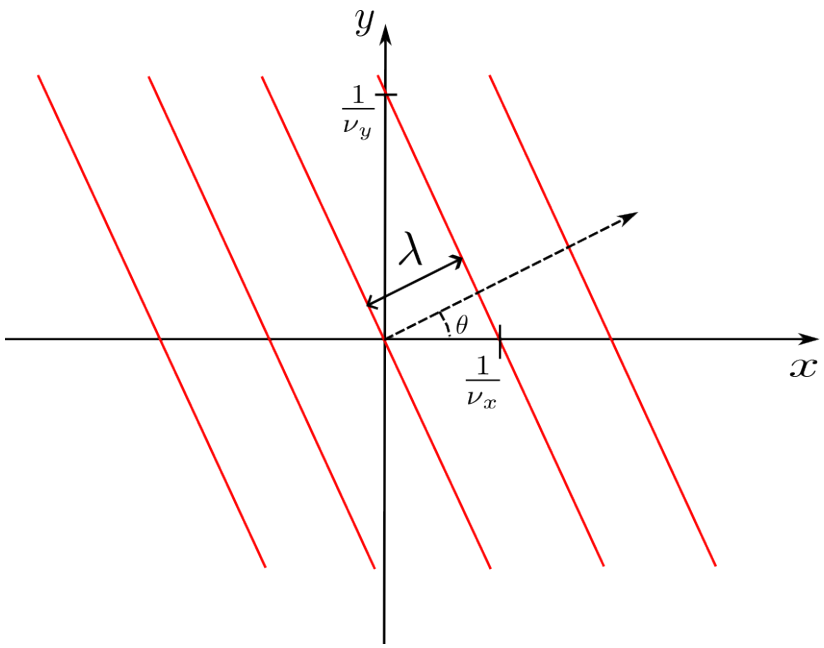


**Figure 2.6:** Lines of constant phase (in red) are directed at an angle for a given spatial frequencies. Image influenced by Ref. [18]

properties. The phase of that function equals either zero or integer multiple of radians: $2\pi(\nu_x x + \nu_y y) = n2\pi$. From that fact, one can find the equation.

$$y = -\frac{\nu_x}{\nu_y}x + \frac{n}{\nu_y} \tag{2.20}$$

Where $n$ is an integer. An illustration of this equation is given in figure 2.6. From that figure, we can regard that elementary functions are "directed" at angle $\theta$ (with respect to $x$) that depends on the spatial frequencies:

$$\theta = \arctan\left(\frac{\nu_y}{\nu_x}\right) \tag{2.21}$$

Using linearity and harmonic analysis, one can conclude the following fundamental statement of Fourier Optics: **any arbitrary wave can be considered as a sum of the elementary plane waves**.

### Transfer function of free space

We will be interested in the effect of the STCs after long propagation or at the focus. Diffraction theory allows us to find the field expression after propagation in any media. For linear systems, the general procedure is to convert the complex field to k space (or spatial frequency space), multiply it to a transfer function, and finally convert it back to the spatial coordinates[15].

General routine for the free space propagation calculations of the shift-invariant linear systems are given as the Rayleigh–Sommerfeld solution and can be written in a compact form [15]:

$$u_2(x,y) = \mathcal{F}^{-1}\Big\{\mathcal{F}\big\{u_1(x,y)\big\}H(\nu_x,\nu_y)\Big\} \tag{2.22}$$

where $u_1(x,y)$ -is a complex amplitude of the input plane, $u_2(x,y)$-is a complex amplitude of the output plane, and $H(f_x,f_y)$ - is so called transfer function.

The equation for the monochromatic complex plane wave is given by $U(x,y,z) = A\exp[-j(k_x x + k_y y + k_z z)]$ where $k_x, k_y$ and $k_z$ are the components of the *wavevector* $\mathbf{k}$, its modulus, known as *wavenumber*, $k = \sqrt{k_x^2 + k_y^2 + k_z^2}$. If we say that the plane wave propagates in free space along the $z$ direction and the given input plane wave located at $z = 0$ will be $u_1(x,y) = U(x,y,0) = A\exp[-j(k_x x + k_y y)]$, output plane wave located at $z = d$ will be $u_2 = U(x,y,d) = A\exp[-j(k_x x + k_y y + k_z d)]$. We can write the transfer function $H(\nu_x,\nu_y) = u_2(x,y)/u_1(x,y) = \exp(-jk_z d)$ or using $k_z = \sqrt{k^2 - k_x^2 - k_y^2} = 2\pi\sqrt{\lambda^{-2} - \nu_x^2 - \nu_y^2}$:

$$H(\nu_x,\nu_y) = \exp\Big(-j2\pi\sqrt{\lambda^{-2} - \nu_x^2 - \nu_y^2}\Big) \tag{2.23}$$

This equation is called the transfer function of free space.

The system is called linear when its response to several stimuli is equivalent to the sum of the responses to each stimulus.

**Fourier Transform properties of Lens**

To understand the spatial filtering and characterizations of the STCs, we need to understand the lens's Fourier transform properties.

Lets say plane wave with complex amplitude $u_1(x,y)$ propagates from $z = 0$ along the $z$ direction with small angles $\theta_x = \lambda\nu_x$ and $\theta_y = \lambda\nu_y$ and note its Fourier transform as $F(\nu_x,\nu_y) = \mathcal{F}\{u_1(x,y)\}$. Then, the wave will be focused into a point with coordinates $(\nu_x f_0, \nu_y f_0)$ in the focal plane. Assuming waves are paraxial (i.e., propagate with small angles to z) and using the Fresnel approximation, one can show that complex amplitude $u_2(x,y)$ at the output plane is [15]

$$\boxed{u_2(x,y) = h_l \exp\left[j\pi\frac{(x^2+y^2)(d-f_0)}{\lambda f_0^2}\right]F\left(\frac{x}{\lambda f_0},\frac{y}{\lambda f_0}\right)} \tag{2.24}$$

where, $\nu_x = x/\lambda f_0$ and $\nu_y = y/\lambda f_0$ were used and $h_l = H_0 h_0 = (j/\lambda f_0)\exp[-jk(d + f_0)]$, $f_0$- focal length of the lens. Thus, the complex amplitudes of front $u_1(x,y)$ and back $u_2(x,y)$ focal planes of the lens are related to each other by Fourier transform multiplied by the coefficient that is the function of coordinates $(x,y)$.

**Sampling theory**

Since the data analysis part of this project (section 3.2) uses the numerical Fast Fourier Transform, the short introduction of the sampling theory would be relevant to this work.

Fourier transform equation given in the formula 2.19 allows us to calculate the *continuous* functions. It is not always practical to use continuous functions for Fourier analysis. By converting these functions into a sequence of discrete functions, we can make them computer-readable. This conversion is done by using sampling and quantization.

A function $f(t)$ is called band-limited if its Fourier transform has zeros values outside of the integral $[-B, B]$ around the origin. Figure 2.7 a. is given an example of the Fourier transform of such a function.

One way to sample the continuous function $f(t)$ is to multiply it to the sampling function $s_{\Delta T} = \sum_{-\infty}^{+\infty} \delta(t - n\Delta T)$. The sampling function is just a sequence of impulse functions that are equally separated at a distance $\Delta T$. So multiplication $\tilde{f}(t) = f(t)s_{\Delta T}(t) = \sum_{-\infty}^{\infty} f(t)\delta(t - n\Delta T)$ will give us the *sampled function*. The Fourier transform of the sampled function:

$$\tilde{G}(\nu) = \mathcal{F}\{\tilde{f}(t)\} = \mathcal{F}\{f(t)s_{\Delta T}(t)\} = G(\nu) * S(\nu) \tag{2.25}$$

where $S(\nu) = (1/(\Delta T)\sum_{n=-\infty}^{+\infty} \delta\big(\nu - n/\Delta T\big)$ Fourier transform of the impulse train $s_{\Delta T}(t)$. Putting this equation and calculating the convolution integral in 2.25, we can find:

$$\tilde{G}(\nu) = \mathcal{F}\{\tilde{f}(t)\} = \frac{1}{\Delta T}\sum_{n=-\infty}^{\infty} G\big(\nu - \frac{n}{\Delta T}\big) \tag{2.26}$$

So from this equation, the Fourier transform of the *sampled function* $\tilde{f}(t)$ consists of *infinite*, *periodic* sequence of copies of $G(\nu)$ separated by distance $1/\Delta T$. Depending on $1/\Delta T$ value, the periods $\tilde{G}(\nu)$ will be critically close to each other - critically sampled; have a clean separation - oversampled; or will merge - undersampled. Discrete Fourier transform of the corresponding *sampled function* is illustrated in figures 2.7.

We told that the Fourier transform of the sampled function $\tilde{G}(\nu)$ is a continuous, periodic function with period $1/\Delta T$. Therefore, we need only one *complete* period in order to recover the original $f(t)$ function by taking the inverse Fourier transform. For extracting from $\tilde{G}(\nu)$ a single *complete* period that is equal to $G(\nu)$, we need to make sure that separation between the copies is sufficient. This sufficient condition is satisfied if $1/2\Delta T > B$ or

$$\Delta T < \frac{1}{2B} \tag{2.27}$$

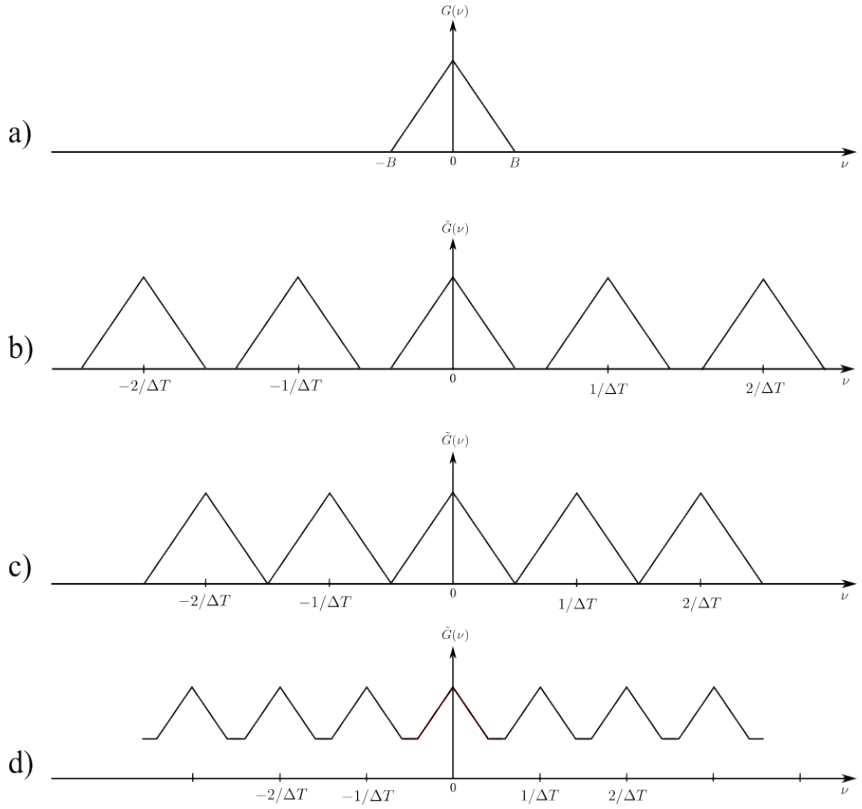


**Figure 2.7:** a) Fourier transform (FT) of bandlimited function, Transforms of corresponding b) oversampled function, c) critically sampled function, d)undersampled function. This illustration is adapted from [19].

This sampling theorem can be extended to the two-dimensional case: let's assume that function $f(x, y)$ is bandlimited, i.e., is zero outside of the rectangle $[-B_x, B_x]$ and $[-B_y, B_y]$, then this function can be fully recovered if the sampling intervals are satisfied:

$$\Delta X < \frac{1}{2B_x} \quad \Delta Y < \frac{1}{2B_y} \tag{2.28}$$

### Spatial filtering of images

The beam profile image of ultrashort pulses can be noisy due to dust in the reflecting mirrors or other components. Thankfully, we can filter the noises using Fourier analysis by removing parts of an image with higher frequency. In this work, we use spatial filtering to reduce the noise of the beam profile image and improve the homogeneity of the reference beam.

We can implement spatial filtering by following the steps: first, we need to take a two-dimensional Fourier transform of an image. This will allow us to see the spatial frequency components of an image. Then, we select only lower-frequency components that are limited to within a given radius. Then, we reimage using the inverse Fourier

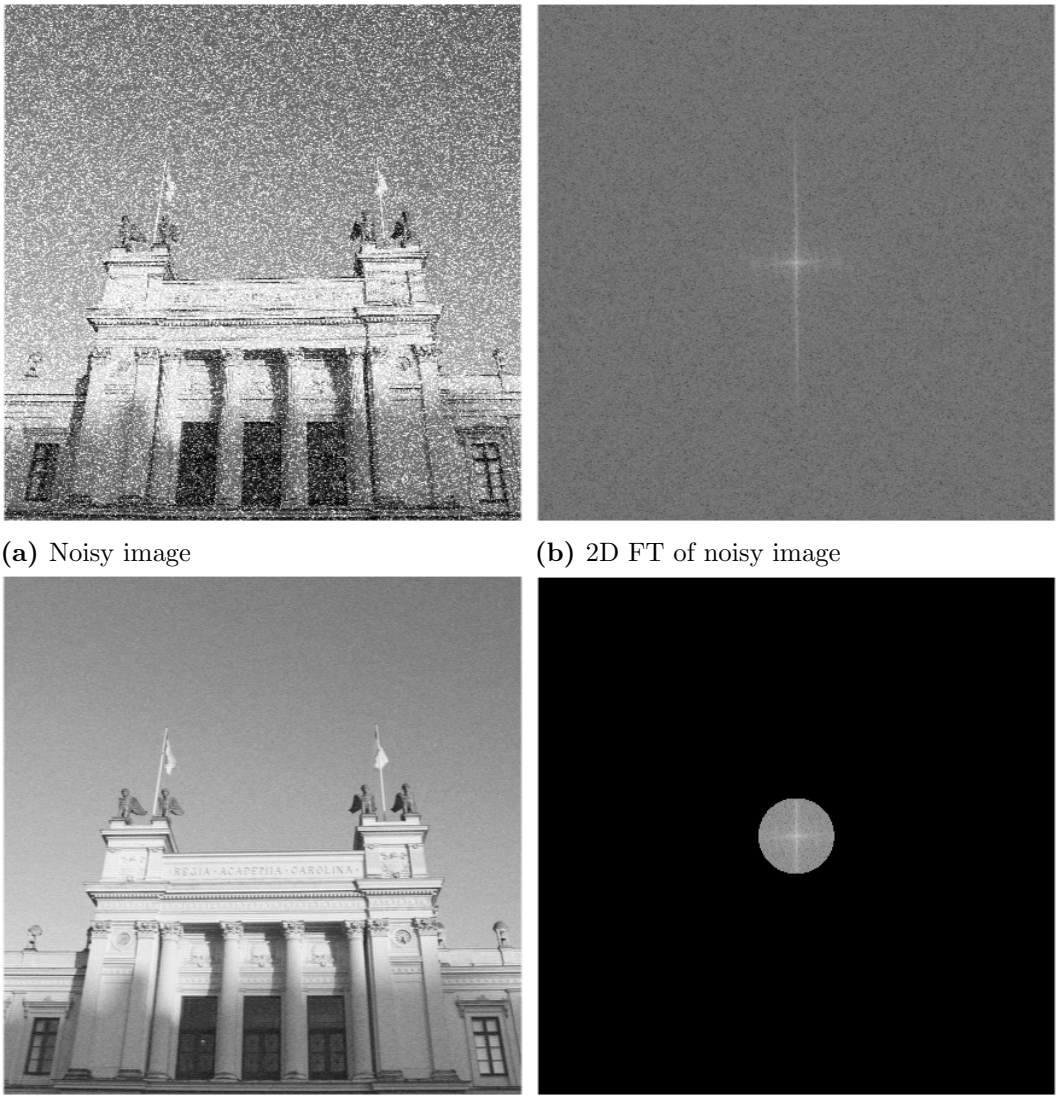

**(a)** Noisy image

**(b)** 2D FT of noisy image

**(c)** Image after low pass filter

**(d)** After applying low pass filter

**Figure 2.8:** Spatial filtering illustration. The right columns are image spectral magnitude (log scale). The right columns are corresponding images

transform. As a result, one can obtain a less noisy image. Figure 2.8 gives an example of noise reduction of an image by using spatial filtering.

### 2.2.2 Common types of aberrations

Chromatic aberrations are an integral part of this project. When broadband pulse passes through essential optical elements, they are highly likely to get aberrations. We try to avoid aberrations when we do the optical alignment of the system. In this work, we remove the common aberrations that are shared by all wavelengths. By describing and comparing aberrations of individual colors, we can obtain information about STCs. But before giving them characterization it is useful to get a general concept of common types of aberrations. In this subsection, we will give a brief introduction about them.

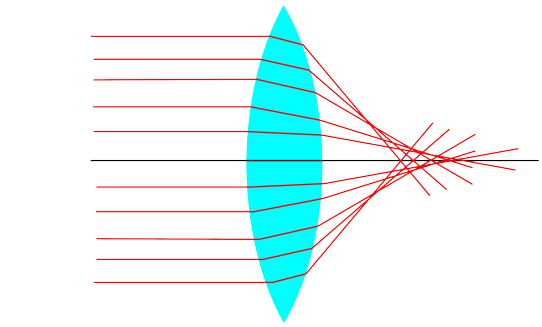

a) Spherical aberration

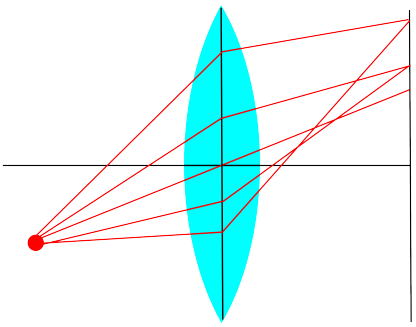

b) Coma

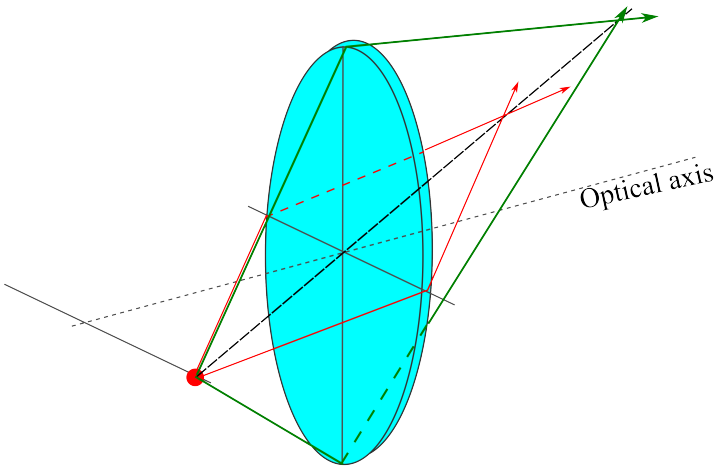


c) Astigmatism

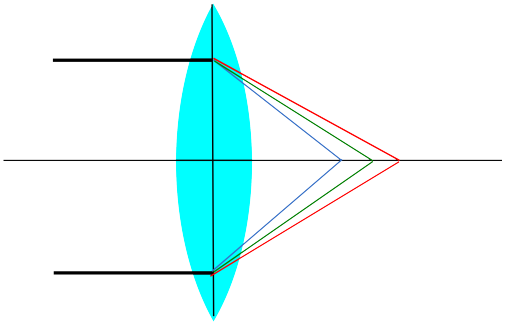

d) Chromatic aberration

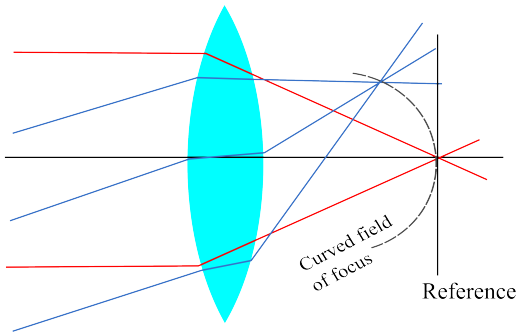


e) Field curvature

**Figure 2.9:** Common types of aberrations

In the real world, the wavefront of light rays deviates from the ideal mathematical paraxial approximation model. These phenomena are known as optical aberrations. They are caused by lens design, diffraction, refraction effects, and light's wave nature.

There are many aberrations, but we will limit our discussion to a few basic common types: spherical, astigmatic, field curvature, and chromatic aberration.

### Spherical aberration

Ideally, the lenses focus all the light into one plane. Still, when a spherical aberration is present, light comes into focus in a different plane, resulting in a so-called circle of confusion. In an ideal lens, the light wavefront maintains a perfect spherical wavefront, while spherical aberration results in the deviation from that spherical shape. In spherical aberration, focusing distances depend on where the rays interact with the lens (figure 2.9 a.). Because of the curved surface of the lens, rays that hit different points of the aperture will come at various angles of its surface. The steeper the angle, the more light will be deflected. Due to the larger angle of incidence lenses with large apertures (or smaller $f\#$), are more likely to suffer from spherical aberration.

Increasing the lenses' $f\#$ spherical aberration can be reduced. However, we need to remember that there is a limit to how much this can improve image quality.

### Coma

Coma is a type of aberration when off-axis *point* sources such as stars appear to have a tail, like a comet (figure 2.9 b). This occurs because of the imperfection in the lens or other components of the optical system.

This is an inherent property of parabolic mirrors when incoming rays have an angle to the parabola's axis. The greater the angle, the more coma aberration is noticeable.

### Astigmatic aberration

Rays coming off-axis points don't pass rotationally symmetric surfaces, including those coming from the half-vertical (tangential) plane and the half-horizontal (sagittal) plane (see Fig. 2.9 c). As a result, one of the directions will be in focus, but the other direction will be out of focus. This distortion is called astigmatic aberration. Since astigmatism occurs for off-axis sources, it depends on field angles. Astigmatism can be corrected if lenses are symmetric and field rays come from small angles.

#### Chromatic aberration

Chromatic aberration is caused by the wavelength dependence of the refractive index from which lenses are made. When light passes through the lens, different wavelengths of light are refracted at various angles and focused at different points. Longer wavelengths (red, for example) of light will have longer focal lengths than shorter wavelengths (blue, for example), as shown in figure 2.9 d.

Reflective optics or lenses made of several materials (i.e. doublet lenses or triplet lenses) can have zero or greatly reduced chromatic aberration.

#### Field Curvature

The curvature of the lens design results in the image plane being curved ( figure 2.9 e. This is known as field curvature aberration. In typical imaging lenses, the image plane will have a concave curvature.

We can use a negative lens near the image plane to compensate for the field curvature. These lenses are called field flatteners, and they allow us to drastically reduce the field curvature without affecting image size or introducing spherical aberration.

### 2.2.3 Zernike decomposition of wavefront

Characterization of the aberrated wavefront is possible with Zernike polynomials. Usually, optical systems have a circular aperture. A wavefront function $W$ defined over a unit circle can be written in terms of a linear combination of finite Zernike polynomials as:

$$W(R\rho,\theta) = \sum_{j=0}^{J} a_j Z_j(\rho,\theta) \tag{2.29}$$

where $R$ is the radius of the pupil, $0 \geq \rho \geq 1$, $J$ is the maximum number of terms of the polynomials, $a_j$ is the expansion coefficients, and $Z_j$ is the $j-th$ terms of Zernike polynomial. The first 15 normalized Zernike circle polynomials and their corresponding aberration are summarized in the following table. Here the $\int_0^{2\pi}\int_0^1 Z^2 \cdot \rho\, d\rho\, d\phi = \pi$ normalization is used:

Zernike polynomials have many useful properties:

- Expansion coefficients are independent from each other and can be found:

$$a_j = \frac{1}{\pi}\int_0^{2\pi}\int_0^1 W(\rho,\theta) Z_j \rho \mathrm{d}\rho \mathrm{d}\theta \tag{2.30}$$

| **OSA/ ANSI index** $j$ | $Z_j$ | **Classical name** |
|---|---|---|
| 0 | 1 | Piston |
| 1 | $1\ \rho\sin\phi$ | Vertical Tilt |
| 2 | $2\ \rho\cos\phi$ | Horizontal Tilt |
| 3 | $\sqrt{6}\rho^2\sin 2\phi$ | Oblique astigmatism |
| 4 | $\sqrt{3}\,(2\rho^2-1)$ | Defocus |
| 5 | $\sqrt{6}\rho^2\cos 2\phi$ | Vertical astigmatism |
| 6 | $\sqrt{8}\rho^3\sin 3\phi$ | Vertical trefoil |
| 7 | $\sqrt{8}\,(3\rho^3-2\rho)\sin\phi$ | Vertical coma |
| 8 | $\sqrt{8}\,(3\rho^3-2\rho)\cos\phi$ | Horizontal coma |
| 9 | $\sqrt{8}\rho^3\cos 3\phi$ | Oblique trefoil |
| 10 | $\sqrt{10}\rho^4\sin 4\phi$ | Oblique quadrafoil |
| 11 | $\sqrt{10}\,(4\rho^4-3\rho^2)\sin 2\phi$ | Oblique secondary astigmatism |
| 12 | $\sqrt{5}\,(6\rho^4-6\rho^2+1)$ | Primary spherical |
| 13 | $\sqrt{10}\,(4\rho^4-3\rho^2)\cos 2\phi$ | Vertical secondary astigmatism |
| 14 | $\sqrt{10}\rho^4\cos 4\phi$ | Vertical quadrafoil |

**Table 2.1:** Zernike Polynomials

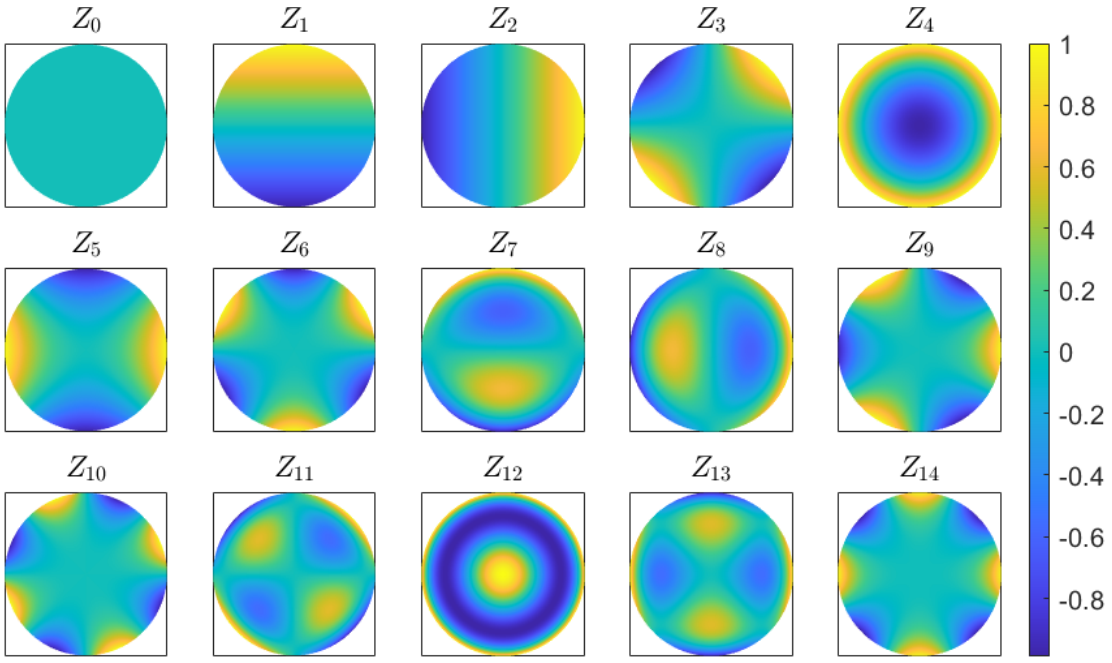


**Figure 2.10:** The first 15 Zernike Polynomials starting from $0^{th}$ term to $14^{th}$ term under OSA/ANSI indexing

- All Zernike terms except the piston term have a mean value of zero; thus, the mean value of the wavefront is equal to the piston coefficient:

$$\bar{W}(\rho,\theta)=\frac{1}{\pi}\int_{\Sigma}W(\rho,\theta)\rho\mathrm{d}\rho\mathrm{d}\theta=a_0 \tag{2.31}$$

- The variance is equal to the square of each expansion coefficient, excluding the

piston coefficient:

$$\begin{aligned}\sigma^2 &= \frac{1}{\pi}\int_0^{2\pi}\int_0^1 [W(\rho,\theta) - \bar{W}(\rho,\theta)]^2 \rho \mathrm{d}\rho \mathrm{d}\theta \\ &= \overline{W^2} - (\bar{W})^2 = \sum_{j=1}^{\infty} a_j^2\end{aligned} \tag{2.32}$$

**Strehl ratio**

The aberration of the beam decreases its intensity at the focus. We can characterize this reduction of intensity by a quantity called Strehl ratio, which is defined as the ratio of the intensity $I$ of the aberrated beam, divided by the intensity of the $I_0$ of aberration-free beam:

$$\text{Strehl ratio } = \frac{I}{I_0} = \frac{1}{\pi^2}\left|\int_0^{2\pi}\int_0^1 \exp[\mathrm{i}2\pi W(\rho,\theta)]\rho \mathrm{d}\rho \mathrm{d}\theta\right|^2, \tag{2.33}$$

## 2.3 Amplification of Ultrashort pulses

Most high-intensity laser systems have amplification stages based on Chirped Pulse Amplification (CPA) or Optical Parametric Chirped Pulse Amplification (OPCPA) techniques. These techniques are based on chromatic elements, which can potentially cause STCs. Since we are characterizing the laser systems based on these techniques, a short introduction to them is relevant to this work.

Amplification techniques have been established for pulses with different durations. For picosecond and nanosecond pulses, their energy can be increased by passing them through a gain medium. However, it has been challenging to do the same for femtosecond (fs) pulses. Because in the case of ultrashort extremely high-intensity fs pulses, many non-linear effects occur in the gain medium. For example, at high intensities, the refractive index of the medium in the transverse direction will depend on the intensity $n = n(I)$, creating the self-phase modulation (SPM) and eventually self-lensing (Optical Kerr effect). SPM will change the pulse spectrum and self-lensing the beam profile modulation, even damaging the crystal. This was a limiting factor of the ultrashort power amplification. The introduction of the chirped pulse amplification in 1985 by Strickland and Mourou [2] has revolutionized the ultrafast science and allowed us to push the amplification limit up to the PW level.

### 2.3.1 Chirped Pulse Amplification

The main idea of CPA is to stretch a fs pulse from an oscillator up to 10,000 times, increasing its duration but decreasing its power. Then, this pulse is amplified by linear amplification and thereafter recompressed. In the end, we can obtain the pulse with

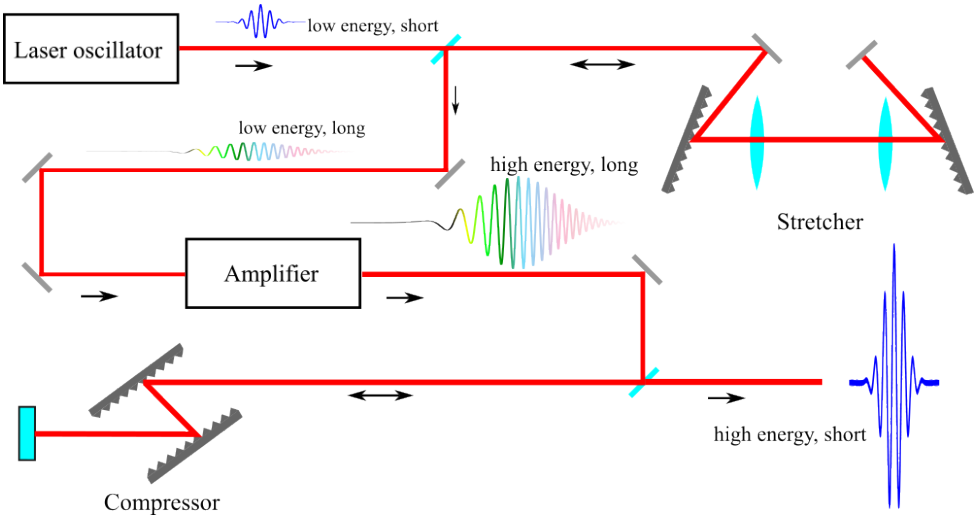


**Figure 2.11:** Illustration of Chirped Pulse Amplification (CPA) Scheme adapted from [2]

the same duration but with high power. A combination of gratings and a telescope can stretch the pulse. To amplify the stretched pulse, we need to use an amplifier that satisfies two crucial conditions: its bandwidth must exceed the pulse's bandwidth that is amplified, and the amplifier must not be saturated [2].

## 2.4 Spatio-Temporal Couplings (STC)

This section gives the theoretical background of spatial-temporal couplings (STC), which is the core part of this project. The main content of this section is influenced by classical papers about the general theory of STCs by Akturk et al. [20] and Jolly et al. [1]. This section is divided into four subsections: pulse front tilt (subsection 2.4.1), pulse front curvature (subsection 2.4.2), STC at different Fourier domains (subsection 2.4.3) and Multi-pass-cell (MPC) compression technique. The first two subsections give a detailed description of first-order couplings with the derivations of important formulas. Then, the subsection 2.4.3 gives a wave-optical description of the STC at different Fourier domains in the example of the Gaussian pulse. The MPC is briefly introduced in the last subsection.

In section 2.1.1, we described the ultrashort pulse only in the time and frequency domain. To fully describe the pulse, we also need to know the pulse in the spatial domain. It has been assumed that all spatial part of the wave equation evolves with time (or frequency) similarly so that we can describe the pulse as a multiplication of spatial and temporal (or frequency) parts: $U(\mathbf{r}, t) = U(\mathbf{r}) \cdot U(t)$. However, this assumption fails in the case of the ultrashort (broadband) pulses. Spatial and temporal (or frequency) parts of the wave equation become dependent (or coupled)on each other for ultrashort pulses so that we no longer can separate the wave equation into spatial and temporal (or frequency) parts: $U(\mathbf{r}, t) \neq U(\mathbf{r}) \cdot U(t)$. This phenomenon is known as **Spatio-Temporal Couplings (STC)** or spatio-temporal distortions [1].

Angular dispersion (AD), Pulse front tilt (PFT), and pulse front curvature (PFC) are

common examples of the STC. In this section, we will discuss these couplings in more detail. STC is caused by the main feature of the ultrashort pulse—its broadband spectrum. Common sources of STC are optical chromatic elements: lenses, prisms, and gratings.

### 2.4.1 Pulse front tilt (PFT)

Pulse front tilt (PFT) is defined as the difference in the time of arrival of the pulse in a given plane perpendicular to the propagation direction. It commonly occurs in the configuration where the angular dispersion exists, i.e., when the propagation angle is linearly dependent on optical frequency, for example, in prisms and gratings.

When the pulse passes through a prism with refractive index $n$ and angle $\alpha$, due to a linear increase in the thickness of the prism, the beam will experience different group delays in the transverse direction. Let's consider the pulse that goes from plane $AB$ to plane $A'B'$. The time that it takes for the pulse front for path $AA'$ is $T_g = AA'/v_g$ while for the phase front $T_p = AA'/v_p$, where $v_p-$ phase velocity, $v_g-$ group velocity given in the equation 2.13. If the beam propagates through nondispersive material, then $v_p = v_g$ pulse font and wavefront would travel the same distance at a given time period. However, the phase front and pulse front become separated when the pulse propagates in a dispersive medium. The time difference between the pulse front and phase front will give us the introduced group delay ($GD$):

$$T = T_g - T_p = \frac{AA'}{v_g} - \frac{AA'}{v_p} = \frac{nl_0}{c} - \frac{l_0}{c}(n - \frac{dn}{d\lambda}\lambda_0) = \frac{l_0\lambda_0}{c}\frac{dn}{d\lambda} \tag{2.34}$$

where, $\lambda_0-$ central wavelength. Using $l_0 = x\tan\alpha$ we can find that:

$$\boxed{T(x) = \frac{\lambda_0 \tan\alpha}{c}\frac{dn}{d\lambda}x} \tag{2.35}$$

As we can see from this equation, the accumulated group delay linearly increases with transverse distance $x$, resulting in the rotation of the pulse front because part of the pulse closer to the prism's upper edge will experience less group delay than the part below. The angle difference $\delta$ between phase front and pulse front gives us Pulse Front Tilt (PFT). This tilt angle can be found from triangle $\tan\delta = a/D$, where $D-$ width of the beam, $a = cT(x)$ using that we on can find

$$\tan\delta = \frac{\lambda_0 x \tan\alpha}{D}\frac{dn}{d\lambda} \tag{2.36}$$

It is important to note that a general relation exists between angular dispersion $d\theta/d\lambda$ and the tilt angle $\delta$ [21], where $\theta(\lambda)-$ is called the deviation angle (see fig. 2.12 b.).

$$\tan\delta = \lambda_0\left|\frac{d\theta}{d\lambda}\Big|_{\lambda_0}\right| \tag{2.37}$$

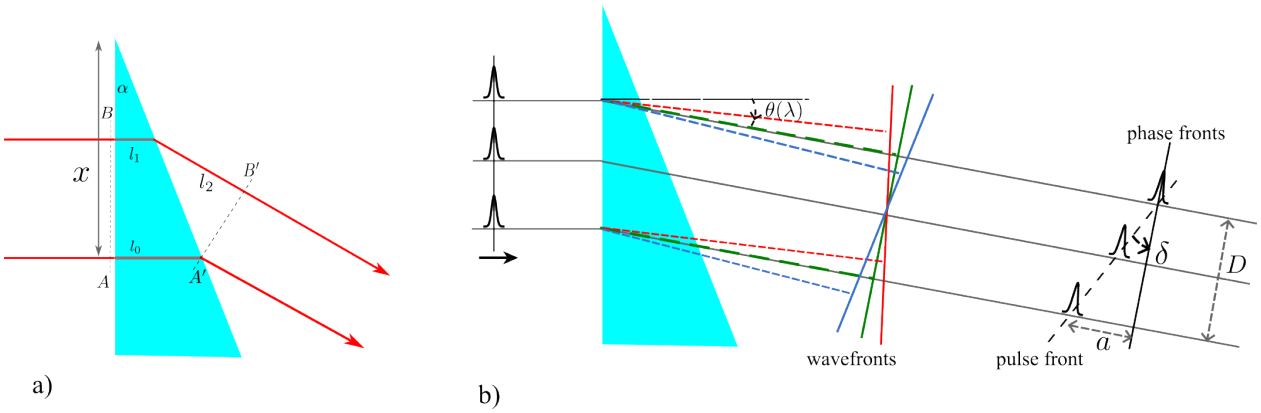


**Figure 2.12:** Pulse front tilt introduced by prisms

Gratings also introduce pulse front tilt. We can verify it using the sketch given in figure 2.13.

It has been shown that simultaneous temporal chirp and spatial chirp of the pulse also yield PFT [20] even if there is no angular dispersion (AD). For example, when a spatially chirped input pulse propagates through a dispersive medium in the output, we obtain the spatially chirped pulse with pulse front tilt.

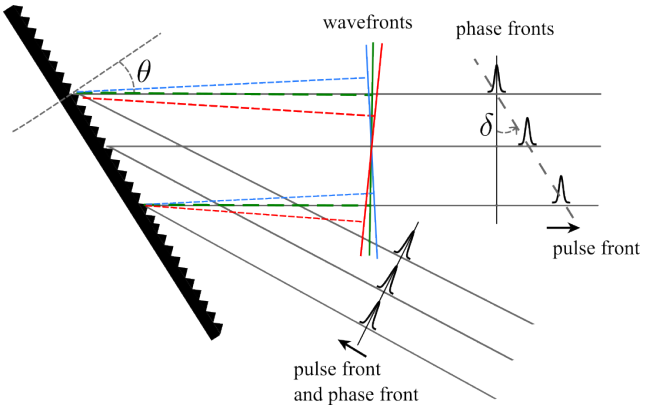


**Figure 2.13:** PFT introduced by gratings

### 2.4.2 Pulse front curvature (PFC)

As we discussed in subsection 2.2.2, when the pulse passes through the lens, it's affected by chromatic aberration. We can look at this as the achromatic lens curves the wavefront of different colors differently, known as chromatic curvature (CC). Let's consider pulse propagation in the temporal domain. The pulse will get a different group delay in the transverse direction due to the varying thickness of the lens in a radial direction. If the thickness of lens $L(r)$, then the time that it takes for the phase front is $T_p = L(r)/v_p$, while for pulse front is $T_g = L(r)/v_g$. The varying thickness of the lens $L(r)$ can be found by using the formula for the lens and paraxial approximation:

$$L(r) = \frac{a^2 - r^2}{2f(n-1)} \tag{2.38}$$

where, $a-$ radius of the aperture of lens, $r-$ radial distance from the optical axis of lens, $f-$ focal lenghts of lens. Using this equation and equations for phase and group velocity, we can find the group delay as follows:

$$\boxed{T(r) = \frac{a^2 - r^2}{2f(n-1)} \frac{\lambda_0}{c} \frac{dn}{d\lambda}} \tag{2.39}$$

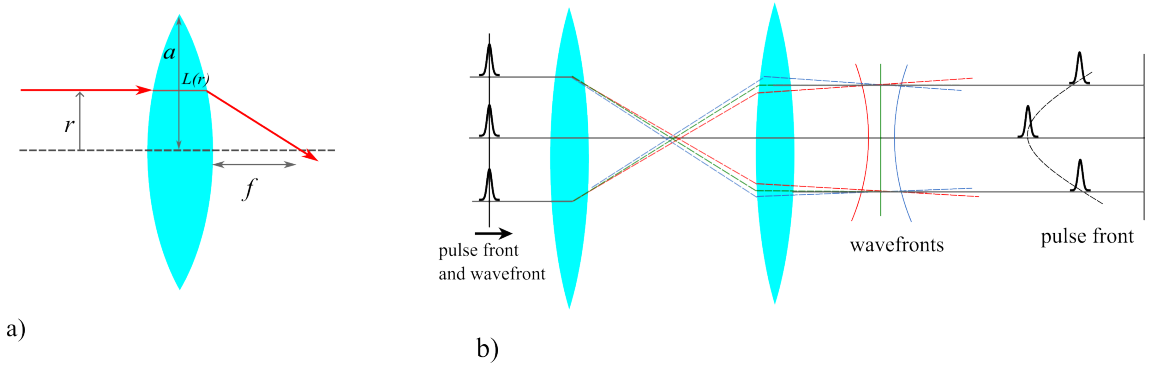


a) b)

**Figure 2.14:** The derivation of group delay using paraxial approximation a), PFC introduced by the lens b)

As we can see from this equation, the introduced group delay varies quadratically in the radial $r$ dimension, resulting in pulse front curvature in the output.

The Spatio-Temporal Couplings are neither good nor bad. In some cases we want to avoid it, in other cases we intentionally introduce depending on the applications. For example, in CPA, we know that gratings/prisms are used for compression; they are, in turn, introducing large amounts of PFT. However, they are constructed to have no PFT in the output. Even small misalignments in this system will cause large amounts of PFT, which will be detrimental to the intensity of the focus.

### 2.4.3 STC at different Fourier domains

In section 2.1.1, we wrote the spatial and temporal parts of the ultrashort pulse separately, i.e., the spatial part was only dependent on spatial coordinates, and the temporal part was dependent only on time. However, we already noted that in the case of STC, these parts become dependent on each other. For the more general case, when there is STC, we can describe the pulse in the following way [22]:

$$U(x,y,t) = |U(x,y,t)|exp\{j\phi(x,y,t)\} \tag{2.40}$$

where $|U(x,y,t)|-$ spatially resolved amplitude, $\phi(x,y,t)$ spatially resolved phase. We can see from this description that the amplitude is also dependent on time, and the phase is also dependent on spatial coordinates in contrast to our previous description in section 2.1.1 i.e., they are coupled to each other. Similarly, we can describe the pulse more generally in the spectral domain by taking the Fourier transform of equation 2.40: $\tilde{U(x,y,\omega)} = |\tilde{U}(x,y,\omega) = |\tilde{U}(x,y,\omega)|exp\{j\psi(x,y,\omega)\}$.

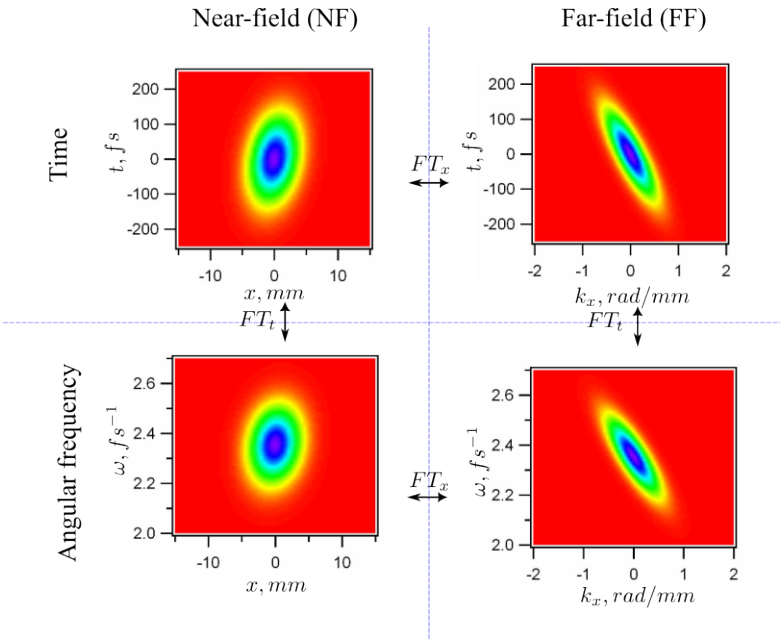


**Figure 2.15:** STC characterization in four domains: $(x,t)$, $(x,\omega)$, $(k_x,t)$ and $(k_x,\omega)$ related with each other by Fourier transform. Image is adapted from paper [22]

When we characterize ultrashort pulses, it is convenient to define two planes: the plane where we measure the collimated beam - *near-field* (NF) and the plane where we focus the pulse (or propagate to far distance) - *far-field* (FF). This introduction of two planes adds complexity to our description. Now, we can describe the pulse in four different domains related to each other by Fourier transforms. The explicit relations between these domain descriptions are well described in paper [22].

A simpler mathematical derivation of the STC in different domains is given in the appendix of paper [1]. If we consider the beam only in one transverse $x$ direction and assume that its arrival time $t_0(x)$ is dependent on that transverse direction, then we describe the beam:

$$U(x,t) = f(x)g[t - t_0(x)]\exp\{j\omega_0 t\} \tag{2.41}$$

where, $f(x)-$ describes the spatial envelope, $g(t)-$ is a temporal profile. We will use the Fourier transform to convert this equation to the spectral domain. But before that, we will rewrite this equation in the following form:

$$U(x,t) = f(x)[g(t) \circledast \delta[t - t_0(x)]] \cdot \exp\{j\omega_0 t\} \tag{2.42}$$

here we denote $\circledast-$ for convolution. The Fourier transform of then becomes:

$$\begin{aligned} \tilde{U}(x,\omega) &= f(x)[\tilde{g}(\omega) \cdot \mathcal{F}\{\delta[t - t_0(x)]\}] \circledast \mathcal{F}\{\exp\{j\omega_0 t\}\} \\ &= f(x)\tilde{g}(\omega - \omega_0)\exp\{j(\omega - \omega_0)t_0(x)\} \end{aligned} \tag{2.43}$$

Assuming the pulse spatial distribution is a Gaussian $f(x) \propto \exp(-x^2/\sigma_x)$. Simil-

arly, we will assume the temporal and spectral distribution is also Gaussian $g(t) = \exp\{-4\log 2 \cdot (t/\tau_0)^2\}$ and $\tilde{g}(\omega) \propto \exp\{-\tau_0^2\omega^2/(4\pi)\}$. Putting all of these equations into equation 2.41, we can find our final equation for describing the pulse in $(x,t)$ representation:

$$U(x,t) \propto \exp\Big\{-\frac{x^2}{\sigma_x} - 4\log 2 \cdot \Big(\frac{t-t_0(x)}{\tau_0}\Big)^2\Big\}\exp\{j\omega_0 t\} \tag{2.44}$$

Similarly putting Gaussian profile equations into equation 2.43, we will find our final formula for the $(x,\omega)$ representation:

$$\tilde{U}(x,\omega) \propto \exp\Big\{-\frac{x^2}{\sigma_x} - \frac{\tau_0}{4\pi}(\omega-\omega_0)^2\Big\}\exp\{j(\omega-\omega_0)t_0(x)\} \tag{2.45}$$

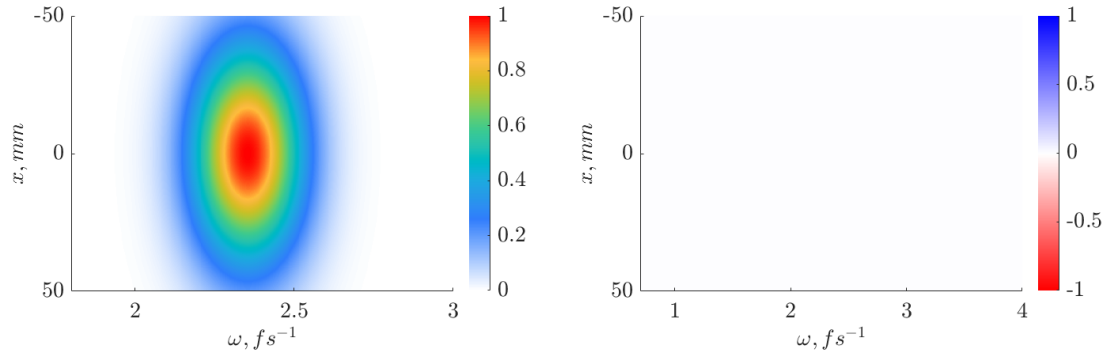


**(a)** Amplitude STC free pulse pulse in $(x,\omega)$ representation

**(b)** Phases of the STC free pulse in $(x,\omega)$ representation

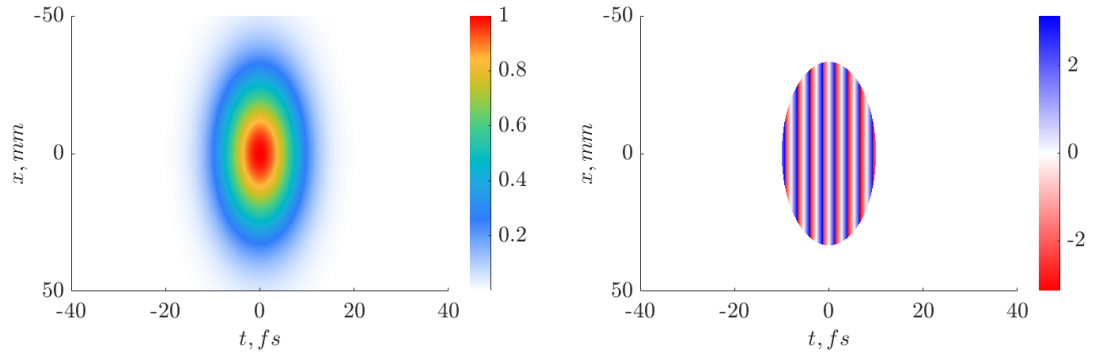


**(c)** Amplitude of the STC free pulse $(x,t)$ representation

**(d)** Phases of the STC free pulse in $(x,t)$ representation

**Figure 2.16:** Simulations of the STC free pulse in the NF (collimated beam) at different representations. Here, the pulse with central wavelength $\lambda = 800nm$, pulse duration $20fs$ were used

If we omit the arrival time dependence on transfer distance, i.e., $t_0(x) = 0$, we can simulate the STC free pulse using equations 2.44 and 2.45 at different near-field domains given in figure 2.16. If no spatial-temporal distortions are present, then the amplitude change in $(x,t)$ configuration spatial change over time is symmetric, as we can see from figure 2.16c.

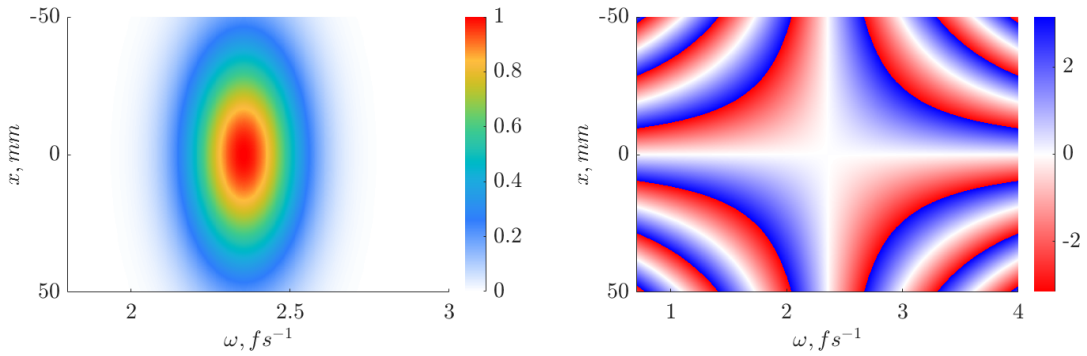


**(a)** Amplitude of the pulse with PFT in $(x, \omega)$ representation

**(b)** Phases of the pulse with PFT in $(x, \omega)$ representation

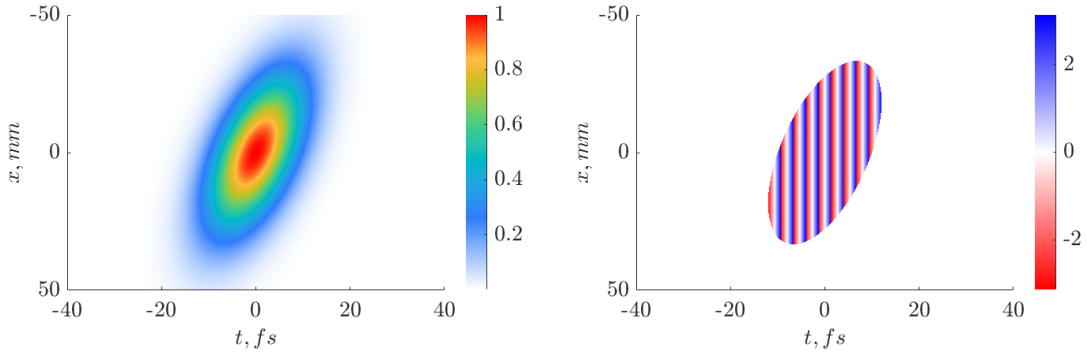


**(c)** Amplitude of the pulse with PFT in $(x, t)$ representation

**(d)** Phases of the pulse with PFT in $(x, t)$ representation

**Figure 2.17:** Simulations of PFT in the NF (collimated beam) at different representations. Here, the pulse with central wavelength $\lambda = 800nm$, pulse duration $20fs$ with pulse front tilt coefficient $\gamma = 0.5mm/fs^{-1}$ were used

In the case of PFT, the arrival time $t_0(x)$ is dependent on the transverse $x$ dimension. We found this dependence is given in equation 2.35. Noting the constant values in that equation as $\gamma = (\lambda_0 \tan\alpha/c)(dn/d\lambda)$, we write it in a simpler form:

$$t_0(x) = \gamma x \tag{2.46}$$

where, $\gamma-$ is a PFT coefficient. We can simulate amplitude at different near-field domains, inserting this equation into equations 2.44 and 2.45 (figure 2.17). Looking at figure 2.17c, we can see the amplitude (or intensity) in $(x, t)$ representation is tilted. We can also observe this in $(x, t)$ phase representation by looking at figure 2.17d. The front is tilted relative to the phase front direction.

Also, using equations 2.46 and 2.45 we can find the equation for the spectral phase:

$$\psi(x, \omega) = \gamma(\omega - \omega_0)x \tag{2.47}$$

This phase is plotted in figure 2.17b and can be understood in two ways. On the one hand, this can be seen as a phase varying linearly in frequency, with a slope $d\psi/d\omega$, that varies linearly with position: this describes PFT. On the other hand, this can

be seen as a phase varying linearly in position (i.e. a wavefront tilt) with a slope that varies linearly with frequency: this describes angular dispersion (AD). It is not surprising because, as we said before, any element that introduces angular dispersion (AD) (prisms, gratings) gives PFT (eq. 2.37). Then, we can conclude that **PFT and AD correspond to the description of the same pulse but are considered in different spaces**. This means that PFT (time-domain description) is equivalent to frequency-dependent wavefront tilt (frequency-domain description).

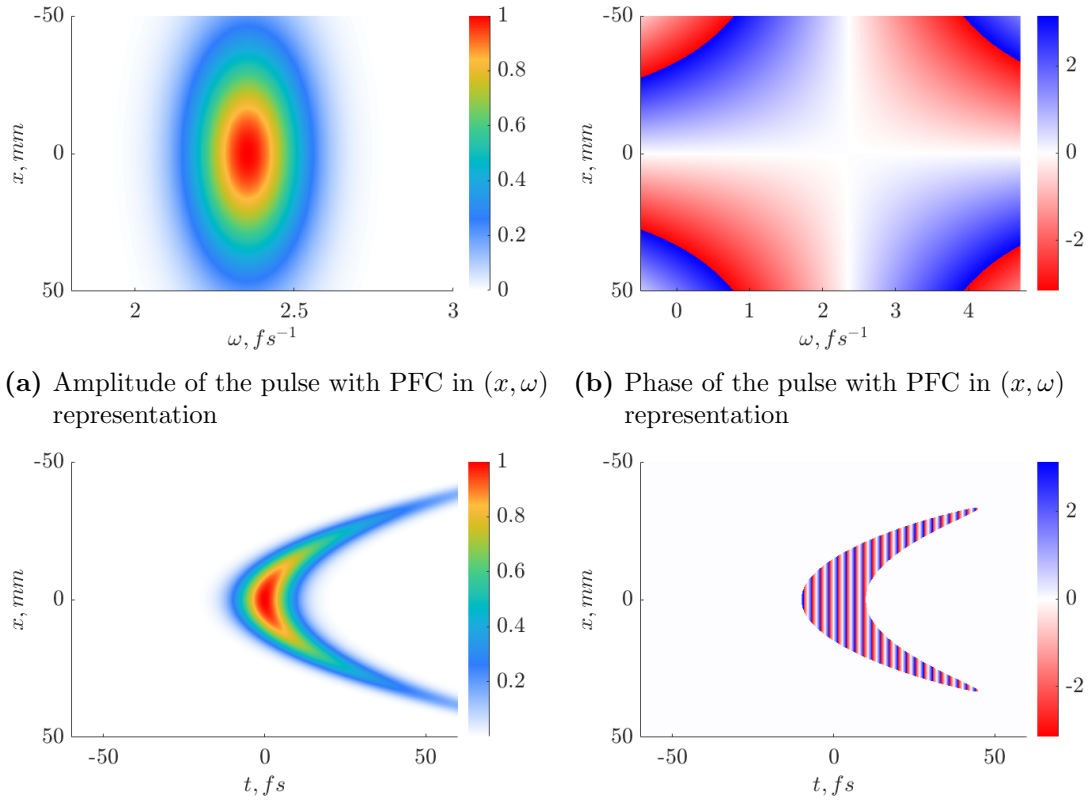


**(a)** Amplitude of the pulse with PFC in $(x, \omega)$ representation

**(b)** Phase of the pulse with PFC in $(x, \omega)$ representation

**(c)** Amplitude of the pulse with PFC in $(x, t)$ representation

**(d)** Phases of the pulse with PFC in $(x, t)$ representation

**Figure 2.18:** Simulations of PFC in the NF (collimated beam) at different representations. Here, the pulse with central wavelength $\lambda = 800nm$, pulse duration $20fs$ with pulse front curvature coefficient $\alpha = 0.04mm/fs^{-1}$ were used

Figures 2.18 gives the simulations of the PFC at different representations. In the case of the PFC, the time of arrival $t_0(x)$ depends on the traverse direction quadratically as we derived before in equation 2.39. Noting constant values as $\alpha$ we can write:

$$t_0(x) = \alpha x^2 \tag{2.48}$$

where $\alpha-$ is a pulse front curvature constant. Using this equation, we can find the spectral phase in $(x, \omega)$ representation:

$$\psi(x, \omega) = \alpha(\omega - \omega_0)x^2 \tag{2.49}$$

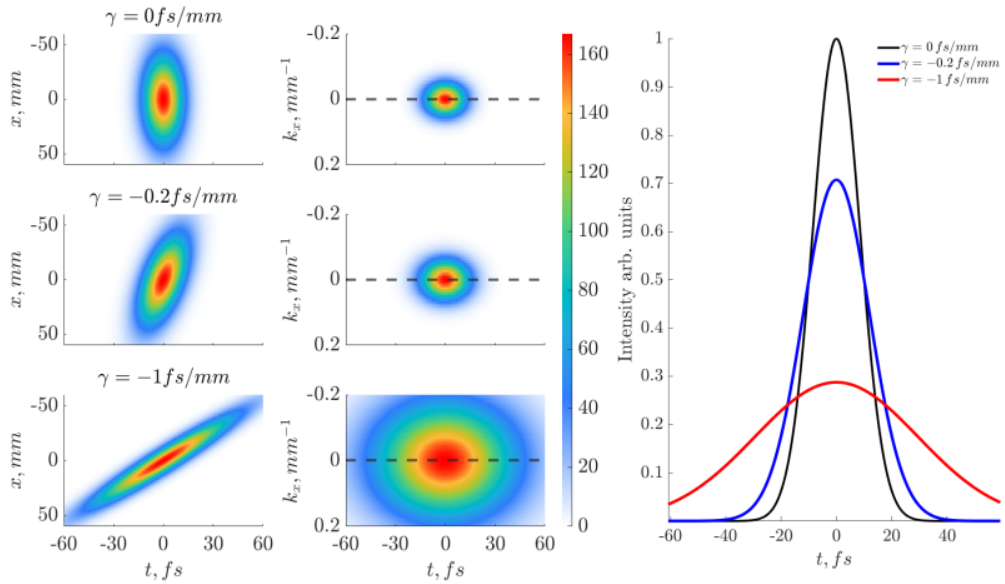


**Figure 2.19:** Pulse front tilt simulations in the NF and FF: a) STC free Gaussian pulse ($\gamma = 0$), b) Pulse with PFT $\gamma = -0.2\, fs/mm$, c) PFT $\gamma = -0.5\, fs/mm$ d) Intensity values in the far field taken along the dashed line. With an increase in PFT, the pulse duration increases and intensity decreases

The plot of this phase is given in figure 2.18b. Again, we can see this in two ways. On the one hand, the linear spectral phase with a slope that varies with position quadratically: this is PFC. On the other hand, the quadratic spatial phase (wavefront curvature) varies linearly with frequency: this is chromatic curvature (CC) [1]. As we described before, PFC is introduced by the chromatic lens which curves the wavefronts differently for different frequency components (chromatic curvature). Thus, we infer that the PFC (time-domain description) is equivalent to frequency-dependent wavefront curvature (frequency-domain description). So with that, we conclude that **PFC and CC correspond to the description of the same pulse but are considered in different spaces**.

We can find the far-field (FF) (i.e., intensity at the focus plane or the plane located far away) description of the pulses by taking spatial Fourier transform of equations 2.41 and 2.43 at the end will give us fields in the conjugate $k_x$ space: $U_k(k_x, t)$ and $\tilde{U}_k(k_x, \omega)$. Suppose the pulse has AD/PFT in the NF, in the FF (after some propagation or after focusing). In that case, it will focus different colors differently in the transverse direction, known as "transverse spatial chirp." 2.21. This will increase the focal spot size in the focus, resulting in an intensity drop at the focus, shown in figure 2.19. Moreover, the wavefront in the FF will have a peculiar form known as "wavefront rotation."

If the pulse has CC/PFC in the NF, it will cause an intensity to drop and pulse duration to increase like PFT shown in figure 2.20. Moreover, CC/PFC must result in a different best-focusing position in the longitudinal dimension of the FF since the chromatic curvature results in different radii of curvature of different frequency components 2.22. This effect is known as *Longitudial Chromatism* or *Flying focus*.

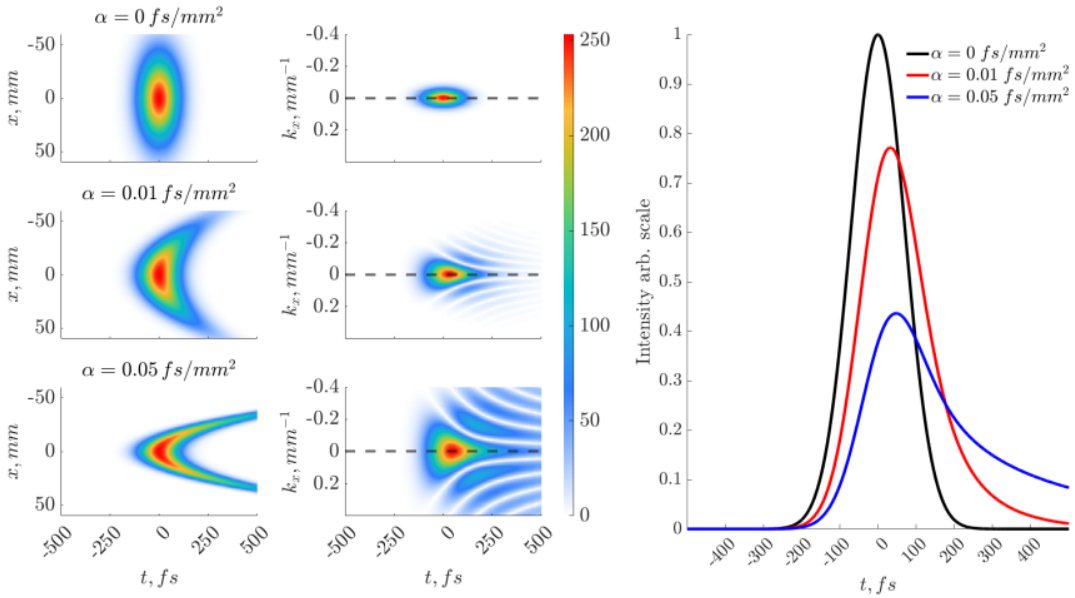


**Figure 2.20:** Pulse front curvature simulations in the NF and FF: a) STC free Gaussian beam ($\alpha = 0$), b) PFC with $\alpha = 0.01 fs/mm^2$, c) PFC with $\alpha = 0.05$, d) Intensity taken along the dashed lines. With the increase of the PFC, intensity decreases and pulse duration increases

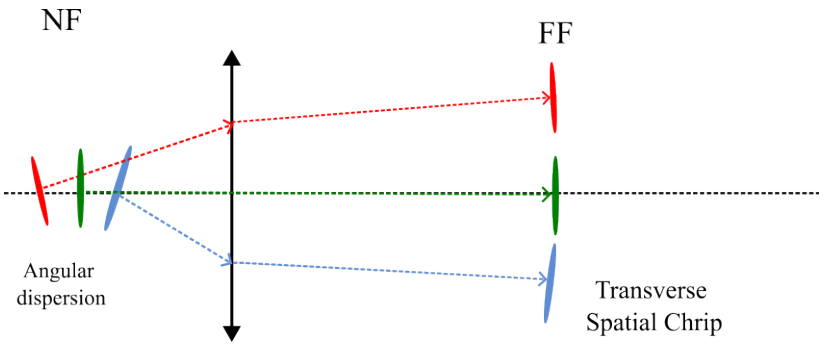


**Figure 2.21:** Angular dispersion (AD) in the NF results in Transverse Spatial Chirp in the FF

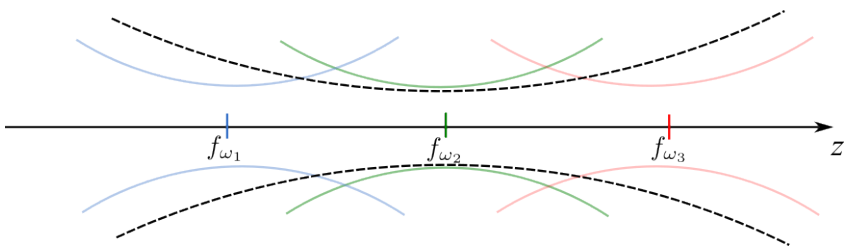


**Figure 2.22:** CC/PFC in the NF results in Longitudinal Chromatism in the FF

We can summarise the first and second-order STC at different domains in the following table:

| | Fourier Domain | First order couplings | Second order couplings |
|---|---|---|---|
| NF | $(x, \omega)$ | Angular Dispersion (AD) | Chromatic Curvature (CC) |
| | $(x, t)$ | Pulse front tilt (PFT) | Pulse Front Curvature (PFC) |
| FF | $(k_x, \omega)$ | Transverse Spatial Chirp | Longitudial Spatial Chirp |
| | $(k_x, t)$ | Wavefront rotation | Flying focus |

### 2.4.4 Multi-pass cell compression

As mentioned before, one of the goals of this project is to give STC characterization of the Multi-pass cell compression (MPC) system based on the German Electrons (DESY). Because of that, the basic knowledge of the MPC technique is essential for this project.

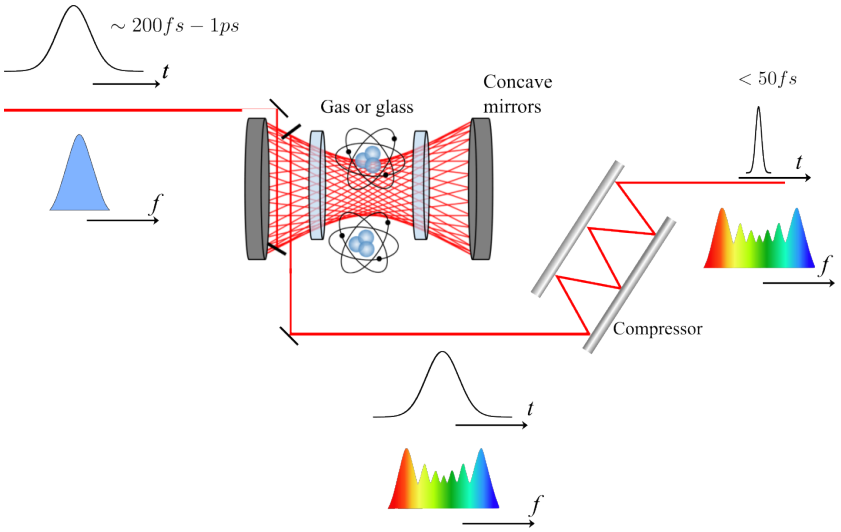


**Figure 2.23:** Basic setup for MPC technique. Adapted from paper [23]

Multi-pass cell compression (MPC) is a post-compression method that achieves sub 50 fs short pulses with kW average power level. The practical realization of this method is relatively simple: we need only two curved mirrors and a Kerr medium between them. The Kerr medium can be a solid or a gas. Stability for beam pointing, high tolerance for minor mismatches, and compactness make them attractive for both scientific and commercial laser systems[23].

Herriot-type MPCs are the most commonly used nowadays. When the pulse passes from Herriot-type cells, it acquires small non-linear modulation. Multiple trips through the medium will cause large self-phase modulation (SPM) and a large bandwidth gain.

Figure 2.23 gives a typical MPC schematic representation. We match the eigenmode using a telescope, and then the beam is coupled to the MPC using a small mirror. Then, the pulse passes through the cell multiple times, and the beam is coupled out using the same mirror. Then we collimate the output pulse, and since it is chirped, we remove the chirp utilizing a pair of gratings (or Bragg mirror).

# 3 Method

This chapter provides the STC characterization method, data analysis, and details of the cumbersome calculations that were used during this project. Methods to measure the STCs are summarized in many review papers [2]. These methods can be divided into two categories: measurement of an individual STC and full spatio-temporal measurements. For broader pulses, it is preferable to take a complete spatio-temporal measurement. The main STC characterization methods include: i) spectrally-resolved wavefront measurements, such as Hartmann–Shack assisted, a multidimensional, shaper-based technique for electric-field reconstruction (HAMSTER) [24], ii) Spatially-resolved Fourier transform spectroscopy (FTS), for example, "total E-field reconstruction using a Michelson interferometer temporal scan" (TERMITES) [25] and INSIGHT [26], iii) Hyperspectral imaging techniques for STC, iv) spectral interference methods such a spatio-temporal amplitude-and-phase reconstruction by Fourier-transform of interference spectra of high-complex-beams (STARFISH) [9], v) Holographic methods such as Spatially and Temporally Resolved Intensity and Phase Evaluation Device: Full Information from a Single Hologram (STRIPED-FISH)[27], and lastly, vi) STC measurement based on Young's double slit interferometry such as Iterative Multispectral Phase Analysis for LAsers (IMPALA)[28].

In this project, STC measurement and characterization will be done using spatially resolved Fourier transform spectrometry. This method was developed at Lund University to give a detailed characterization of few-cycle ultrashort pulses and uses both spectral and holographic approaches [7].

## 3.1 Spatially Resolved Fourier Transform Spectrometry

The Spatially Resolved Fourier Transform Spectrometry setup is shown in figure 3.1. The unknown beam is collimated before entering the setup. The beam splitter (BS1) separates the pulse into two parts. The intense part of the beam passes through the delay stage and is focused using the off-axis parabola. This is done to obtain a homogeneous spherical wave. The unknown beam and the reference beam are combined in the second beam splitter (BS2) and are brought to interference on the chip of the CCD camera. We scan the delay between the two pulses by moving the stage (like the Mach-Zehnder interferometer), corresponding to the linear cross-correlation between the two pulses. In addition, in our case, it is spatially resolved. We can retrieve the unknown pulse by recording interferometric data for the different time delays between the pulses.

Let us consider an ultashort pulse in the spectral domain $\tilde{U}(\omega) = |\tilde{U}(\omega)| \exp i\psi(\omega)$, and in time domain $U(t) = |U(t)| \exp i\phi(t)$. Noting the reference pulse as $U_r(t-\tau)$ at

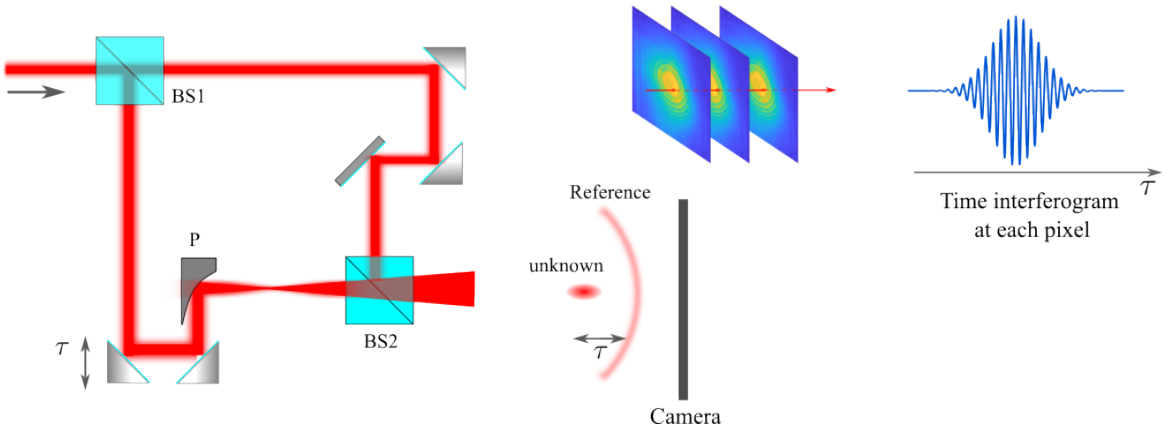


**Figure 3.1:** Schematic illustration of the method.

a given time delay $\tau$, the interferometric complex field will be the sum of the fields: $U_c(t) = U(t) + U_r(t-\tau)$. Then, the intensity of the cross-correlation between the two pulses is:

$$I(\tau) = \int |U(t) + U_r(t-\tau)|^2 dt \tag{3.1}$$

or

$$I(\tau) = \int |U(t)|^2 dt + \int |U_r(t)|^2 dt + \int U^*(t) U_r(t-\tau) dt + \int U(t) U_r^*(t-\tau) dt \tag{3.2}$$

We apply Fourier transform to convert this equation into a frequency domain:

$$\mathcal{F}\{I(t)\} = \mathcal{F}\left\{ \int |U(t)|^2 dt + \int |U_r(t)|^2 dt \right\} + \tilde{U}(\omega)\tilde{U_r}^*(\omega) + \tilde{U_r}^*(-\omega)\tilde{U}(-\omega) \tag{3.3}$$

As we can see, this equation contains three parts: the DC part and two terms around central frequency $\omega_0$ and $-\omega_0$. In the spectral domain, it is easy to separate these terms. Let's look at the second term closely and rewrite it in terms of its amplitude and phase:

$$A_2(\omega) = |\tilde{U}(\omega)||\tilde{U_r}(\omega)| \exp\{i[\psi(\omega) - \psi_r(\omega)]\} \tag{3.4}$$

as we can see from this equation, when we know the reference beam amplitude $|\tilde{U_r}(\omega)|$, phase $\psi_r(\omega)$ and the reference pulse contains enough spectral content, then we can fully characterize the pulse because the term $A_2(\omega)$ is obtained at each pixel of the interferogram. If the reference pulse is homogenous enough to assume its spatial variation is negligible, then we can resolve the pulse amplitude and phase spatially:

$$\tilde{U}(x,y,\omega) = \frac{A_2(x,y,\omega)}{|\tilde{U}_r(\omega)|}\exp\{i\psi_r(\omega)\} \tag{3.5}$$

The reference pulse's homogeneity is achieved by increasing the distance between the beam splitter 2 (BS2) and the camera. Of course, as the radius of the spherical reference pulse increases, its power will decrease. For that reason, the initial pulse is divided by the beam splitter 1 (BS1) by power portion 90/10, and the most intense part is used for the reference beam. We can further increase the homogeneity of the pulse by using the spatial filtering that is discussed in chapter 2, subsection 2.2.1. The focusing mirror with a focal length of 50 mm is used in this setup.

Interferometric image is recorded using the CCD chip FLIR and Allied Vision broadband cameras. The pixel sizes of the cameras are 3.7 $\mu$ m and 5 $\mu$m , respectively. In both cases, the resolution is decreased by a factor 10 in each direction and averages its nearest 8 neighbors to decrease memory usage and increase the signal-to-noise ratio. A delay scan is done by stage piezosystemjena with closed-loop feedback. The scanning range and steps of this stage can be changed. The delay scan must be sub-cycle and very stable.

## 3.2 Data analysis and calculation details

The data obtained from this method is saved as a .h5 extension file. This section gives a detailed analysis example of data obtained from an ultrashort pulse with a 20 fs time duration, a central wavelength around 800 nm, and a 3 kHz repetition rate (ATTOLAB). Similar steps are followed for other measurements.

Saved .h5 file contains three sets of data: spectral intensity of each pixel at a given time delay, $A(x,y,t)$, with dimension $(N_x, N_y, N_t)$, an array of the scan delay times $t$, with dimension (1, $N_t$), and an array of center coordinates of each pixel of the chip CCD camera, $x$, with dimension (1, $N_x$) (figure 3.2 a.). We will use the $x$ array to calibrate the pixel values to real-world dimensions. Since in our case the FLIR CCD camera sensor is square: $N_x = N_y$. In the Matlab code we import these set of the data and assign corresponding variables. For example, in data that was obtained from ATTOLAB were $N_x = N_y = 512$ and $N_t = 1024$.

Then we plot the spectral intensity dependence to time (figure 3.2 b.) to look at a spectral interferogram. If the interferogram contains some unstructured noisy part, we can remove it by applying the time mask using the following equation:

$$t_{mask} = \frac{1}{[1+\exp(t-t_{right})]}\frac{1}{[1+\exp(-(t-t_{left}))]} \tag{3.6}$$

Figure 3.2 c. shows an interferogram of the time-masked data. Here the time range $t_{left} = 100fs$ and $t_{right} = 100fs$ were used. Moreover, the spectrogram intensity is calibrated to its mean intensity.

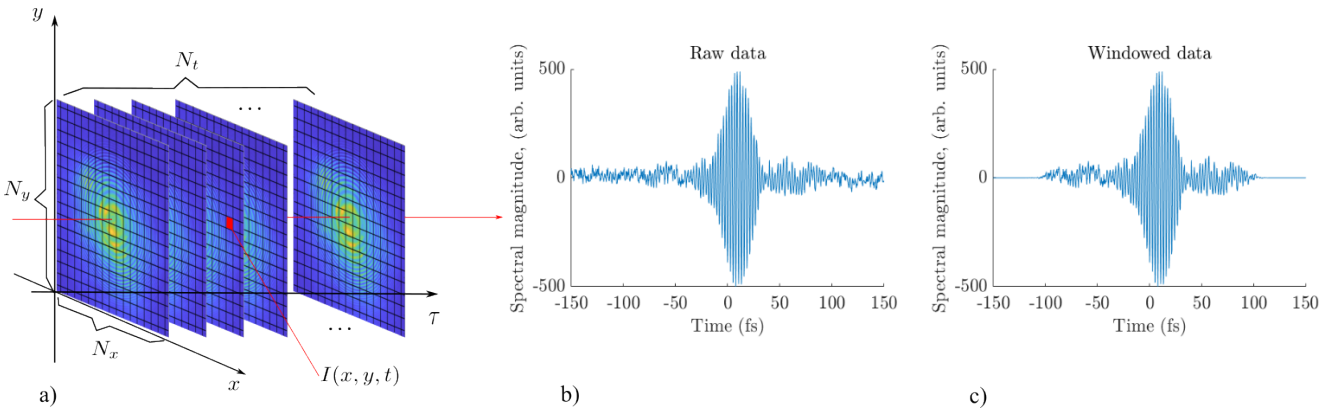


**Figure 3.2:** a) visual illustration of recorded data. b) spectrogram at the central pixel c) windowed data to remove the noise part of the spectrogram

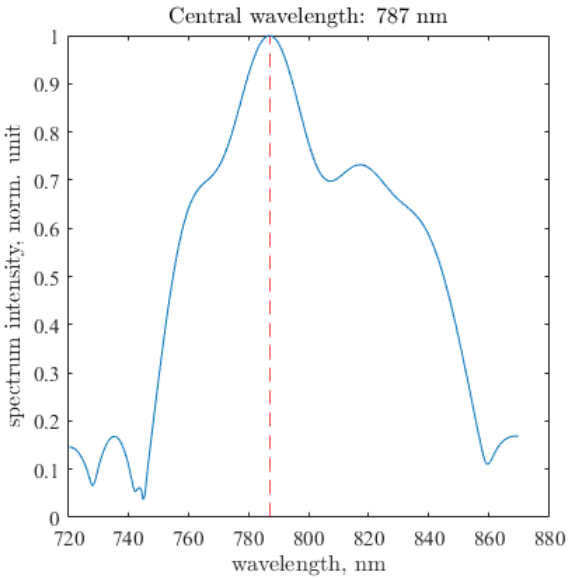


**Figure 3.3:** Retrieved spectrum with filtered wavelength range $[\lambda_{lower}, \lambda_{upper}]$ since only parts with significant spectral amplitude are considered for the analysis

The next step is to convert $I(x, y, t)$ from time to frequency $\tilde{I}(x, y, f)$ domain by taking numerical slice by slice fast Fourier Transform (FFT) for each pixel. From an $x$ and time $t$ array we find array steps: $dx$ and $dt$. $dx$ will be necessary for pixel to real value calibration and $dt$ for taking Fourier transform from time to frequency domain. With the given sampling resolution $N$ sampled frequency values $f$ will be from 0 to $\frac{N-1}{Ndt}$ with $1/dt$ step. It is simple to convert frequency axis values to wavelength by equation $\lambda = c/f$. The retrieved spectrum will contain some noisy data outside of the given wavelength (or frequency) range. Thus, we will select only a given wavelength (or frequency) part of the spectrum $\lambda_{lower}$ and $\lambda_{upper}$ (or $[f_1, f_2]$) and for further calculations, we will only be interested in intensity values $\tilde{I}_{filt}(x, y, f)$ at this frequency range. In figure 3.3 is given the retrieved spectrum at a given wavelength range $[\lambda_{lower}, \lambda_{upper}]$ where $\lambda_{lower} = 720$ nm, $\lambda_{upper} = 870$ nm is given.

The next step is to remove the curvature of the reference pulse from the data. For convenience, we will move the center of the coordinate to the central pixel. We can

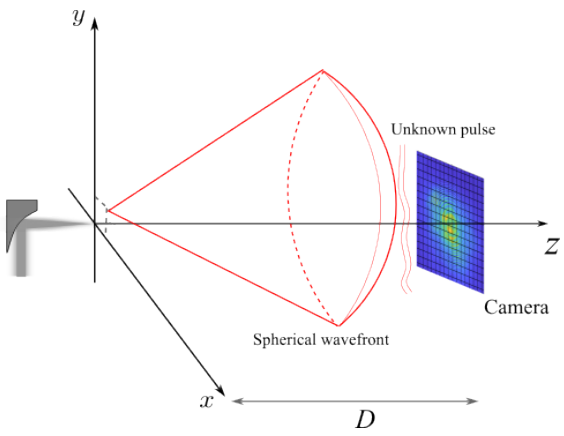


**Figure 3.4:** Illustration of the reference spherical wavefront.

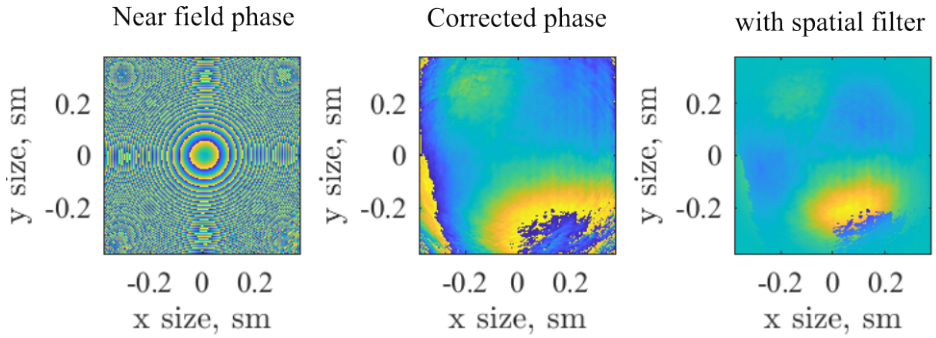


**Figure 3.5:** phases of interferometric image (left), after removing the reference phase (middle), with spatial filter (right) at the peak wavelength ($787nm$)

assume the reference pulse is a spherical wave centered around the focus of the focusing mirror. Due to pulse aberrations, the exact center of the spherical wave will have some offset $x_0$ and $y_0$ relative to the coordinate system centered at the exact focus of the parabolic mirror. If $D$ is the distance between the focus of the parabolic mirror and a camera then the equation for the spherical wave is given by the equation:

$$\tilde{U}_r(x, y, f) = \exp\left\{ik_0(f)\left(\frac{(x - x_0)^2 + (y - y_0)^2}{2D}\right)\right\} \tag{3.7}$$

where $k_0(f) = 2\pi f/c$ wavenumber at a selected frequency range $[f_1, f_2]$,and amplitude is $|\tilde{U}_r(x, y, f)| = 1$. After normalizing the intensity, we can find the unknown pulse by using the equation 3.5 and 3.7.

The parameters $x_0$, $y_0$, and $D$ are difficult to physically measure precisely since the offset values are in the order of micrometers and distance is very sensitive to small changes (see figure 3.4). For that reason, we adjust these parameters by looking at the subtracted wavefront. Figure 3.5 gives the phases of the interferometric image after removing the reference phase and the spatially filtered phase at the peak frequency value. In this case, the fitted parameters were $x_0 = 100$ $\mu$m, $y_0 = -5$ $\mu$m and $D = 3.815 \cdot 10^5$ $\mu$m.

In the next step, we will do spatial filtering to remove the noise of the unknown

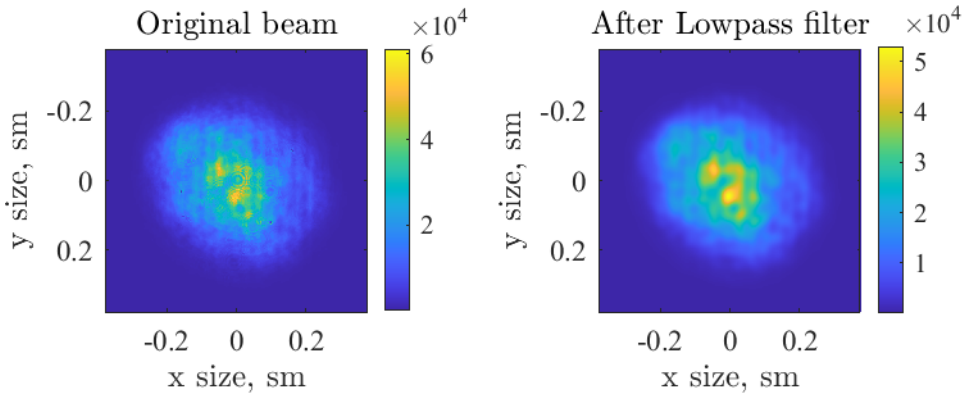


**Figure 3.6:** Beam profile of the unknown beam before (left) and after (right) applying the low pass filter

beam profile. The description of the spatial filtering is given in chapter 2 subsection 2.2.1. After removing the reference phase, we are left only with the complex field of the unknown pulse $\tilde{U}_{un}(x, y, f)$. We will go to $k$-space by applying a 2D Fourier Transform to implement the low pass filtering and then go back to the spatial domain by applying an inverse 2D Fourier Transform. Figure 3.6 gives the beam profile of the unknown pulse before and after the low-pass filter.

### Common aberration correction

Ultrashort pulse $\tilde{U}_{un}(x, y, f)$ may contain several types of aberrations as we discussed in chapter 2 in subsection 2.2.2. In order to characterize the STC of the pulse without any common aberration that is shared by all colors, we will need to do aberration correction. For that, we will find Zernike coefficients of each type of aberration for each wavelength. Next, we will do Zernike decomposition of the wavefront for each wavelength to check at which wavelength range Zernike coefficients fit well with the original wavefront. Then, we will find the average Zernike coefficients and subtract it from the original wavefront:

$$W_{cor}(\lambda) = W_{org}(\lambda) - \sum_{i=0}^{14} a_{i,avg} Z_i \tag{3.8}$$

here $W_{org}(\lambda)$ - original wavefront, $a_{i,avg}$ - average value $i$'s term expansion coefficient.

If the wavefront of the pulse $W_{org}(\lambda)$ is given, we can find Zernike expansion coefficients $a_i(\lambda)$ over a circle by using the equation 2.30 in subsection 2.2.3. Since this equation can find the Zernike coefficients over a circle, we will need to select only the circular part of the wavefront.

After finding the Zernike coefficients, we can decompose the wavefront at a given wavelength using equation $W_{decom}(\lambda) = \sum_{i=0}^{14} a_i(\lambda) Z_i$. We plot the original wavefront $W_{org}(\lambda)$ and the decomposed wavefront $W_{decom}(\lambda)$ at different wavelengths for comparison. Figure 3.7a shows the original wavefront starting from 720.2 nm to 869.81

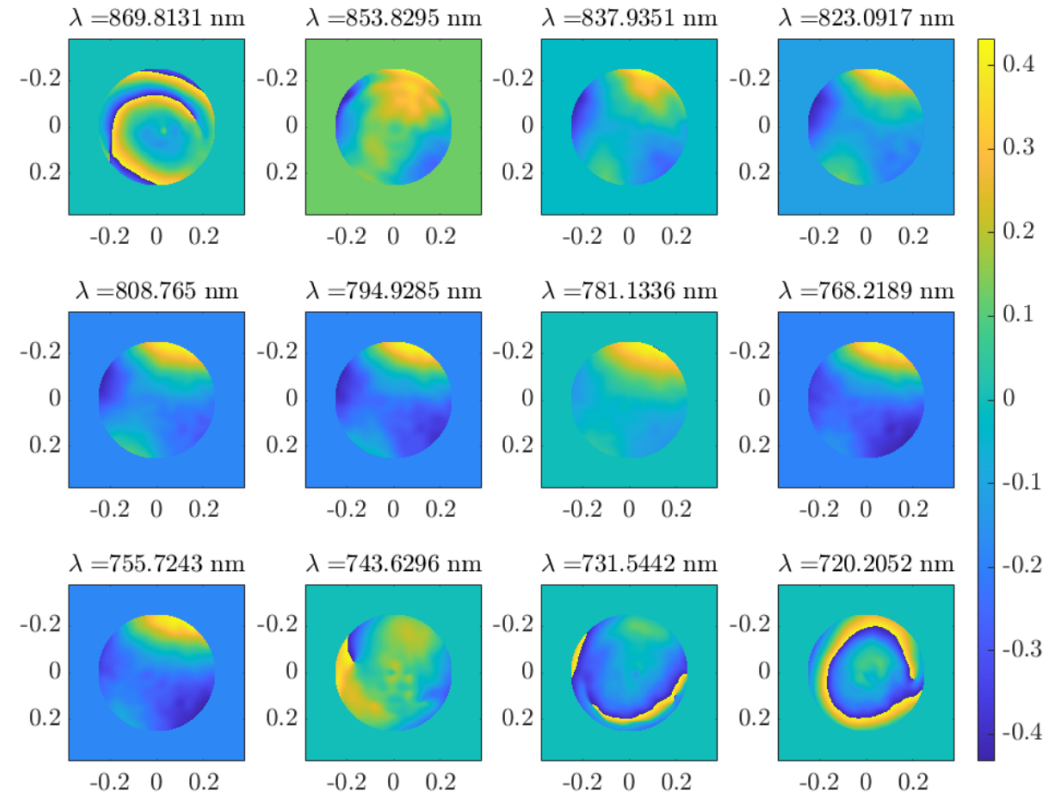


**(a)** Original wavefront $W_{org}(\lambda)$ plotted for 12 different equally spaced wavelength values

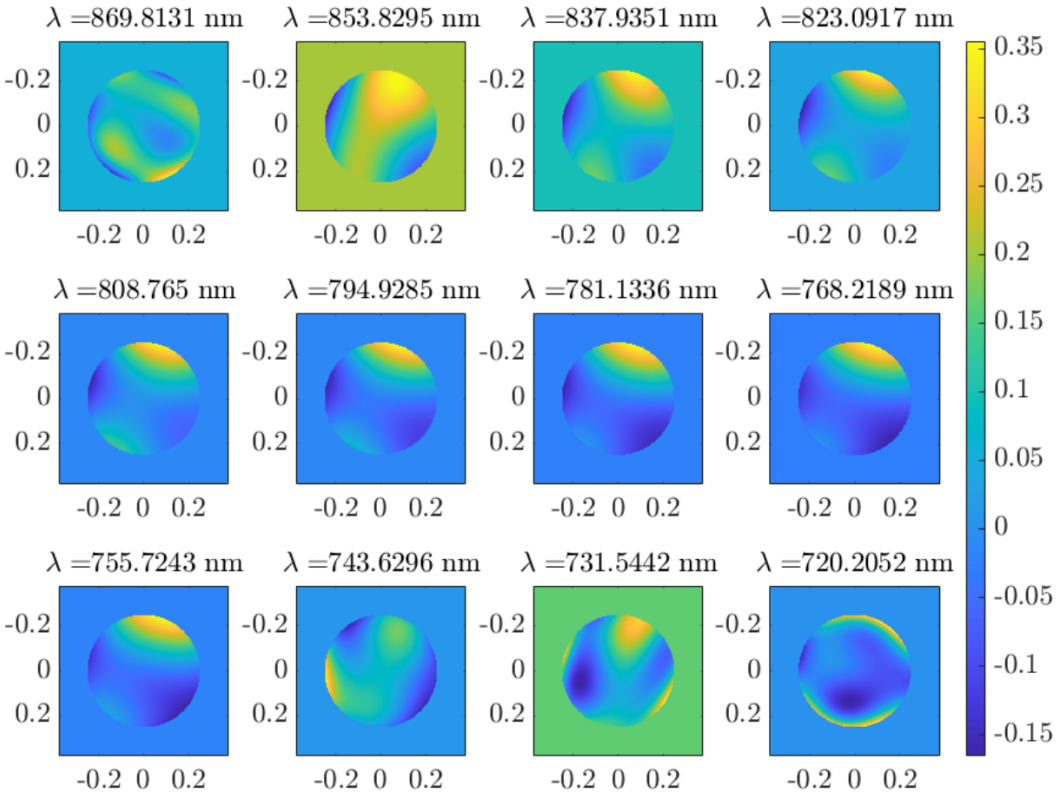


**(b)** Reconstructed wavefront from Zernike decomposition $W_{decom}(\lambda)$ for the same 12 wavelength values

**Figure 3.7:** Comparison of original (a) and reconstructed (b) wavefronts

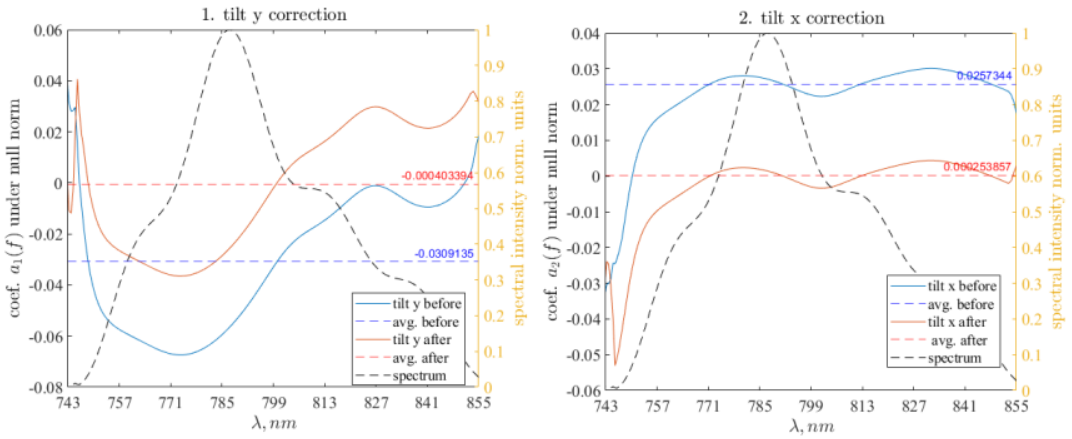


**Figure 3.8:** Common y-tilt and x-tilt correction

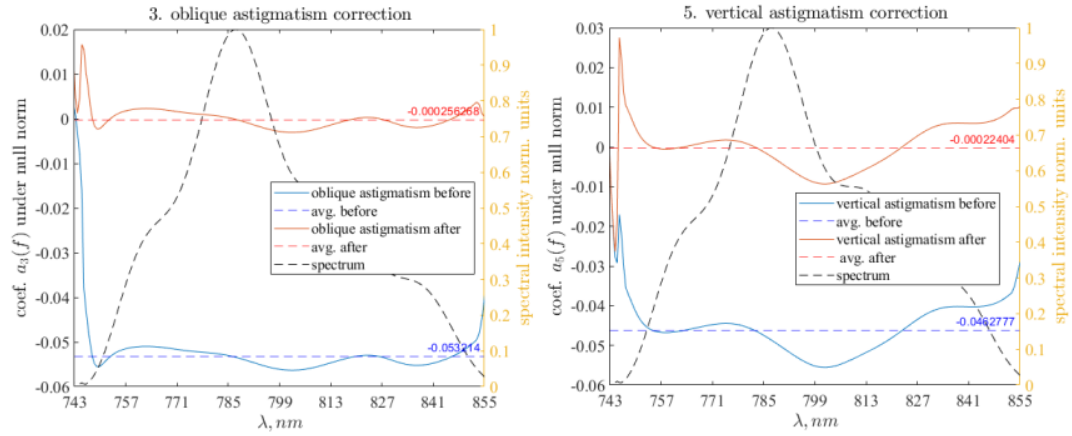


**Figure 3.9:** Common oblique and vertical astigmatism correction. The average $a_{i,avg}$ values of the Zernike coefficients are reduced.

nm and in figure 3.7b reconstructed wavefront from Zernike decomposition for the same wavelength range. Comparing these two figures, we can notice that the Zernike decomposition fails for wavelengths less than 743 nm and greater than 853 nm. For that reason, the average of the Zernike expansion coefficient $a_{i,avg}$ was calculated in wavelength range [743 nm, 853 nm]. Finally, we will do the common aberration correction by using the formula 3.8.

Figures 3.8 and 3.9 illustrate the common aberration correction. After doing the correction, we find the average value Zernike coefficient. The modules of average Zernike coefficients are reduced up to 10 orders of magnitude. For example, in the common y-tilt correction ( left plot of figure 3.8 ), the modulus of the average coefficient is reduced from 0.046 to 0.000403. Similarly, for the vertical astigmatism correction (the right plot of figure 3.9 ), the modulus of the average value vertical astigmatism coefficient is reduced from 0.0426 to 0.000224. We do a similar correction for the other remaining Zernike coefficients. As we have corrected now for the aberration shared by all frequencies, we can now focus on the differences, i.e., the STCs.

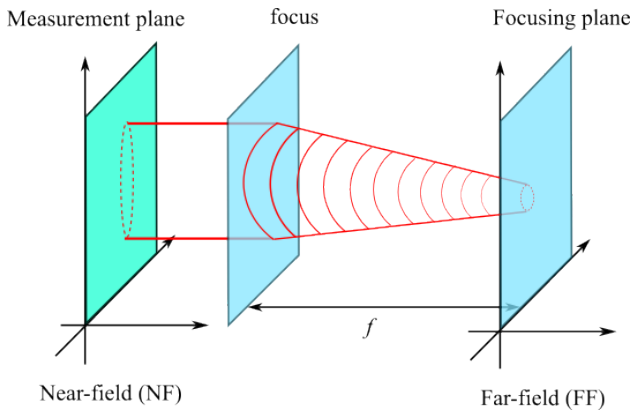


**Figure 3.10:** Illustration of the relevant planes and focusing

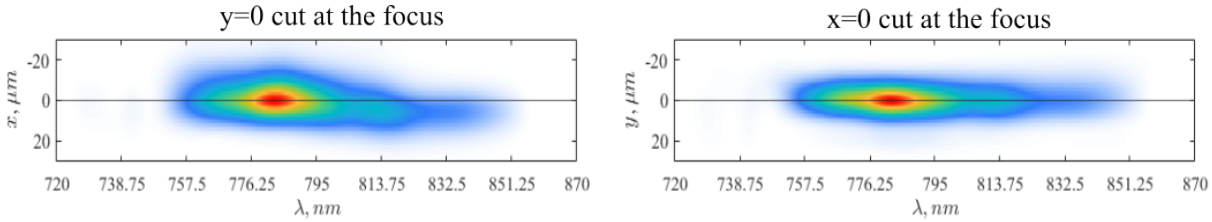


**Figure 3.11:** Verical (left plot) and horizontal (right plot) slices at the focus

### Focusing

Applications of ultrashort laser pulses, such as HHG, often involve focusing. Therefore, the impact of STC on focus is very important to investigate. For that reason, we will focus our beam numerically under aberration-free conditions and will look at transverse focusing of different frequency components. Here, we distinguish two planes illustrated in figure 3.10: the near-field plane - where we do the measurement, and the far-field plane - where we focus the beam.

Focusing, we can implement the formula given in equation 2.24 in the subsection 2.2.1. However, for code convenience, we will follow an analogous procedure. First, we will curve the wavefront with focusing radius $F$ and apply it to a free-space propagation equation given in 2.22 for distance $F$. The choice of the focusing distance $F$ is arbitrary. We used $F = 100$ mm focusing distance. For calculating the Strehl ratio, we do the exact focusing of aberration-free $\tilde{U}_{ideal}$ field. $\tilde{U}_{ideal}$ - is the field of the perfect beam when there are no aberrations exist. It can be found by killing the phase of the complex field of unknown beam, i, e. $\tilde{U}_{ideal} = |\tilde{U}_{un}|$.

Figure 3.11 gives the intensity at $(x, \lambda)$ (i.e. $y = 0$ cut at the focus) and $(y, \lambda)$ representation (i.e. cut $x = 0$ at the focus). These plots give the $x$ and $y$ transverse focus positions of the different frequency components of the ultrashort pulse. In the case of no-significant spatio-temporal coupling, the focusing positions of different frequencies should be the same, i.e., they must be symmetric along the $x$ and $y$ directions. On the right plot of figure 3.11, there are no distinct asymmetries along the $y$ axis. Thus, there is no significant spatiotemporal coupling in that axis. However, on the left plot of figure 3.11, there are distinct asymmetries; thus, we can say that there is noticeable spatio-temporal coupling, i.e., spatial dispersion along $x$ axis or it's not very obvious.

The Matlab code for the data processing is given in appendix A.

# 4 Results and Discussions

This chapter presents the findings and discusses the measurements carried out during the project. It is divided into two sections. The first section is about the STC results of a Titanium-doped Sapphire (Ti: Sapphire) CPA laser system with 800 nm, pulse duration around 20 fs, and 3 kHz repetition rate, which has been an HHG generation source for many years in Lund High-Power Laser Facility (section 4.1). The second section is about STC results of Multi-pass-cell compressed pulses with a wavelength of 1030 nm and pulse duration of less than 20 fs based on German Electron Synchrotron (DESY) that is used for electron acceleration. Ytterbium-doped Yttrium aluminium garnet (Yb: YAG) Innosab laser (Amphos) laser with a pulse duration of 1.2 ps serves as the pulse source of that MPC system.

Since we showed the data processing step in the example of Ti: Sapphire laser characterization in the method chapter, we only show the final results of that measurement, i.e., intensity cuts at the far-field (focus) at different space representations in section 4.1.

To give a better overview of the MPC setup, we included the schematic experimental sketch of MPC setup based on DESY and the beam outputs where the STC measurements are done in subsection 4.2.1. Subsection 4.2.2 gives results of data obtained from Ytterbium-doped Yttrium aluminum garnet (Yb: YAG) Innosab laser (Amphos) output, including all data processing details. However, we include only the final results of the MPC1 outputs at different power levels.

## 4.1 STC characterization of Ti: Sapphire laser

### 4.1.1 Low power results

Figure 4.1 shows STC characterization of the Ti: Sapphire CPA laser with a central wavelength around 800 nm, pulse duration 20 fs, and 3 kHz repetition rate at low power, which is 30% of the maximum peak power. More specifically, figure 4.1a shows the intensity cut at $x = 0$ in $(y, \lambda)$ and $(k_y, \lambda)$ representation. In $(y, \lambda)$, there are no distinct asymmetries along the horizontal axis, which means the spectral components are focused almost to the same $y$ axis coordinate. Similarly, there is no sign of the spatial dispersion in the $(k_y, \lambda)$ representation.

However, for $y = 0$ intensity cut at the focus given in figure 4.1b, noticeable asymmetries in $(x, \lambda)$ representation. Wavelengths around 812.5 nm are focused in lower positions along the $x$ axis than the main wavelength components around 780 nm (middle plot of figure 4.1b). This means that there are spatio-temporal couplings on that axis.

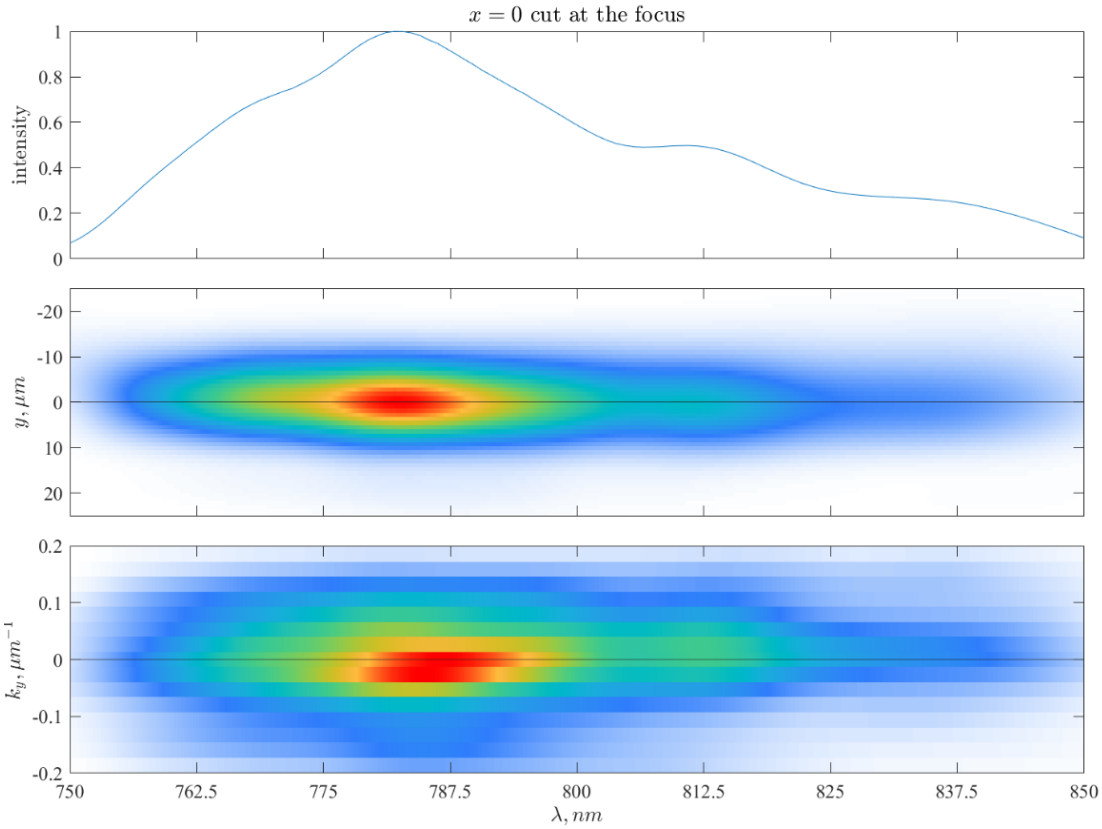


**(a)** Normalized spectrum $|\sum_x \sum_y U(x, y, \lambda)|^2$ (top), intensity cuts ($x = 0$) in $(y, \lambda)$ (middle) and $(k_y, \lambda)$ representation (bottom)

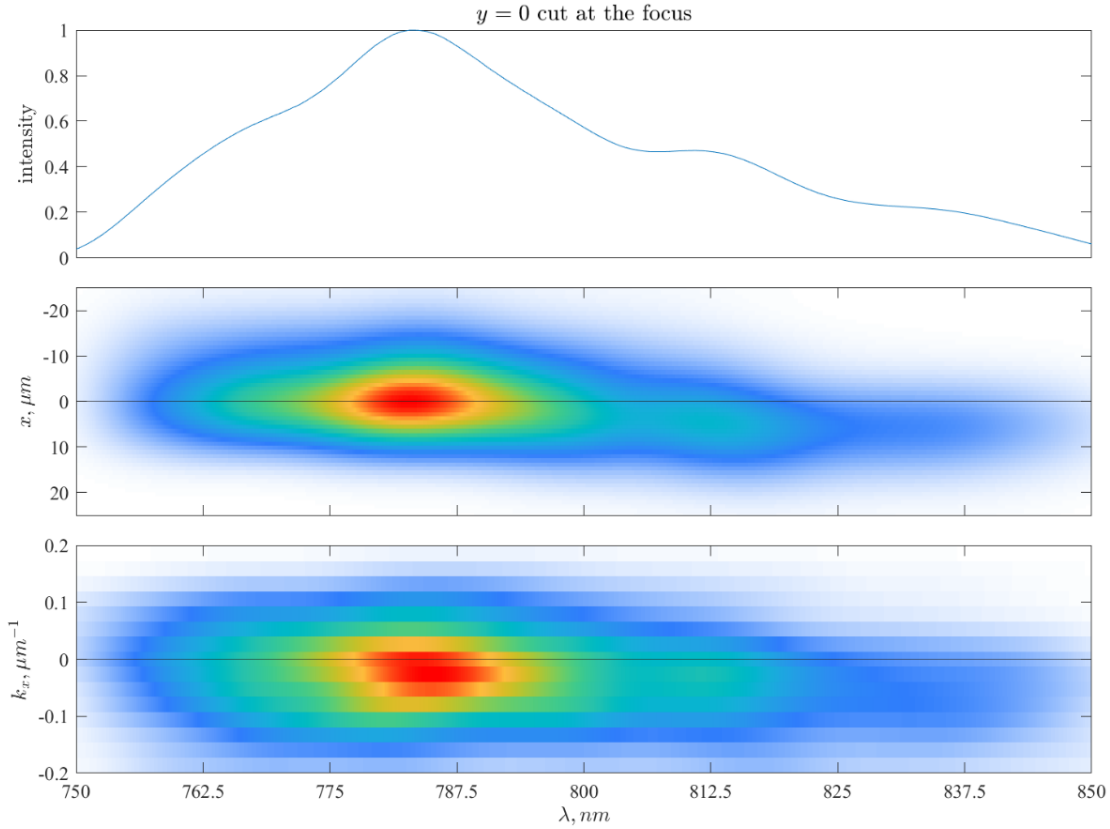


**(b)** Normalized spectrum $|\sum_x \sum_y U(x, y, \lambda)|^2$ (top), intensity cuts ($y = 0$) in $(x, \lambda)$ (middle) and $(k_x, \lambda)$ representation (bottom)

**Figure 4.1:** Spatio-temporal characterization of the pulse 800nm wavelength, pulse duration around 20 fs at low power

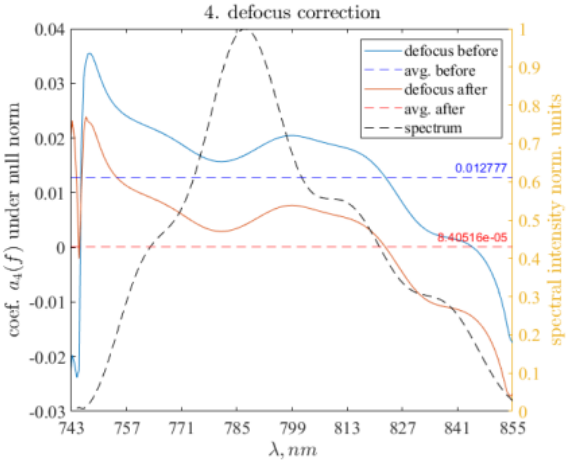


**Figure 4.2:** Defocus coefficient $a_4(\lambda)$ for 30% of the maximum peak power of Ti:Sapphire laser (AttoLab) before and after the correction

One of the Zernike expansion coefficients that were mentioned in subsection 2.2.3, called defocus coefficient $a_4$, gives information about how wavefront is curved in the NF. The defocus graph shown in figure 4.2 shows that this coefficient greatly varies with the wavelength. This is a sign of pulse front curvature. As we discussed before, PFC leads to longitudinal chromatism; in other words, the defocus coefficient variation infers that different wavelengths are focused at different longitudinal positions.

### 4.1.2 High power results

We were interested in knowing if the STCs change at high power. Figure 4.3 gives STC characterization at the 100% of the maximum peak power. There are no distinct asymmetries at the intensity cut $x = 0$ at the spectrum (figure 4.3 b.). However, slight asymmetries are observable in the $y = 0$ intensity cut at the $(x, \lambda)$ representation (figure 4.3 a.).

Figure 4.4 shows the defocus coefficient and a common defocus correction at high power. Defocus coefficient variation gets stabilized for most of the frequency values, but we still observe slight oscillations around an average value.

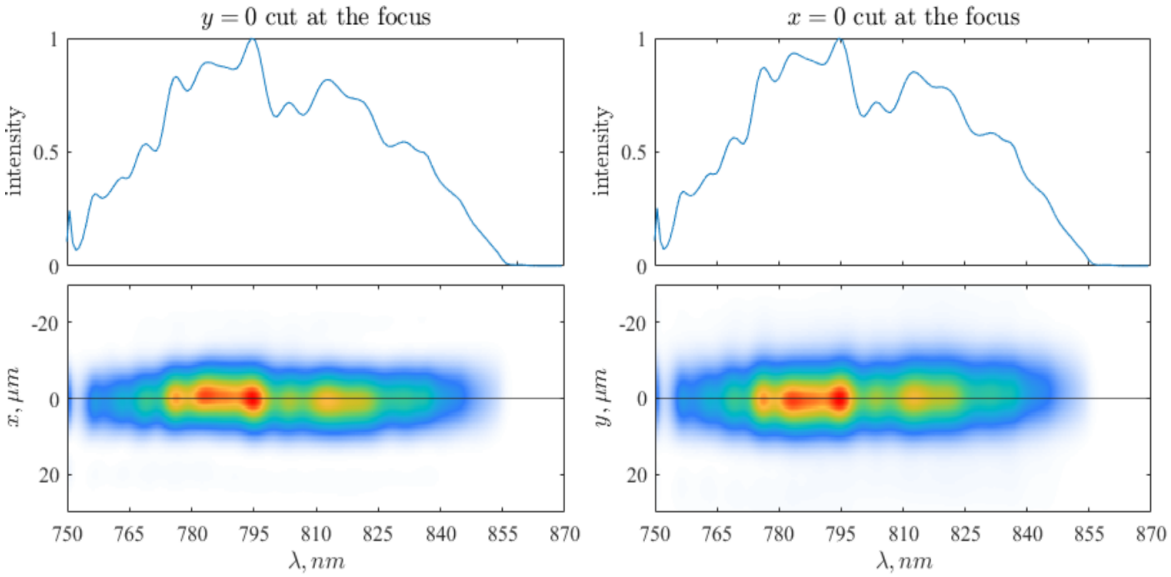


**Figure 4.3:** Spatio-temporal characterization of the pulse 800 nm wavelength, pulse duration around 20 fs at high power (AttoLab)

## 4.2 Multi-pass-cell compressed (MPC) pulses

### 4.2.1 Experimental setup for MPC system

A sketch of the multi-pass cell compression system based on DESY is given in figure 4.5. The goal was to determine whether there is STC in this MPC setup. Several STC measurements were done at different outputs of this setup to achieve this goal. These outputs are indicated with numbers in figure 4.5. The laser source for this system comes from a Ytterbium-doped Yttrium aluminium garnet (Yb: YAG) Innosab laser (Amphos) with energy 9.8 mJ, 1-20 kHz repetition rate, and pulse duration around 1.2 ps with a central wavelength of 1030 nm. This pulse is sent to the first MPC1 via a mode-matching telescope (MMT). Then, this pulse takes 10 round trips inside MPC1. The initial pulse duration is roughly maintained at 1 ps during the propagation inside the MPC1, while the Fourier transform limit (FTL) is decreased to 49 fs after the MPC1. Then, the pulse is coupled out from MPC1 and, through a telescope (TEL), sent to the compressor, which gives a compressed pulse with a duration very close to the Fourier limit. After that, this pulse is coupled to the second MPC2 using another MMT, where the Fourier transform limit duration decreases further to 9.2 fs after taking 10 round trips. Then, this pulse is coupled out and, after passing the telescope (TEL), sent to another compressor (CMP).

### 4.2.2 STC characterization of the Yb: YAG Innosab laser (AMPHOS)

We first start with characterizing the Yb: YAG Innosab laser (Amphos) pulse with a duration of 1.2 ps. It corresponds to the output (1) of the MPC system given in figure 4.5.

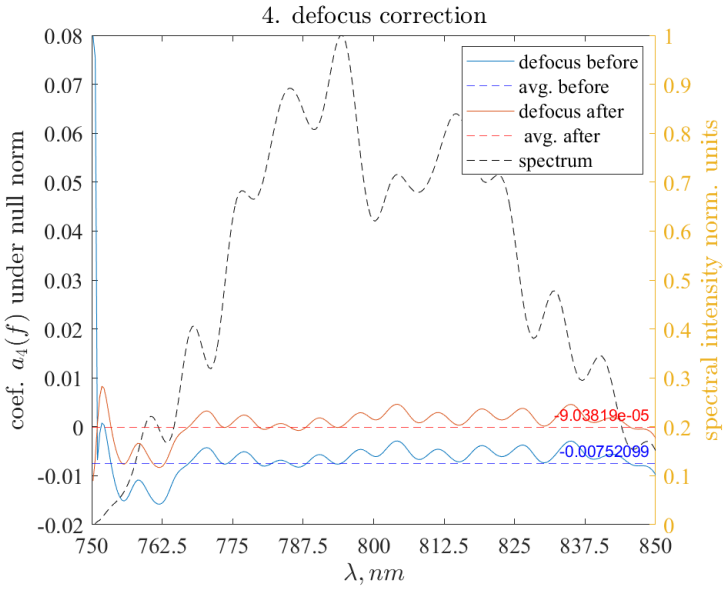


**Figure 4.4:** Defocus coefficient and its correction for high-power Ti: Sapphire (AttoLab) output

Figure 4.6 gives the reconstructed spectra of the central pixel of obtained data and the measured spectra of the output, measured with another spectrometer. The reconstructed spectral peak corresponds to the 1029 nm wavelength, while the measured peak is at the 1031.9 nm wavelength. It means our setup reconstructed the spectra with an error of 0.28%, which gives good credit to the capability of the STC setup. Figure 4.7 shows an illustration of the removal of the curvature of the reference beam. For this data, the spherical reference beam with a diameter of $D = 46.9$ sm and offset values $x_0 = -160\mu$m, and $y_0 = -90\mu$m was subtracted.

Before making the common aberration corrections, we compared the original wavefront at different wavelength values from 1024.11 nm to 1036.95 nm. Zernike coefficients fit well except for some noises on the original wavefront, as shown in figure 4.8. Then, we find the average Zernike coefficients for all the wavelengths and remove the common aberrations shared by all colors using the formula 3.8.

Figure 4.9 illustrates the common correction of the defocus, tilt y, vertical astigmatism, and oblique astigmatism correction. We can observe that the module of the average Zernike coefficients $a_{i,avg}(\lambda)$ are greatly reduced. For example, the modulus of the average vertical astigmatism value is reduced from 0.054 to 0.00017, and similarly, for oblique astigmatism, that value is reduced from 0.0079 down to 0.000293 (see figures 4.9b).

We numerically focus the beam in order to see its characteristics in the far-field. Figure 4.10 gives the beam profile at the focus. A Strehl ratio of 0.7216 was obtained for this beam. Since we removed all of the common aberrations up to the $14^{th}$ term, we can conclude that this reduction from the ideal (no STC) beam intensity is reduced by possible STC couplings or other higher-order aberrations (greater than $14^{th}$ term).

Figure 4.11 gives the STC characterization at output (1) of the setup (see figure 4.5). The intensity cut at $y = 0$ shows no distinct asymmetries in the $(x, \lambda)$ representation

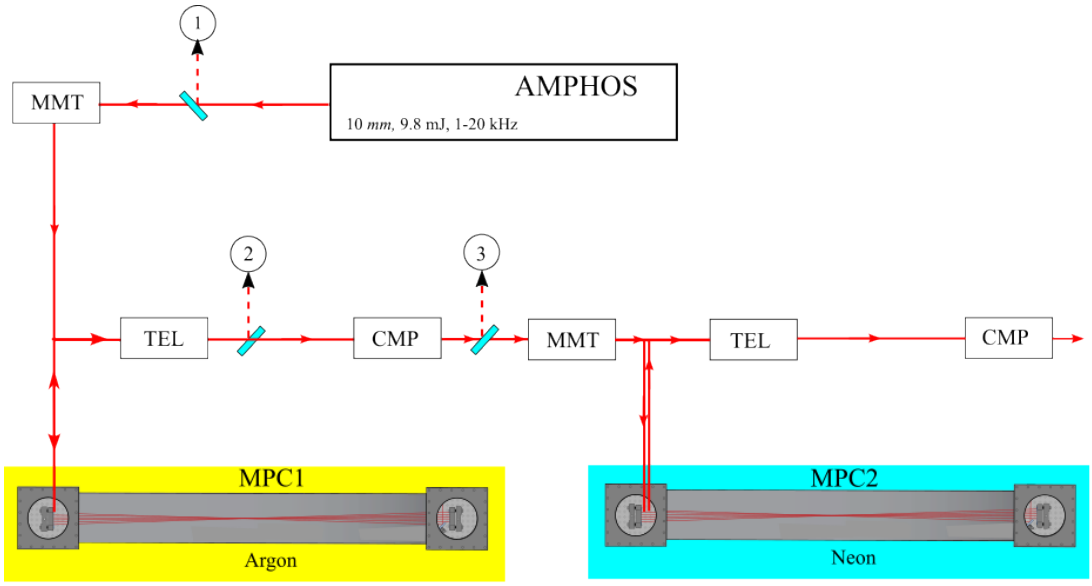


**Figure 4.5:** Experimental setup used for the multi-pass-cell post-pulse compression by using two gas-filled MPCs and outputs where the STC measurements are implemented: (1) output of the AMPHOS laser, (2) MPC1 output, (3) MPC1 output after the compressor, TEL - telescope, and CMP-compressor. The sketch is inspired by paper [29]

.

(left middle plot of figure 4.11). However, there are slight asymmetries in the $x = 0$ intensity cut at $(y, \lambda)$ representation (right middle plot of figure 4.11). We can conclude that there are STCs on that axis, which might be caused by a slight misalignment of the internal grating compressor inside of the AMPHOS.

### 4.2.3 MPC1 output

STC measurements were done at the output of MPC1 before the compressor ( output (2) in figure 4.5).

Figure 4.12 shows the comparison of the reconstructed spectra and measured spectra that were obtained from normal spectrometer. From that graph, we can see that the spectral ranges are similar. However, since our reconstructed spectrum's resolution is low, it fails to reconstruct the exact same spectra. Despite that, it gives us reliably enough spectral shape that is similar to the measured one. Like any Fourier transform approach, the spectral resolution depends on the scan range.

STC characterization of MPC1 output before the compressor at different power levels is given in figures 4.13 and 4.14. These figures show in the $y = 0$ intensity cut, no distinct asymmetries in $(x, \lambda)$ representations (left plots in fig. 4.13). However, there are noticeable asymmetries in the intensity cut at $x = 0$ in $(y, \lambda)$ representation at 20% (fig. 4.13 a.), 40% (fig. 4.13 b.), and 60% (fig. 4.13 c.) power levels. This means that there is STC in that axis. This STC originates from the AMPHOS laser pulse because,

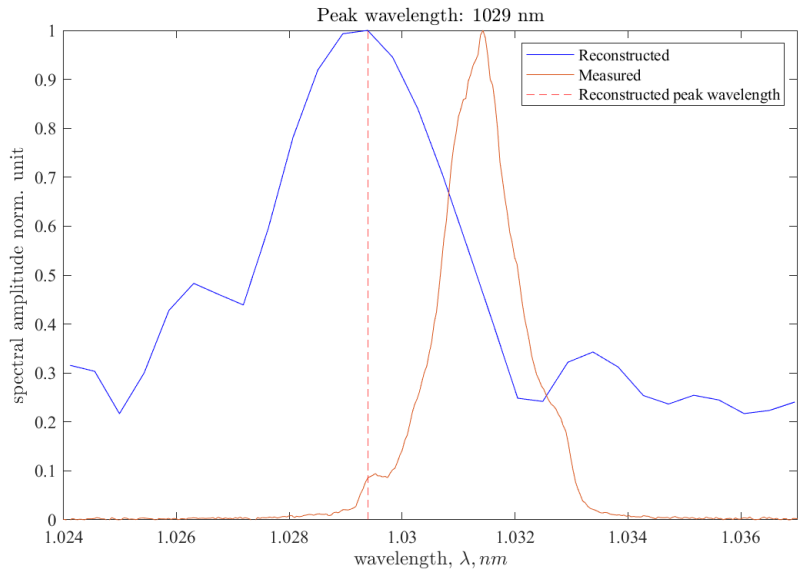


**Figure 4.6:** Comparison of measured and reconstructed spectra of the AMPHOS laser

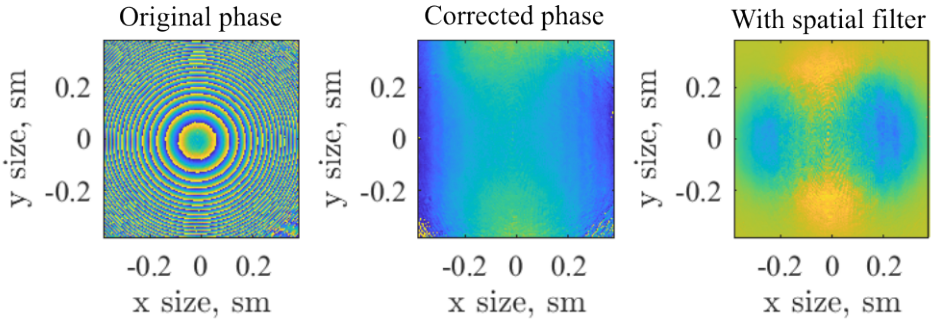


**Figure 4.7:** Phase correction corresponding to the peak wavelength

as we saw in its STC characterization, it has STC on the same axis. MPCs usually do not introduce much STC because there are no dispersive elements such as gratings or prisms. At higher power levels 80% and 100% there is no distinct asymmetries both intensity cuts at $x = 0$ and $y = 0$, in the $(x, \lambda)$, $(y, \lambda)$ representations as we can see form figure 4.14.

The most interesting result was obtained for STC pulse characterization after the compressor at full power given in figure 4.15. This result corresponds to the output (3) of the MPC setup in figure 4.5. We can see distortion on the $y = 0$ intensity cut in $(x, \lambda)$ representation, corresponding to the tilt. This massive tilt is most likely related to misalignments of the grating compressor following the MPC. Furthermore, the effect is stronger in one direction, which makes sense because the alignment of the grating compressor is most sensitive in the direction of diffraction of the gratings.

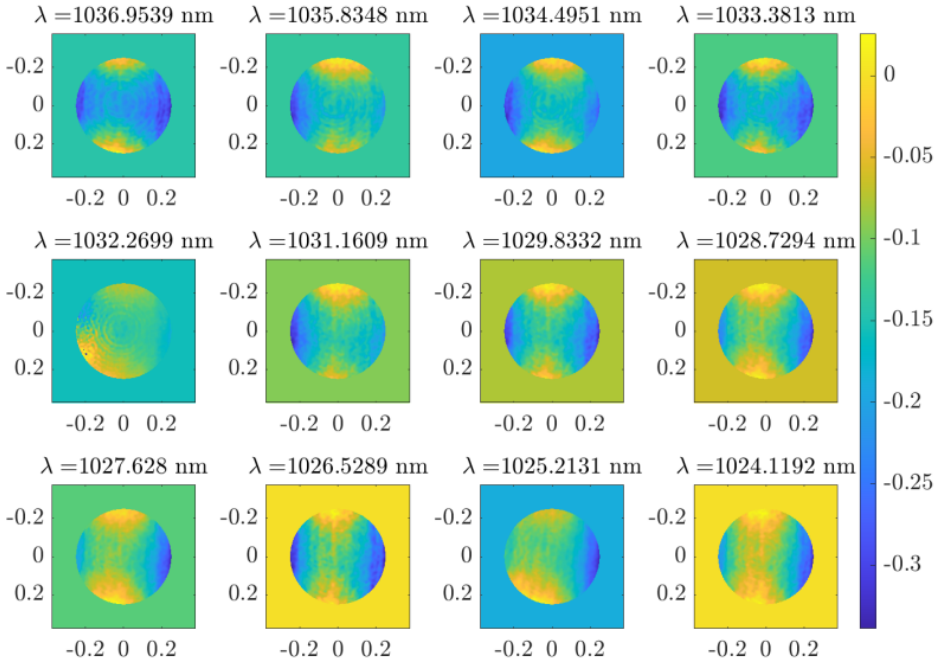


**(a)** Original wavefronts for different wavelength

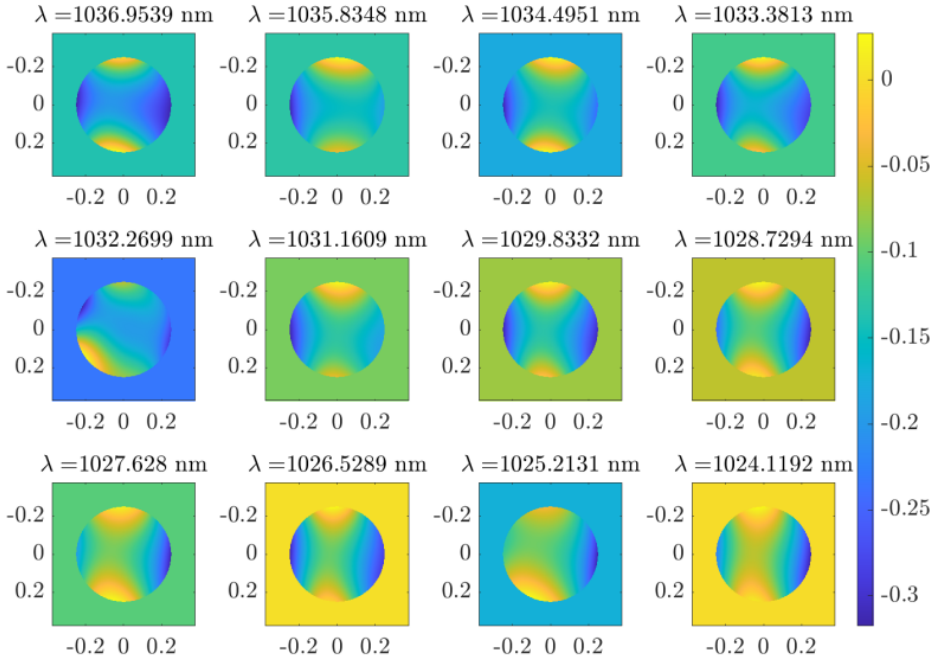


**(b)** Corresponding Zernike decomposed wavefronts

**Figure 4.8:** Original (a) and Zernike decomposed (b) wavefronts for the different wavelength values

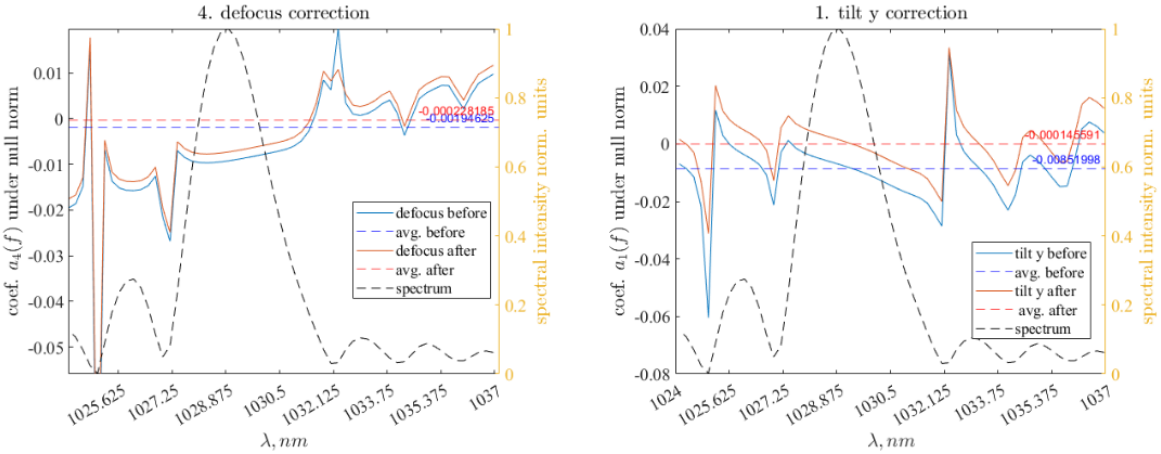


**(a)** Common defocus (left plot) and common tilt-y (right plot) corrections

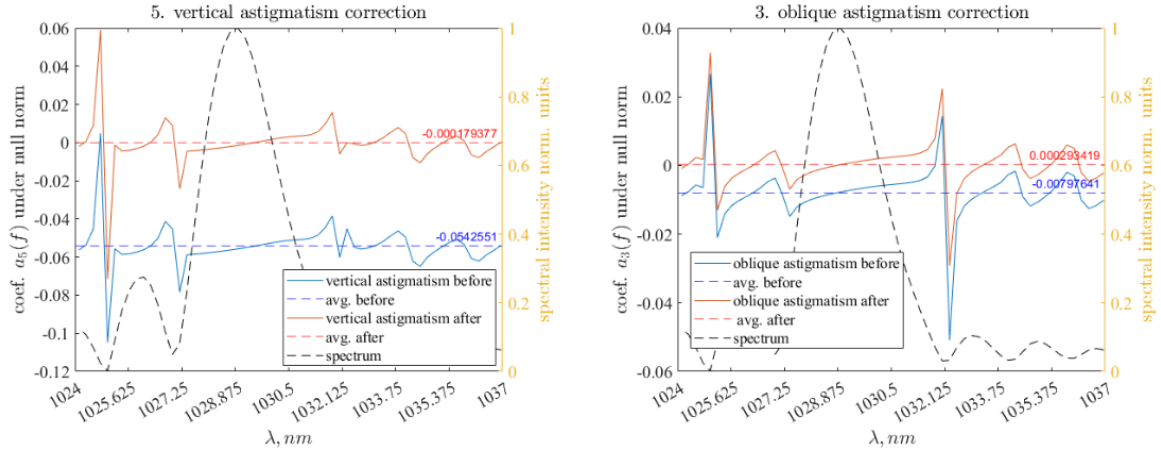


**(b)** Common vertical astigmatism (left plot) and common oblique astigmatism (right plot) corrections

**Figure 4.9:** Common aberration corrections for AMPHOS laser output

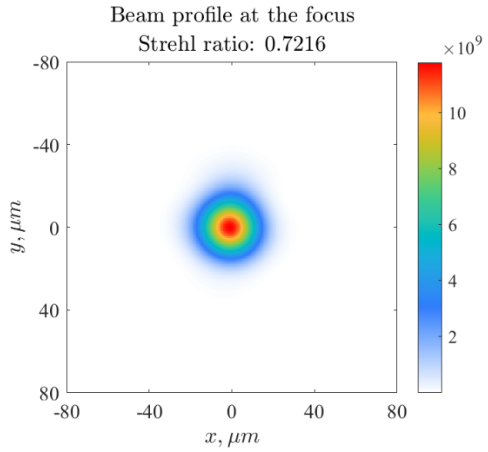


**Figure 4.10:** Beam profile at the focus

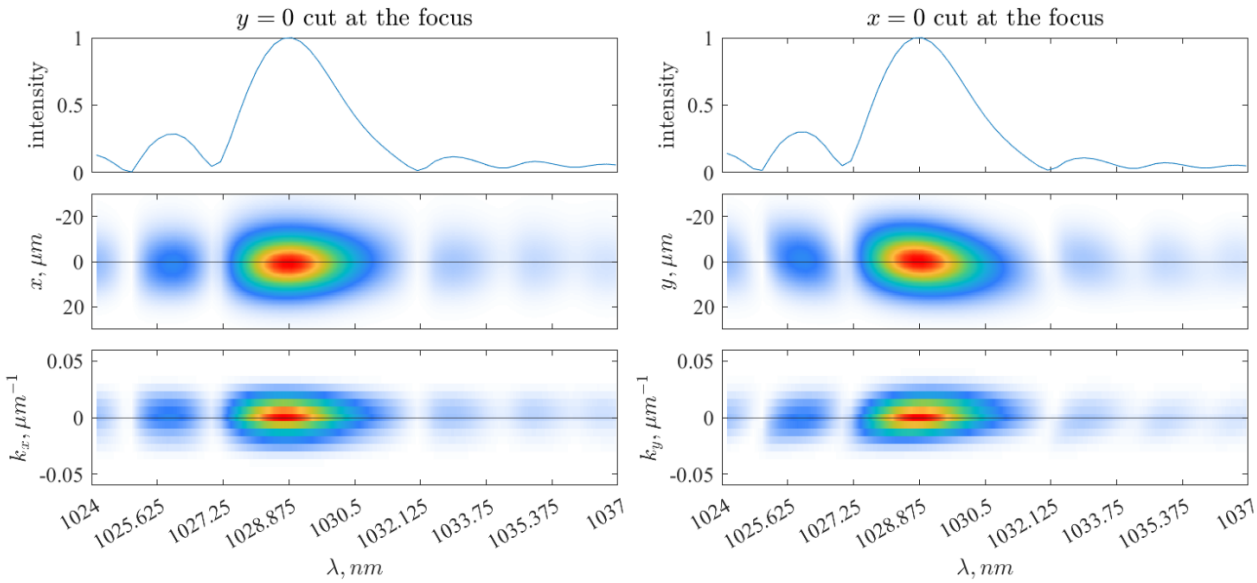


**Figure 4.11:** STC characterization of the AMPHOS laser source at full power. Slight asymmetries on the $x = 0$ intensity cut (right plot) in the $(y, \lambda)$ representation is a sign of the STC in that axis.

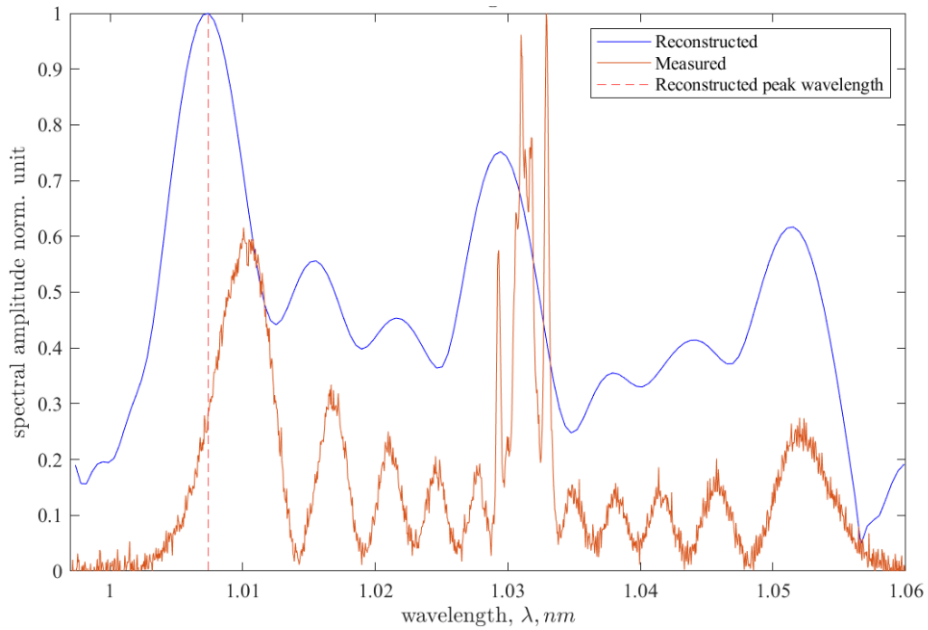


**Figure 4.12:** Reconstructed and measured spectra of the MPC1 output before the compressor

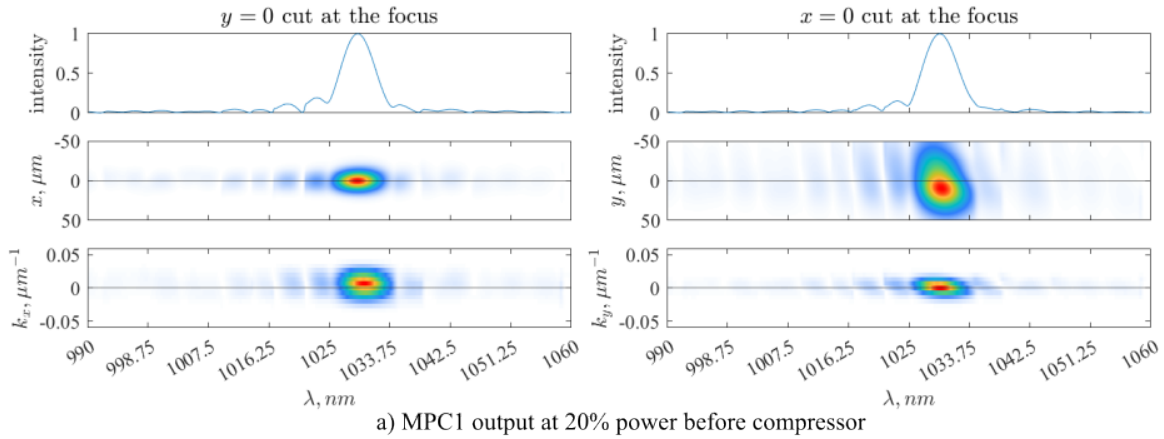


a) MPC1 output at 20% power before compressor

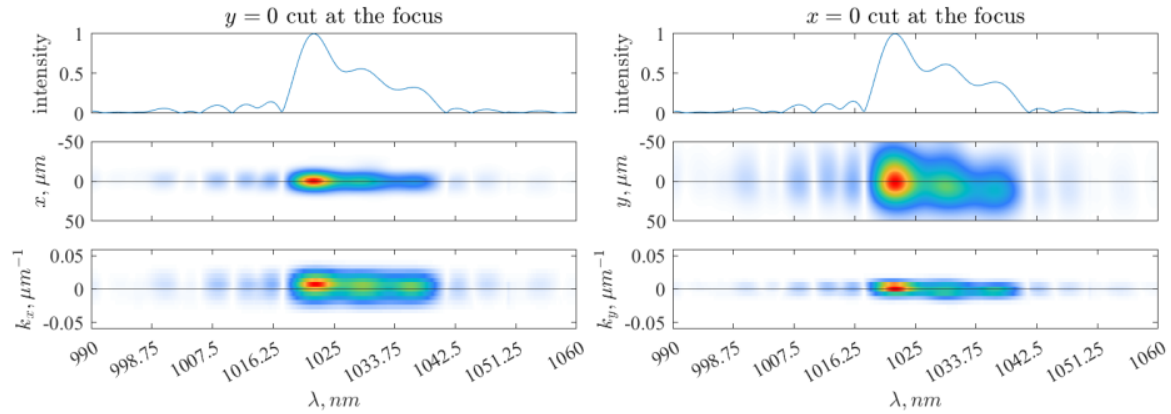


b) MPC1 output at 40% power before compressor

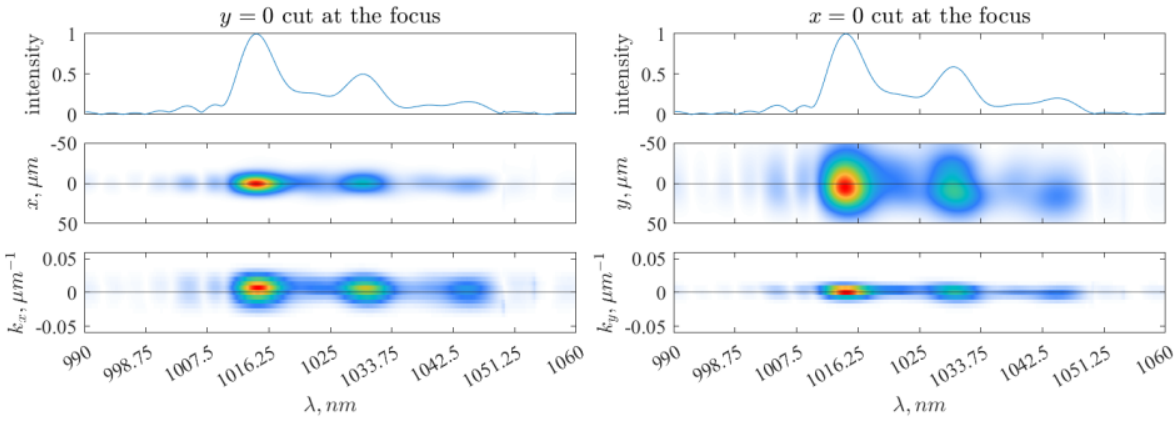


c) MPC1 output at 60% power before compressor

**Figure 4.13:** MPC1 outputs before the compressor at different input power levels.

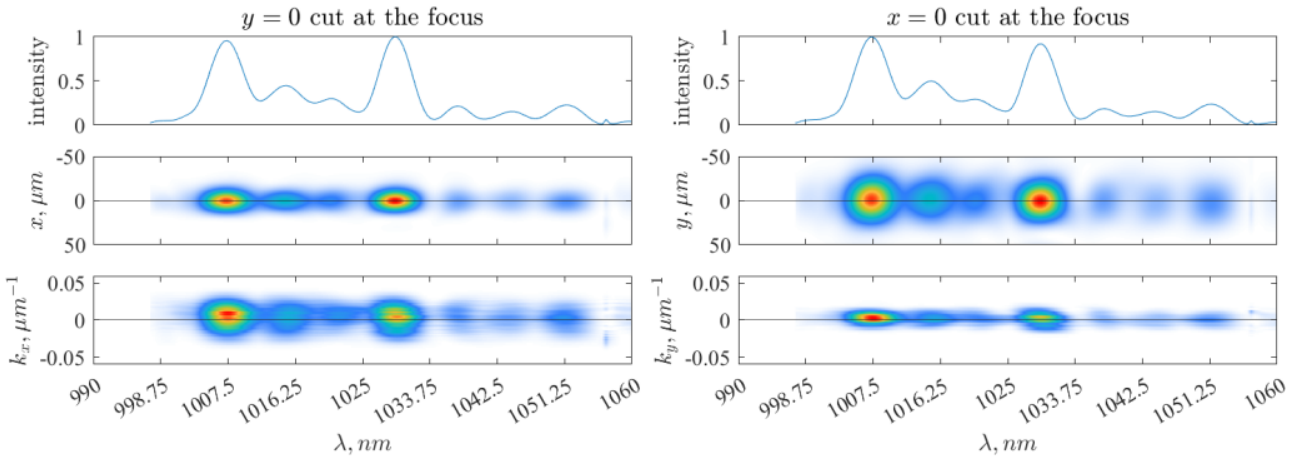


a) MPC1 output at 80% power before the compressor

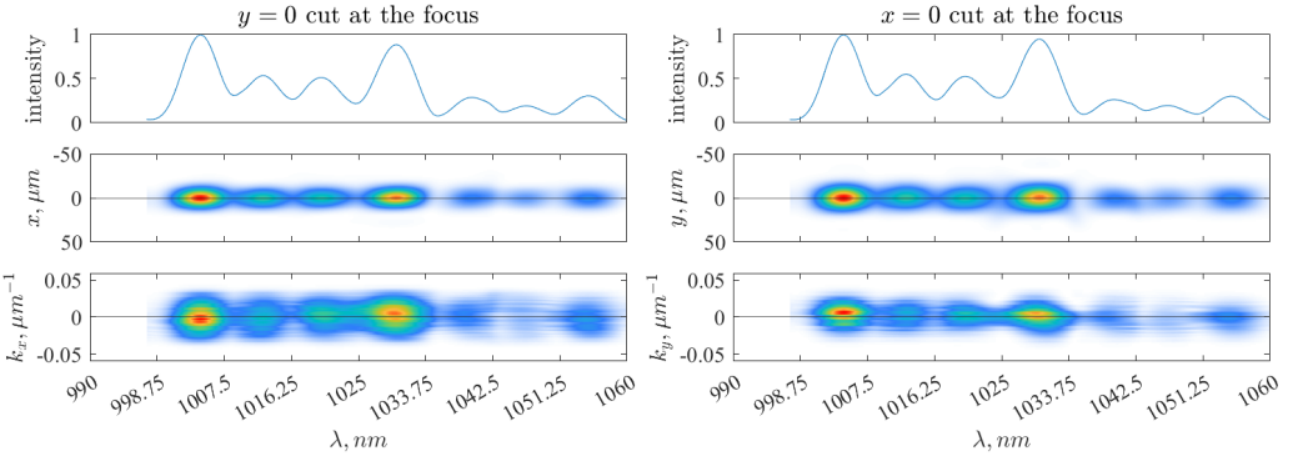


b) MPC1 output at 100% power before the compressor

**Figure 4.14:** MPC1 output before the compressor at (a) 80% and (b) 100 % powers before the compressor

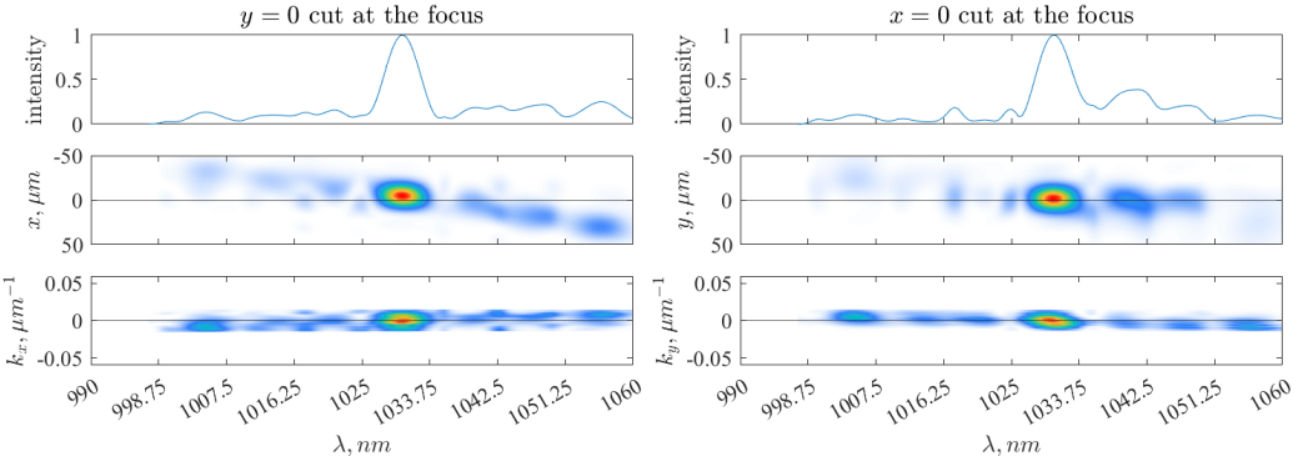


**Figure 4.15:** MPC1 output after the compressor at 100 % power

# 5 Conclusion and Outlook

In this project, the spatio-temporal characterization of two intense laser systems was presented. The first was an 800 nm central wavelength Ti: Sapphire CPA laser with a repetition rate of 3 kHz and a pulse duration of 20 fs. The second was a 1030 nm central wavelength MPC system with a repetition rate of 20 kHz. The results showed that for the Ti: Sapphire CPA laser, there is a spatial chirp at the focus along the $y$ transverse axis for both low and high-power cases. In the high-power cases, this spatial chirp becomes weaker but still observable. Moreover, the great changes in the defocus coefficient with frequencies (or wavelengths) at low power have indicated the existence of pulse front curvature.

STC characterization was done at each stage of the MPC system. Its results showed spatial dispersion in the $y$ transverse direction of the focus in the Yb: YAG Innosab laser output. This was also the main cause of the observed STCs in MPC1 output at low powers. However, at high powers $(80\%, 100\%)$ the STCs becomes unobservable at the MPC1 output. This is an important finding, indicating that the STCs of the incoming laser are not translated to the spectrally broadened components in an MPC! Lastly, the STC measurements are done at the MPC1 output after the compressor. Significant spatial chirp is observed due to the misalignment of the compressor. A strict realignment of the compressor would remove most of the observed STCs.

The data analysis code underwent improvements in this project. We introduced a shared aberration removal script, which simplifies the analysis process. By removing common aberrations, real STCs are more easily identified, enhancing the accuracy and reliability of the analysis. This thesis provides comprehensive details on the data analysis and documentation of the MATLAB code, a valuable resource for future research in this field.

Looking ahead, the future of the measurement setup holds promising possibilities. Notably, the spectral resolution of the measurement can be improved by increasing the scanning range and the number of points recorded. This is particularly relevant for complex spectra like the MPC's output, which necessitates a high resolution for better reconstructed spectra. Also, like any non-single-shot measurement method, the stability of the beam pointing is important for obtaining better data.

The most time-consuming part of the experiment is recording interferometric data. This time depends on the number of points in the given scanning range. In our case, it took 20-40 minutes, depending on the number of points. The interferometric image recording software is written in Matlab, which keeps the data in its buffer. Handling large data structures is challenging, and proper memory management has to be implemented to make faster data acquisition and to prevent buffer overflow.

# Bibliography


[1] Spencer W Jolly, Olivier Gobert and Fabien Quéré. "Spatio-temporal characterization of ultrashort laser beams: a tutorial". In: *Journal of Optics* 22.10 (2020), p. 103501. DOI: 10.1088/2040-8986/abad08. URL: https://dx.doi.org/10.1088/2040-8986/abad08.

[2] Donna Strickland and Gerard Mourou. "Compression of amplified chirped optical pulses". In: *Optics Communications* 56.3 (1985), pp. 219–221. ISSN: 0030-4018. DOI: https://doi.org/10.1016/0030-4018(85)90120-8. URL: https://www.sciencedirect.com/science/article/pii/0030401885901208.

[3] Zenghu Chang. "Fundamentals of Attosecond Optics". In: 2011. URL: https://api.semanticscholar.org/CorpusID:118294962.

[4] Rick Trebino and Daniel J. Kane. "Using phase retrieval to measure the intensity and phase of ultrashort pulses: frequency-resolved optical gating". In: *J. Opt. Soc. Am. A* 10.5 (1993), pp. 1101–1111. DOI: 10.1364/JOSAA.10.001101. URL: https://opg.optica.org/josaa/abstract.cfm?URI=josaa-10-5-1101.

[5] K. W. DeLong, Rick Trebino, J. Hunter and W. E. White. "Frequency-resolved optical gating with the use of second-harmonic generation". In: *J. Opt. Soc. Am. B* 11.11 (1994), pp. 2206–2215. DOI: 10.1364/JOSAB.11.002206. URL: https://opg.optica.org/josab/abstract.cfm?URI=josab-11-11-2206.

[6] L. Gallmann, D. H. Sutter, N. Matuschek, G. Steinmeyer, U. Keller, C. Iaconis and I. A. Walmsley. "Characterization of sub-6-fs optical pulses with spectral phase interferometry for direct electric-field reconstruction". In: *Opt. Lett.* 24.18 (1999), pp. 1314–1316. DOI: 10.1364/OL.24.001314. URL: https://opg.optica.org/ol/abstract.cfm?URI=ol-24-18-1314.

[7] Miguel Miranda, Thomas Fordell, Cord Arnold, Anne L'Huillier and Helder Crespo. "Simultaneous compression and characterization of ultrashort laser pulses using chirped mirrors and glass wedges". In: *Opt. Express* 20.1 (2012), pp. 688–697. DOI: 10.1364/OE.20.000688. URL: https://opg.optica.org/oe/abstract.cfm?URI=oe-20-1-688.

[8] D. Meshulach, D. Yelin and Y. Silberberg. "Real-time spatial–spectral interference measurements of ultrashort optical pulses". In: *J. Opt. Soc. Am. B* 14.8 (1997), pp. 2095–2098. DOI: 10.1364/JOSAB.14.002095. URL: https://opg.optica.org/josab/abstract.cfm?URI=josab-14-8-2095.

[9] Benjamín Alonso, Íñigo J Sola, Óscar Varela, Juan Hernández-Toro, Cruz Méndez, Julio San Román, Amelle Zaïr and Luis Roso. "Spatiotemporal amplitude-and-phase reconstruction by Fourier-transform of interference spectra of high-complex-beams". In: *JOSA B* 27.5 (2010), pp. 933–940.

[10] Miguel Miranda, Marija Kotur, Piotr Rudawski, Chen Guo, Anne Harth, Anne L'Huillier and Cord L. Arnold. "Spatiotemporal characterization of ultrashort laser pulses using spatially resolved Fourier transform spectrometry". In: *Opt. Lett.* 39.17 (2014), pp. 5142–5145. DOI: 10.1364/OL.39.005142. URL: https://opg.optica.org/ol/abstract.cfm?URI=ol-39-17-5142.

[11] Anne-Lise Viotti, Marcus Seidel, Esmerando Escoto, Supriya Rajhans, Wim P. Leemans, Ingmar Hartl and Christoph M. Heyl. "Multi-pass cells for post-compression of ultrashort laser pulses". In: *Optica* 9.2 (2022), pp. 197–216. DOI: 10.1364/OPTICA.449225. URL: https://opg.optica.org/optica/abstract.cfm?URI=optica-9-2-197.

[12] Z. Bor. "Distortion of Femtosecond Laser Pulses in Lenses and Lens Systems". In: *Journal of Modern Optics* 35.12 (1988), pp. 1907–1918. DOI: 10.1080/713822325. eprint: https://doi.org/10.1080/713822325. URL: https://doi.org/10.1080/713822325.

[13] J. A. Fülöp, Z. Ollmann, Cs. Lombosi, C. Skrobol, S. Klingebiel, L. Pálfalvi, F. Krausz, S. Karsch and J. Hebling. "Efficient generation of THz pulses with 0.4 mJ energy". In: *Opt. Express* 22.17 (2014), pp. 20155–20163. DOI: 10.1364/OE.22.020155. URL: https://opg.optica.org/oe/abstract.cfm?URI=oe-22-17-20155.

[14] H. Vincenti and F. Quéré. "Attosecond Lighthouses: How To Use Spatiotemporally Coupled Light Fields To Generate Isolated Attosecond Pulses". In: *Phys. Rev. Lett.* 108 (11 2012), p. 113904. DOI: 10.1103/PhysRevLett.108.113904. URL: https://link.aps.org/doi/10.1103/PhysRevLett.108.113904.

[15] Bahaa EA Saleh and Malvin Carl Teich. *Fundamentals of photonics*. john Wiley & sons, 2019.

[16] U. Keller. *Ultrafast Lasers: A Comprehensive Introduction to Fundamental Principles with Practical Applications*. Graduate Texts in Physics. Springer International Publishing, 2022. ISBN: 9783030825317. URL: https://books.google.se/books?id=jjuEzgEACAAJ.

[17] O. E. Martinez, J. P. Gordon and R. L. Fork. "Negative group-velocity dispersion using refraction". In: *J. Opt. Soc. Am. A* 1.10 (1984), pp. 1003–1006. DOI: 10.1364/JOSAA.1.001003. URL: https://opg.optica.org/josaa/abstract.cfm?URI=josaa-1-10-1003.

[18] Joseph W Goodman. *Introduction to Fourier optics*. Roberts and Company publishers, 2005.

[19] Michael Thompson. "Digital image processing by rafael c. gonzalez and paul wintz". In: *Leonardo* 14.3 (1981), pp. 256–257.

[20] Selcuk Akturk, Xun Gu, Erik Zeek and Rick Trebino. "Pulse-front tilt caused by spatial and temporal chirp". In: *Opt. Express* 12.19 (2004), pp. 4399–4410. DOI: 10.1364/OPEX.12.004399. URL: https://opg.optica.org/oe/abstract.cfm?URI=oe-12-19-4399.

[21] G Pretzler, A Kasper and KJ Witte. "Angular chirp and tilted light pulses in CPA lasers". In: *Applied Physics B* 70 (2000), pp. 1–9.

[22] Selcuk Akturk, Xun Gu, Pablo Gabolde and Rick Trebino. "The general theory of first-order spatio-temporal distortions of Gaussian pulses and beams". In: *Opt. Express* 13.21 (2005), pp. 8642–8661. DOI: 10.1364/OPEX.13.008642. URL: https://opg.optica.org/oe/abstract.cfm?URI=oe-13-21-8642.

[23] Anne-Lise Viotti, Marcus Seidel, Esmerando Escoto, Supriya Rajhans, Wim P Leemans, Ingmar Hartl and Christoph M Heyl. "Multi-pass cells for post-compression of ultrashort laser pulses". In: *Optica* 9.2 (2022), pp. 197–216.

[24] Seth L. Cousin, Juan M. Bueno, Nicolas Forget, Dane R. Austin and J. Biegert. "Three-dimensional spatiotemporal pulse characterization with an acousto-optic pulse shaper and a Hartmann–Shack wavefront sensor". In: *Opt. Lett.* 37.15 (2012), pp. 3291–3293. DOI: 10.1364/OL.37.003291. URL: https://opg.optica.org/ol/abstract.cfm?URI=ol-37-15-3291.

[25] Gustave Pariente, V Gallet, Antonin Borot, Olivier Gobert and Fabien Quéré. "Space–time characterization of ultra-intense femtosecond laser beams". In: *Nature Photonics* 10.8 (2016), pp. 547–553.

[26] Antonin Borot and Fabien Quéré. "Spatio-spectral metrology at focus of ultrashort lasers: a phase-retrieval approach". In: *Opt. Express* 26.20 (2018), pp. 26444–26461. DOI: 10.1364/OE.26.026444. URL: https://opg.optica.org/oe/abstract.cfm?URI=oe-26-20-26444.

[27] Pablo Gabolde and Rick Trebino. "Single-shot measurement of the full spatio-temporal field of ultrashort pulses with multi-spectral digital holography". In: *Opt. Express* 14.23 (2006), pp. 11460–11467. DOI: 10.1364/OE.14.011460. URL: https://opg.optica.org/oe/abstract.cfm?URI=oe-14-23-11460.

[28] Slava Smartsev, Aaron Liberman, Igor Andriyash, Antoine Cavagna, A. Flacco, Camilla Giaccaglia, Jaismeen Kaur, Joséphine Monzac, Sheroy Tata, Aline Vernier, Victor Malka, Rodrigo Lopez-Martens and Jérôme Faure. "Simple few-shot method for spectrally resolving the wavefront of an ultrashort laser pulse". In: (July 2023). DOI: 10.48550/arXiv.2307.15799.

[29] Supriya Rajhans, Esmerando Escoto, Nikita Khodakovskiy, Praveen K Velpula, Bonaventura Farace, Uwe Grosse-Wortmann, Rob J Shalloo, Cord L Arnold, Kristjan Põder, Jens Osterhoff et al. "Post-compression of multi-millijoule picosecond pulses to few-cycles approaching the terawatt regime". In: *Optics Letters* 48.18 (2023), pp. 4753–4756.

# Appendix A

# Matlab code for data processing

```
%% STC analalysis code
% First we read the data:
% Int_xyt - intensity,
% t- time,
% x- physical x dimension of the camera:

% Quick instructions:

%%%%%%%%%%%%%%%%%%%%%%%%%%%%%%%%%%%%%%%%%%%%%%%%%%%%%%%%%%%%%%%%%%%%%%%%%%%%%%%

% 1. variables that is located between the blocks should be changed
    depending on data

%%%%%%%%%%%%%%%%%%%%%%%%%%%%%%%%%%%%%%%%%%%%%%%%%%%%%%%%%%%%%%%%%%%%%%%%%%%%%%%

% 2. It is better to run section by section

%%
clear;
clc;
close all;

filename=['Filename.h5'];

Int_xyt=h5read(filename,'/Int');
t=h5read(filename,'/t');
x=h5read(filename,'/x');

%% 2. introducing the time mask
% define left t_left and t_right edges for the timemask

%%%%%%%%%%%%%%%%%%%%%%%%%%%%%%%%%%%%%%%%%%%%%%%%%%%%%%%%%%%%%%%%%%%%%%%%%%%%%%%
% enter the left and right edge of time (fs):

t_left=-440;
t_right=440;

%%%%%%%%%%%%%%%%%%%%%%%%%%%%%%%%%%%%%%%%%%%%%%%%%%%%%%%%%%%%%%%%%%%%%%%%%%%%%%%
s=size(Int_xyt);

%timemask is better when it is exponential smooth
time_mask=single(permute(1./(1+exp((t-t_right)/3))./(1+exp((t_left-t)
    /3)),[1,3,2])); %time mask
%
pix_x_cor=s(1)/2;                       % central pixel coordinates
pix_y_cor=s(2)/2;

```

```
x0=10;y0=300;width=2000;height=500;

figure('Units', 'pixels','Position', [x0 y0 width height],'Name', '
    Spectra' ,'PaperPositionMode', 'auto'); clf;
subplot(1,2,2)
Cor_field = (squeeze(Int_xyt(pix_x_cor,pix_y_cor,:))-mean(squeeze(
    Int_xyt(pix_x_cor,pix_y_cor,:)),[1,2,3])).*squeeze(time_mask);
plot(t,Cor_field)
xlabel("Time (fs)")
ylabel("Spectral magnitude, (arb. units)")
title("Windowed data")

subplot(1,2,1)
Cor_field = squeeze(Int_xyt(pix_x_cor,pix_y_cor,:)-mean(squeeze(
    Int_xyt(pix_x_cor,pix_y_cor,:)),[1,2,3]));
plot(t,Cor_field)
ylabel("Spectral magnitude, (arb. units)")
xlabel("Time (fs)")
title("Raw data")

%% (optional) see the camera image at the given time delay

% Enter the index of time delay (between 1-512):
idx_t=252;      % <-------------------------

figure(1);clf;
imagesc(Int_xyt(:, :, idx_t));
xlabel('x, pixel')
ylabel('y, pixel')
title("Delay time: "+num2str(round(t(idx_t)))+" fs");
axis square;
colorbar
%% 3. Taking FFT
% define x and y axis for the FFT
c=0.299792458;
siz=size(Int_xyt);          % size of Intxy_t
dx=mean(diff(x));
x=(0:(siz(1)-1))*dx;
y=x';                       % since image square y and x are the same
dt=mean(diff(t));           % time step

% Enter the resolution:
N=2^13;   % <------- Here you can  change the resolution

T=dt*(1:N);
F=(0:N-1)/N/dt;

% Enter the upper and lower limit for the wavelength in um
%%%%%%%%%%%%%%%%%%%%%%%%%%%%%%%%%%%%%%%%%%%%%%%%%%%%%%%%%%%%%%%%%%%%%%%
wavelength_lower = 1.02;
wavelength_upper = 1.04;
%%%%%%%%%%%%%%%%%%%%%%%%%%%%%%%%%%%%%%%%%%%%%%%%%%%%%%%%%%%%%%%%%%%%%%%

% Converting these limits into frequency domain
f_upper = c/wavelength_lower;
f_lower = c/wavelength_upper;

%creating id to filter the data in a given range
```

```
id=permute((F>f_lower)&(F<f_upper),[1,3,2]);            % indexes of
    the given frequency range

K=sum(id);                                              % How many
    spectral points correspond that area
M=siz(1);                                               % number of
    points spatial

Int0=mean(Int_xyt,3);                % Avg. intensity for each pixel,
     since the intensity in the third dimension

Int_xyf=complex(zeros(M,M,K,'single')); %same dimension, x,y,f
    creating empty intensity data for frequency domain

% start FFT for each pixel:
%%
for i=1:M
    disp(i)
    sp=fft(((Int_xyt(i,:,:))-(Int0(i,:))).*time_mask,N,3);      %
    slice by slice fft
    Int_xyf(i,:,:)=sp(1,:,id);                                  %
    save it with frequency filtering.
end

%% 4. Plotting the spectrum of the central point

c=0.299792458;
f0=F(id);                   % selecting only filtered frequency
    values
k0=2*pi*f0/(c);             % wavenumber of the filtered frequency
    values

% Here we find the spectral amplitude at the center: amp_c      (1
    x1x388)
amp_c=sqrt(abs(Int_xyf(M/2,M/2,:))).*exp(1i*angle(Int_xyf(M/2,M/2,:))
    ); % spectral amplitude at center

% finding indexes that correspond to maximum and minimum values:
[maxval,maxind] = max(abs(squeeze(amp_c)/max(amp_c)));
w_central = c./f0(maxind);                                  % central
    wavelength

spectrum_intensity=abs(squeeze(amp_c))/max(abs(squeeze(amp_c)));

% Plots spectrum in center intensity vs frequency:
x0=10; y0=300; width=2000; height=500;
figure('Units', 'pixels','Position', [x0 y0 width height],'Name', '
    Spectra' ,'PaperPositionMode', 'auto'); clf;
plot(f0,spectrum_intensity);
xline(f0(maxind), '--r')
xlabel('frequency, PHz')
ylabel('spectral amplitude norm. unit')
title("Central wavelength: " + round(w_central*1e3) + " nm"+', ('+f0(
    maxind)+"PHz)")

% Plots spectrum in center intensity vs wavelength:
w0=c./f0;

```

```
figure(); clf;
plot(w0, spectrum_intensity);
xline(w0(maxind), '--r')
xlabel("wavelength, nm");
ylabel("spectrum intensity, norm. unit")
title("Central wavelength: " + round(w_central*1e3) + " nm")
axis square;

%% 5. Subtraction of the reference beam
% Dimensions um (micrometer), PHz (petaherz), fs-(femtosecond)

% Normalize the spectral intensity relative to the value at the
    centre of the image:

amp_xyf=Int_xyf./amp_c;

x=x-mean(x);                              % centering
y=x';

% we need to find to parameters in order to subtract correct
    reference
% spherical beam from the interferometric image
%%%%%%%%%%%%%%%%%%%%%%%%%%%%%%%%%%%%%%%%%%%%%%%%%%%%%%%%%%%%%%%%
% Enter the distance between camera and the focus and offset:

D=-7.1e4;

x0=-9;
y0=-40;
%%%%%%%%%%%%%%%%%%%%%%%%%%%%%%%%%%%%%%%%%%%%%%%%%%%%%%%%%%%%%%%%
[X,Y]=meshgrid(x,y);             % create a grid for the spherical
    wavefront, here x and y in um (real world values)

Sph=single(exp(1i*permute(k0,[1,3,2]).*((X-x0).^2+(Y-y0).^2)/(2*D)));
     % Formula for the spherical wavefront

amp_xyf_R=amp_xyf.*Sph;          % HERE WE SUBTRACT THE SPHERICAL BEAM
     FROM THE INTERFEROMETRIC IMAGE:

% plot the subtracted wavefront phase
% in that image there should not be any fringes
% if there is a finges try to change values of D until you see image
    that
% contains no fringes. By changing x0 and y0 one can center the image
    :

figure(5);clf;
set(gcf,'color','w');
imagesc(x/1e4, y/1e4, angle(amp_xyf_R(:,:,maxind)));                %
     divived 1e4 for converting into sm
xlabel('x size, sm');
ylabel('y size, sm');
axis square;
title("Here is the subtracted beam wavefront")
clear 'Sph';

% This is this lines of code for radial filtering of the image:

```

```
R=single(sqrt(X.^2+Y.^2));

% Here you enter the mask radius:
% mask radius and smooth parameter in um:
%%%%%%%%%%%%%%%%%%%%%%%%%%%%%%%%%%%%%%%%%%%%%%%%%%%%%%%%%%%%%%%%%%%%%%%
r_mask=1000;
smooth_param=300;

%%%%%%%%%%%%%%%%%%%%%%%%%%%%%%%%%%%%%%%%%%%%%%%%%%%%%%%%%%%%%%%%%%%%%%%
% this is equation for mask:
mask=1./(1+exp((R-r_mask)/smooth_param));

% one can also use the frequency mask
% equation for the frequency mask

mask_f=single(permute(1./(1+exp((f0-f_upper)/0.005))./(1+exp((f_lower
    -f0)/0.005)),[1,3,2]));

% Here we apply both radial and frequency mask:

amp_xyf_M=amp_xyf_R.*mask.*mask_f;
amp_xyf_M_before_filter = amp_xyf_M;

kx=fftshift(2*pi/dx.*((-M/2+1):M/2)/M);
imax=fft2(amp_xyf_M(:,:,maxind));
[Kx,Ky]=meshgrid(kx,kx);

% Here we plot for comparison:
figure(3);clf;
set(gcf,'color','w');

subplot(1,3,1)
imagesc(x/1e4, y/1e4, angle(amp_xyf(:,:,maxind)))    % phase of the
    interferogram,
xlabel('x size, sm');
ylabel('y size, sm');
axis xy
axis square
title("Phase NF")

subplot(1,3,2)
imagesc(x/1e4, y/1e4, angle(amp_xyf_R(:,:,maxind)))  % phase after
    subtraction of ref beam
xlabel('x size, sm');
ylabel('y size, sm');
axis xy
axis square
title("Corrected Phase NF")

subplot(1,3,3)
imagesc(x/1e4, y/1e4, angle(amp_xyf_R(:,:,maxind)).*mask) % and phase
     when we apply frequency filtering
xlabel('x size, sm');
ylabel('y size, sm');
axis xy
axis square
title("With Spatial Filter")

```

```
%% Plotting the image of the beam after the reference beam
    subtraction:

figure(4); clf;
imagesc(x/1e4, y/1e4, abs(amp_xyf_R(:,:,maxind)))
xlabel('x size, sm')
ylabel('y size, sm')
axis xy
axis square
title("Beam profile after removing ref. phase")

saveas(gca,fullfile(fname_img, ['5.Beam_after_subtr' name '.png']), '
    png');

%% 6. Filtering in the k space and back again
Kr=sqrt(Kx.^2+Ky.^2);             % radial kl

% Enter the value for the divergency window for spatial filtering in
    rad
%%%%%%%%%%%%%%%%%%%%%%%%%%%%%%%%%%%%%%%%%%%%%%%%%%%%%%%%%%%%%%%%%%%

divg=0.0062;

%%%%%%%%%%%%%%%%%%%%%%%%%%%%%%%%%%%%%%%%%%%%%%%%%%%%%%%%%%%%%%%%%%%

for i=1:K
    im0=fft2(amp_xyf_M(:,:,i))./(1+exp(single((Kr/k0(i))-divg)
    /0.0005)); % going to k space with divergency mask
    amp_xyf_M(:,:,i)=ifft2(im0);
       % transform back with divergency applied
    disp(i);
end

sp=squeeze(amp_xyf_M(s(1)/2,s(2)/2,:));
sp0=sp/max(abs(sp));

%% Here we plot the comparison spectral image with maximum intensity
    before and after lowpass filter
% Here is important you select the maxind
after_filter=abs(amp_xyf_M(:,:,maxind)).^2;

figure(8);clf;
set(gcf,'color','w');
subplot(1,2,1)
imagesc(x/1e4, y/1e4, abs(amp_xyf_M_before_filter(:,:,maxind)).^2)
xlabel('x size, sm')
ylabel('y size, sm')
axis square
title("Original beam")
colorbar

subplot(1,2,2)
imagesc(x/1e4, y/1e4, after_filter )
xlabel('x size, sm')
ylabel('y size, sm')
axis square
title("After Lowpass filter")
colorbar
```

```
301
302 %% Zernike Polynomials!
303
304 %%%%%%%%%%%%%%%%%%%%%%%%%%%%%%%%%%%%%%%%%%%%%%%%%%%%%%%%%%%%%%%%%%%%%%%
305 % radius in um, of the area where we are doing the zernike
    decomposition
306
307 rho=1000;
308
309 %%%%%%%%%%%%%%%%%%%%%%%%%%%%%%%%%%%%%%%%%%%%%%%%%%%%%%%%%%%%%%%%%%%%%%%
310 ang=atan2(Y,X);
311 siz=size(X);
312 Z=zeros(siz(1),siz(2),14);
313 r=R/rho;
314 id=r<1;
315
316 % id=id/sqrt(sum(id(:)));       % Before it was like that
317 id0=1/sum(id(:));
318
319 Z(:,:,1)=1;                     % piston
320 Z(:,:,2)=1.*(2.*(r).*sin(ang)); % tilt y
321 Z(:,:,3)=1.*(2.*(r).*cos(ang)); % tilt x
322 Z(:,:,4)=1.*(sqrt(6)*r.^2.*sin(2*ang)); % oblique asigmatism
323 Z(:,:,5)=1.*(sqrt(3)*(2*r.^2-1));       % defocus
324 Z(:,:,6)=1.*(sqrt(6)*r.^2.*cos(2*ang)); % vertical astimatism
325 Z(:,:,7)=1.*(sqrt(8)*r.^3.*sin(3*ang)); % Vertical trefoil
326 Z(:,:,8)=1.*(sqrt(8)*(3*r.^3-2*r).*sin(ang)); % Vertical coma
327 Z(:,:,9)=1.*(sqrt(8)*(3*r.^3-2*r).*cos(ang)); % Horizontal coma
328 Z(:,:,10)=1.*(sqrt(8)*r.^3.*cos(3*ang));      % Oblique trefoil
329 Z(:,:,11)=1.*(sqrt(10)*r.^4.*sin(4*ang));     % Oblique quadrafoil
330 Z(:,:,12)=1.*(sqrt(10)*(4*r.^4-3*r.^2).*sin(2*ang)); % Oblique
    secondary astigmatism
331 Z(:,:,13)=1.*(sqrt(5)*(6*r.^4-6*r.^2+1));            % Primary
    spherical
332 Z(:,:,14)=1.*(sqrt(10)*(4*r.^4-3*r.^2).*cos(2*ang)); % Vertical
    secondary astigmatism
333 Z(:,:,15)=1.*(sqrt(10)*r.^4.*cos(4*ang));           % Vertical
    quadrafoil
334
335 %% Zernike coefficient calculation:
336
337 co=zeros(15,K);
338 for i=1:K
339     wf=angle(amp_xyf_M(:,:,i))./k0(i);
340     Co=squeeze(sum(sum(id.*wf.*Z,1),2))*id0;
341     co(:,i)=Co;
342     disp(i)
343 end
344
345 %% Plotting all astigmatism for different frequency
346 figure("Name", "Astig"); clf;
347
348 names=["piston", "tilt y", "tilt x", "oblique astigmatism", "defocus"
    , "vertical astigmatism", "vertical trefoil", "vertical coma",...
349     "horizontal coma", "oblique trefoil", "oblique quadrafoil", "
    Oblique sec. astigmatism", ...
350     "Primary spherical", "Vertical secondary astigmatism", "Vertical
    quadrafoil" ];
```

```
351
352 for i=1:15
353     subplot(5, 3, i)
354     hold on
355     plot(f0,abs(sp0).^2, '--k', 'DisplayName','spectrum')
356     yyaxis right
357     plot(f0,co(i,:), 'DisplayName',names(i))
358     xlabel("f (Phz)")
359     box on
360     legend
361 end
362
363
364
365 %% Plotting WAVEFRONT for the different wavelength:
366
367 figure("Name", "Wavefront Original"); clf;
368 dC=round(K/20);
369
370 for i=dC:dC:K
371     wf=angle(amp_xyf_M(:, :, i))./k0(i);
372     subplot(4, 5, round(i/dC))
373     imagesc(x/1e4, x/1e4, wf.*id);
374     colorbar
375     xlabel('x size, sm')
376     ylabel('y size, sm')
377     axis square;
378     title("Wavefront for "+w0(i)*1e3+'nm')
379 end
380
381
382 %% WAVEFRONT DECOMPOSITION using Zernike decomposition:
383
384 % Assuming you have the following matrices:
385 % co: Matrix containing Zernike coefficients (15 coefficients for 115
    frequency values)
386 % Z: Matrix containing Zernike polynomials (512x512x15)
387
388 % Initialize the result matrix
389 decomposed_1 = zeros(size(Z, 1), size(Z, 2), size(co, 2));
390
391 % Loop through each frequency value
392 for freq_index = 1:size(co, 2)
393     % Extract the Zernike coefficients for the current frequency
394     coefficients = co(:, freq_index);
395
396     % Multiply coefficients with Zernike polynomials and sum over all
    coefficients
397     for i = 1:size(co, 1)
398         decomposed_1(:, :, freq_index) = decomposed_1(:, :,
   freq_index) + coefficients(i) * Z(:, :, i).*id;
399     end
400 end
401
402 figure(12); clf;
403 dC=round(K/20);
404
405 for i=dC:dC:K
```

```
    subplot(4, 5, round(i/dC))
    imagesc(x/1e4, x/1e4, decomposed_1(:, :, i));
    xlabel('x size, sm')
    ylabel('y size, sm')
    colorbar
    axis square;
    title("Decomposed wavefront: "+w0(i)*1e3+'nm')
end

%% Finding average Zernike coefficients

% For finding average of the Zernike coefficients
% enter the frequency range in which that coeffients more or less
% contant for all colors

%%%%%%%%%%%%%%%%%%%%%%%%%%%%%%%%%%%%%%%%%%%%%%%%%%%%%%%%%%%%%%%%
f_min=0.284;
f_max=0.3;
%%%%%%%%%%%%%%%%%%%%%%%%%%%%%%%%%%%%%%%%%%%%%%%%%%%%%%%%%%%%%%%%

idx_range=find(f0 >= f_min & f0 <= f_max);

co_mean= zeros(size(15));

% Finding average Zernike coefficients of the given frequency range:

for i=1:15
    coef=co(i, :);
    co_mean(i)=mean(coef(idx_range));
end

% Plotting together spectrum, Zernike coefficients and averaged
   Zernike
% coefficients at the given frequency range.

% Plotting all of the astigmatims with mean values:
figure("Name", "Plot with mean values"); clf;

for i=1:15
    subplot(5, 3, i)
    hold on
    plot(f0,abs(sp0).^2, '--k', 'DisplayName','spectrum')
    yyaxis right
    plot(f0,co(i,:), 'DisplayName',names(i))
    legend
    yline(co_mean(i), "--", ["avg."+co_mean(i)])
    % xlim([f_min, f_max])
    xlabel("f (Phz)")
    box on
end

%% REMOVING COMMON ABERRATIONS SHARED BY ALL WAVELENGTH
% (COMMON ABERRATION CORRECTION):

[s1, s2, s3]=size(amp_xyf_M);
ab_free_amp_xyf_M=zeros(s1, s2, s3);
all_zernike=zeros(s1, s2);

```

```
% Here we add all of the avg. astigmatisms:
for j=1:15
    all_zernike=all_zernike+co_mean(j)*Z(:, :, j);
end

% and make correction to the field
for j=1:K
   disp(j)
   ab_free_amp_xyf_M(:, :, j)=amp_xyf_M(:, :, j).*exp(-1i*all_zernike
   .*k0(j));      % TO BE USED
end

% REMEMBER ab_free_amp_xyf_M will be used for focusing
%% Find Zernike coef. AFTER the FULL CORRECTION:

co_astig_free=zeros(15,K);
for i=1:K
    wf_after2=angle(ab_free_amp_xyf_M(:,:,i))./k0(i);
    Co_astig_free=squeeze(sum(sum(id.*wf_after2.*Z,1),2))*id0;
    co_astig_free(:,i)=Co_astig_free;
    disp(i)
end

% Finding the mean values zernike coefficients after full correction:
co_af_mean= zeros(size(15));

% Finding average Zernike coefficients of the given frequency range:
% For finding average of the Zernike coefficients
% enter the frequency range in which that coeffients more or less
% contant for all colors

%%%%%%%%%%%%%%%%%%%%%%%%%%%%%%%%%%%%%%%%%%%%%%%%%%%%%%%%%%%%%%%%
f_min=0.284;
f_max=0.293;
%%%%%%%%%%%%%%%%%%%%%%%%%%%%%%%%%%%%%%%%%%%%%%%%%%%%%%%%%%%%%%%%

idx_range=find(f0 >= f_min & f0 <= f_max);

for i=1:15
    disp(i)
    coef_after2=co_astig_free(i, :);
    co_af_mean(i)=mean(coef_after2(idx_range));    % it is the mean
   values of the co_astig_free
end

%% COMPARE ALL ABERRATIONS BEFORE AND AFTER THE CORRECTION:

% Plotting the first 4 aberrations
figure("Name", "Correction first 6 astig"); clf;

for i=1:6
    subplot(3, 2, i)
    plot(f0,co(i,:), 'DisplayName',[names(i)+" before"])
    yline(co_mean(i), '--b', co_mean(i),"DisplayName", "avg. before")
    hold on
    plot(f0,co_astig_free(i,:), 'DisplayName',[names(i)+'after'])
    yline(co_af_mean(i),'--r', co_af_mean(i), "DisplayName", "avg.
   after")
```

```
    yyaxis right
    plot(f0,abs(sp0).^2, '--k', 'DisplayName','spectrum')
    xlabel("f (Phz)")
    title([i+". "+names(i)+" correction"])
    box on
    legend
end

% Plotting the last 8 aberrations
figure("Name", "Compare last 8"); clf;
for i=7:14
    subplot(4, 2, i-6)
    plot(f0,co(i,:), 'DisplayName',[names(i)+" before"])
    yline(co_mean(i), '--b', co_mean(i),"DisplayName", "avg. before")
    hold on
    plot(f0,co_astig_free(i,:), 'DisplayName',[names(i)+'after'])
    yline(co_af_mean(i),'--r', co_af_mean(i), "DisplayName", "avg.
   after")
    yyaxis right
    plot(f0,abs(sp0).^2, '--k', 'DisplayName','spectrum')
    xlabel("f (Phz)")
    title([i+". "+names(i)+" correction"])
    box on
    legend
    hold off
end

%% Assing new complex field without common aberrations:
amp_xyf_M=ab_free_amp_xyf_M;

%% Plotting farfield spectral amplitude in k space:
% We define resolution:
P=2^14;             % <------ enter the resolution

% Here we define the grid with better resolution:
x_f=(single(linspace(min(x),max(x),P)));
y_f=(single(linspace(min(y),max(y),P)));
[X,Y]=(meshgrid(x_f,y_f));                      % new meshgrid


% Here is our old meshgrid:
[X0,Y0]=meshgrid(x,y);

id=abs(x_f)<100;            % select spatial part less than 100
   micron
x2=x_f(id);                 % x, filtered #will_be_saved

dx=mean(diff(x_f));

% Here we define grid for the k space with the same resolution as new
    X and
% Y grid:

k=single([0:(P/2),(-P/2+1):-1]/P/dx*2*pi);
[Kx,Ky]=meshgrid(k,k);
K2=(Kx.^2+Ky.^2);
clear 'Kx' 'Ky'

```

```
% k space
kxf = fft2(amp_xyf_M(:,M/2,:));
kyf = fft2(amp_xyf_M(M/2,:,:));

figure(6);clf;
set(gcf,'color','w');

subplot(1,2,1)
imagesc(f0,fftshift(kx),(abs(fftshift(squeeze(kxf),1)).^2))
title("farfield, kx, f")
xlabel("f (PHz)")
ylabel("k (1/um)")
colorbar
axis square

ylim([-0.02,0.02])
subplot(1,2,2)
imagesc(f0,fftshift(kx),(abs(fftshift(squeeze(kyf),1)).^2))
title("farfield, ky, f")
xlabel("f (PHz)")
ylabel("k (1/um)")
ylim([-0.02,0.02])
colorbar
axis square

%% THE PROPAGATION!!!
Dz=(single(100e3)); %100e3 micro meter focal length

amp_foc=complex(zeros(sum(id),sum(id),K,'single')); %focus profile
    spatial and spectrally
amp_foc_ideal=complex(zeros(sum(id),sum(id),K,'single')); %same "
    thing <3 "
diff_offset=250;

% i=325;
for i=1:K
    amp=interp2(X0,Y0,(amp_xyf_M(:,:,i)),X,Y,'linear',0).*exp(1i*k0(i
    )*(sqrt(Dz^2-X.^2-Y.^2)-Dz)); %we curve the wavefront with
    specified focal length
    amp_r=ifft2(fft2(amp).*exp(1i*sqrt(k0(i)^2-K2)*(Dz-diff_offset)))
    ; % diffraction gives offset of real focus
    amp_foc(:,:,i)=amp_r(id,id);
    amp_ideal=interp2(X0,Y0,abs(amp_xyf_M(:,:,i)),X,Y,'linear',0).*
    exp(1i*k0(i)*(sqrt(Dz^2-X.^2-Y.^2)-Dz)); %removes wavefront error
    from each frequency (abs)
    amp_r=ifft2(fft2(amp_ideal).*exp(1i*sqrt(k0(i)^2-K2)*(Dz-250)));
    amp_foc_ideal(:,:,i)=amp_r(id,id);
    disp(i);
end



%% Reconstructed image at the focus!

% Define the desired figure width and height
figureWidth = 1000; % in pixels
figureHeight = 400; % in pixels

```

```
% Create a new figure with the specified width and height
figure('Position', [100, 100, figureWidth, figureHeight]);

selected_freq_index=maxind;
set(gcf,'color','w');

subplot(1, 3, 1)
imagesc(abs(amp_foc(:,:,selected_freq_index)).^2)
title("Reconstructed image at the focus!")

siz=size(amp_foc);
q=exp(-1i*angle(amp_foc(round(siz(1)/2),round(siz(2)/2),:)));
amp_x=amp_foc.*q; %remove the phase in the middle, mulitply: -i,
    divide: +i
axis square

subplot(1, 3,2)
imagesc(abs(amp_x(:,:,selected_freq_index)).^2)
title("after removing phase in the middle")

q=exp(-1i*angle(amp_foc_ideal(round(siz(1)/2),round(siz(1)/2),:))); %
    same "thing <3 " for ideal one
amp_x_ideal=amp_foc_ideal.*q;
axis square

subplot(1, 3, 3)
imagesc(abs(amp_x_ideal(:,:,selected_freq_index)).^2)
title("the same but for the ideal case")
axis square

saveas(gca,fullfile(fname_img, ['7.Focused_beam_pro' name '.png']), '
    png');

%% Converting to the time domain:

P=2^13;
df=mean(diff(f0));
t0=linspace(-0.5/df,0.5/df,P);
%%%%%%%%%%%%%%%%%%%%%%%%%%%%%%%%%%%%%%%%%%%%%%%%%%%%%%%%%%%%%%%%
% Time window:

id=abs(t0)<300;

%%%%%%%%%%%%%%%%%%%%%%%%%%%%%%%%%%%%%%%%%%%%%%%%%%%%%%%%%%%%%%%%

N=sum(id); %how many points

amp_ft=(zeros(siz(1),siz(2),N,'single')); %spatial grid
amp_ft_ideal=(zeros(siz(1),siz(2),N,'single'));

% for i=1:siz(1)
%     for j=1:siz(1)
%         at=fftshift(abs(fft(amp_x(i,j,:),P,3)).^2);
%         amp_ft(i,j,:)=at(:,:,id);
%     end
% end
for i=1:siz(1)
    at=fftshift(abs(fft(amp_x(i,:,:),P,3)).^2,3);
```

```
    amp_ft(i,:,:)=at(:,:,id);
    at=fftshift(abs(fft(amp_x_ideal(i,:,:),P,3)).^2,3);
    amp_ft_ideal(i,:,:)=at(:,:,id);
    disp(i)
end
%% Finding intensities
int_xyf=sum(abs(amp_x).^2,3);
int_yf=squeeze(sum(abs(amp_x).^2,1));
int_xf=squeeze(sum(abs(amp_x).^2,2));

int_xyf=int_xyf/max(max(int_xyf));
int_x=int_xf/max(max(int_xf));
int_y=int_yf/max(max(int_yf));

%% plot in space frequency
figure(89);clf;
subplot(1,2,1)
imagesc(f0,x2,int_xf)
xlabel("f PHz")
ylabel("x (um)")
pbaspect([2 1 1])

subplot(1,2,2)
imagesc(f0,x2,int_yf)
xlabel("f, PHz")
ylabel("y (um)")
pbaspect([2 1 1])

saveas(gca,fullfile(fname_img, ['7.preview_x_f' name '.png']), 'png')
    ;

%% plot in space wavelength
figure(90);clf;
subplot(1,2,1)
imagesc(w0,x2,int_xf)
xlabel("wavelength, nm")
ylabel("x (um)")
pbaspect([2 1 1])

subplot(1,2,2)
imagesc(w0,x2,int_yf)
xlabel("wavelength, nm")
ylabel("y (um)")
pbaspect([2 1 1])

saveas(gca,fullfile(fname_img, ['8.Preview_x_w' name '.png']), 'png')
    ;

%% saving the stuff
% meta info should contain: divergence filter param, radial filter
    param,
% x0,y0, distance from focus to detector.
% x2: spatial axis in um, here: +- 200 um
% t0: time window selected in fs, here plus minus 200 fs
% f0: frequency window, pHz
% % amp_ft and amp_ft_ideal: 3D in xyt, x,y in terms of focus
    coordinates
% % amp_x and amp_x_ideal: 3D in xyf, x,y in terms of focus
```

```
    coordinates
t0 = t;
folder = "Folder\Where\You\Save\Data";
name = "Name_of_data";

h5create(folder + name + "_zernike.h5",'/f0',[size(f0)]);
h5create(folder + name + "_zernike.h5",'/co',[size(co)]);

h5write(folder + name + "_zernike.h5",'/f0',f0);
h5write(folder + name + "_zernike.h5",'/co',co);

h5create(folder + name + "_xyf.h5",'/amplitude_xyf_real',[size(amp_x)
    ]);
h5create(folder + name + "_xyf.h5",'/amplitude_xyf_imag',[size(amp_x)
    ]);
h5create(folder + name + "_xyf.h5",'/f',[size(f0)]);
h5create(folder + name + "_xyf.h5",'/x',[size(x2)]);

h5create(folder + name + "_xyt.h5",'/amplitude_xyt_real',[size(amp_ft
    )]);
h5create(folder + name + "_xyt.h5",'/amplitude_xyt_imag',[size(amp_ft
    )]);
h5create(folder + name + "_xyt.h5",'/t',[size(t0)]);
h5create(folder + name + "_xyt.h5",'/x',[size(x2)]);

h5create(folder + name + "_xyf_ideal.h5",'/amplitude_xyf_ideal_real'
    ,[size(amp_x_ideal)]);
h5create(folder + name + "_xyf_ideal.h5",'/amplitude_xyf_ideal_imag'
    ,[size(amp_x_ideal)]);
h5create(folder + name + "_xyf_ideal.h5",'/f',[size(f0)]);
h5create(folder + name + "_xyf_ideal.h5",'/x',[size(x2)]);

h5create(folder + name + "_xyt_ideal.h5",'/amplitude_xyt_ideal_real'
    ,[size(amp_ft_ideal)]);
h5create(folder + name + "_xyt_ideal.h5",'/amplitude_xyt_ideal_imag'
    ,[size(amp_ft_ideal)]);
h5create(folder + name + "_xyt_ideal.h5",'/t',[size(t0)]);
h5create(folder + name + "_xyt_ideal.h5",'/x',[size(x2)]);

h5write(folder + name + "_xyf.h5",'/amplitude_xyf_real',real(amp_x));
h5write(folder + name + "_xyf.h5",'/amplitude_xyf_imag',imag(amp_x));
h5write(folder + name + "_xyf.h5",'/f',f0);
h5write(folder + name + "_xyf.h5",'/x',x2);

h5write(folder + name + "_xyt.h5",'/amplitude_xyt_real',real(amp_ft))
    ;
h5write(folder + name + "_xyt.h5",'/amplitude_xyt_imag',imag(amp_ft))
    ;
h5write(folder + name + "_xyt.h5",'/t',t0);
h5write(folder + name + "_xyt.h5",'/x',x2);

h5write(folder + name + "_xyf_ideal.h5",'/amplitude_xyf_ideal_real',
    real(amp_x_ideal));
h5write(folder + name + "_xyf_ideal.h5",'/amplitude_xyf_ideal_imag',
    imag(amp_x_ideal));
h5write(folder + name + "_xyf_ideal.h5",'/f',f0);
h5write(folder + name + "_xyf_ideal.h5",'/x',x2);

```

```
778 h5write(folder + name + "_xyt_ideal.h5",'/amplitude_xyt_ideal_real',
       real(amp_ft_ideal));
779 h5write(folder + name + "_xyt_ideal.h5",'/amplitude_xyt_ideal_imag',
       imag(amp_ft_ideal));
780 h5write(folder + name + "_xyt_ideal.h5",'/t',t0);
781 h5write(folder + name + "_xyt_ideal.h5",'/x',x2);
```

# Appendix B

# DFT equations

Using the integral form of equation 2.25 we can write

$$\begin{aligned}\tilde{G}(\nu) &= \int_{-\infty}^{\infty} \sum_{n=-\infty}^{\infty} f(t)\delta(t - n\Delta T)e^{-j2\pi\nu t}dt \\ &= \sum_{n=-\infty}^{\infty} \int_{-\infty}^{\infty} f(t)\delta(t - n\Delta T)e^{-j2\pi\nu t}dt \\ &= \sum_{n=-\infty}^{\infty} f_n e^{-j2\pi\nu n\Delta T}\end{aligned} \tag{B.1}$$

where $f_n$ is a discrete function but its Fourier transform $\tilde{G}(\nu)$ is continuous and periodic function. Thanks to that, we only need to characterize $\tilde{G}(\nu)$ over one period. Moreover, this equation expands from $-\infty$ to $\infty$, but in practice, we deal with a finite number of samples. So, in order to obtain $M$ equally spaced samples that are taken over one period $\nu = 0$ to $\nu = 1/\Delta T$, we need to take the samples of the following frequencies:

$$\nu = \frac{m}{M\Delta T},\ m = 0, 1, 2, 3, ..., M - 1 \tag{B.2}$$

Substituting this result into equation B.1 and denoting the $G_n$ as a discrete Fourier transform (DFT) we get:

$$G_n = \sum_{n=0}^{M-1} f_n e^{-j2\pi mn/M},\ m = 0, 1, 2, ..., M - 1 \tag{B.3}$$

Contrarily, given $\{G_n\}$ we can reconstruct the sample set $\{f_n\}$ by using *inverse discrete Fourier transform* (IDFT)

$$f_n = \frac{1}{M} \sum_{m=0}^{M-1} G_n e^{j2\pi mn/M},\ n = 0, 1, 2, ..., M - 1 \tag{B.4}$$

We can develop the 2-D discrete Fourier transform in a similar way:

$$\boxed{G(u,v) = \sum_{x=0}^{M-1}\sum_{y=0}^{N-1} f(x,y)e^{-j2\pi(ux/M+vy/M)}} \tag{B.5}$$

where $f(x,y)$ is a 2D discrete function (digital image for example) of size $M \times N$ and $u$ and $v$ are the discrete variables in ranges $u = 0, 1, 2, ..., M-1$ and $v = 0, 1, 2, ..., N-1$.

Inversely, we can recover the $f(x,y)$ 2D sample set if $G(u,v)$ Fourier transform is given. It is called the 2D inverse discrete Fourier transform:

$$\boxed{f(x,y) = \frac{1}{MN}\sum_{u=0}^{M-1}\sum_{v=0}^{N-1} G(u,v)e^{j2\pi(ux/M+vy/N)}} \tag{B.6}$$

for $x = 0, 1, 2, ..., M-1$ and $y = 0, 1, 2, ..., N-1$.